

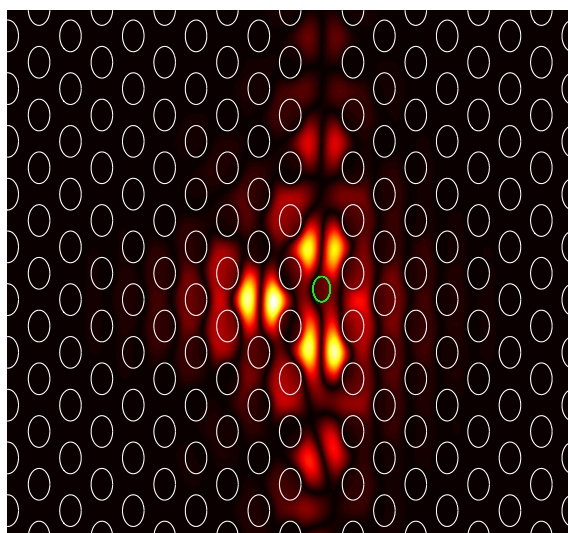


Technical University  
of Denmark

---

# Optical properties of photonic crystal microcavities and waveguides

---



Master Thesis, DTU Photonics  
January 30, 2015

by

---

Andreas Dyhl Østerkryger (s093012)

Technical University of Denmark  
Supervisors:  
Jakob Rosenkrantz de Lasson  
Niels Gregersen  
Jesper Mørk







# Abstract

In recent years the interest in photonic crystal slabs have increased due to their possible applications within integrated photonics. The research is especially driven by the possibility of performing high-speed signal processing with a low energy consumption. For realizing this, photonic switches and modulators are needed, and for photonic switching Fano resonances has been reported particularly advantageous, due to its nonlinear spectral response.

Investigating these Fano resonances are therefore essential for engineering high-speed photonic switches. Fano resonances are realized in photonic crystals by placing a cavity near a blocked waveguide and in the present thesis Fourier modal method implementing both a scattering matrix formalism and a Bloch modal expansion is built from scratch in order to perform simulations on such photonic crystal structures.

With the developed code it is shown that Fano resonances can have two different parities (symmetries) and that coupled-mode theory both predicts and describes this phenomenon very well. By computing the transmission spectra and fitting these to coupled-mode theory it is found that the phase difference between the coupling coefficients in an out of the cavity uniquely determines the parity.

From these transmission spectra it is shown that the parity changes periodically as function of the distance between the cavity and the blocking element. Based on this observation, it is investigated whether a relation between the position of the blocking element in the photonic crystal waveguide field distribution and the parity exists, but no unequivocal correlation between these is found.

New investigations are therefore suggested for determining the phase difference in a different manner than computing transmission spectra and fitting these to coupled-mode theory. The suggestions include implementing quasinormal modes for a better description of the cavity mode, and also a simplification of the investigations by including fewer Bloch modes, when computing the transmission and reflection matrices for the cavity section.



# Resumé

I de seneste år har interessen for fotoniske krystalplader (photonic crystal slabs) været stigende, da disse muligvis kan bruges indenfor integreret fotonik. Forskningen drives især af muligheden for at realisere højhastigheds-signalbehandling ved et lavt energiforbrug. Til dette kræves fotoniske kontakter og modulatorer, og for fotoniske kontakter har det vist sig, at Fano resonanser er særligt fordelagtige grundet deres ikke-lineære spektrale respons.

Derfor er det essentielt at undersøge disse Fano-resonanser for at designe og udvikle højhastigheds-fotoniske kontakter. I fotoniske krystaller fremkommer Fano-resonanser ved at placere en kavitet i nærheden af en blokeret bølgeleder, og i dette speciale simuleres sådanne strukturer ved brug af en fra-bunden-bygget Fourier tilstandsmetode (Fourier modal method), hvori både en spredningsmatrice formalisme og en expansion på Bloch-tilstande er inkorporeret.

Med den udviklede kode vises det, at Fano-resonanser kan have to forskellige pariteter (symmetrier), og at teorien om koblede tilstande (couple-mode theory) både forudsiger og beskriver dette fænomen. Ved at udregne transmissionspektre og fitte disse til teorien om koblede tilstande, er det fundet, at forskellen i fase mellem koblingskoefficienterne ind og ud af kaviteten alene bestemmer pariteten.

Udfra disse transmissionspektre vises det, at pariteten skifter periodisk som funktion af afstanden mellem kaviteten og blokeringselementet i bølgelederen. Baseret på denne observation undersøges det, om der findes en relation mellem positionen af blokerings-elementet i den fotoniske krystal-bølgeleders feltfordeling og pariteten, men ingen entydig korrelation er fundet.

Derfor foreslås nye undersøgelser for at bestemme faseforskellen på en anden måde end ved at udregne transmissionsspektre og fitte disse til teorien for koblede tilstande. Iblant forslagene er at implementere kvasinormale tilstande (quasinormal modes) for at opnå en bedre beskrivelse af kavitets-tilstanden samt en simplificering af undersøgelserne ved at medtage færre Bloch-tilstande i udregningen af transmissions- og refleksionsmatricerne for kavitetssektionen.



# Preface

This thesis is submitted as a fulfilment of the requirements for obtaining the degree of Master of Science in Engineering in Physics and Nanotechnology at the Technical University of Denmark. The thesis is completed in collaboration with the Nanophotonics Theory & Signalprocessing group at DTU Fotonik, Department of Photonics Engineering, under the supervision of PhD-Student Jakob Rosenkrantz de Lasson, Associate Professor Niels Gregersen and Professor Jesper Mørk. The duration of the work has been 5 months from September 2014 to January 2015 corresponding to a credit of 30 ECTS.

It has been a true pleasure working, discussing and interacting with my supervisors throughout the project. A special thanks goes to Jakob for always having time to discuss the small details and for scheduling football for the department every Tuesday morning to great joy of all participants. I would like to thank Niels for introducing me to the world of computational photonics through my 3 week project in June 2013 and also Jepser for introducing me to the exciting subject of Photonic Crystals through his course on Nanophotonics. Furthermore, I would like to acknowledge my fellow student Martin Bækbo for our daily lunch dates during this thesis, where we have shared our concerns and successes experienced in each of our theses.

At last I would like to thank the fantastic support from my family, friends and girlfriend through the project period.

Andreas Dyhl Østerkryger,  
DTU Fotonik, Department of Photonics Engineering,  
Technical University of Denmark,  
30 January 2015



# Contents

<b>1</b>	<b>Introduction</b>	<b>1</b>
<b>2</b>	<b>Theoretical Concepts</b>	<b>5</b>
2.1	Maxwell's Equations . . . . .	5
2.2	Wave Equations . . . . .	6
2.3	The 2D Eigenvalue Problem for Waveguides . . . . .	7
2.4	Photonic Crystals . . . . .	10
<b>3</b>	<b>Computational Method</b>	<b>15</b>
3.1	The Fourier Modal Method . . . . .	15
3.2	Overview of method implementation . . . . .	34
3.3	Validation of method implementation . . . . .	36
3.4	Why use Fourier Modal method . . . . .	39
3.5	Observed errors in method implementation . . . . .	40
<b>4</b>	<b>Computations on PhC waveguides and microcavities</b>	<b>43</b>
4.1	Cavity resonances . . . . .	43
4.2	Fano structures and parity . . . . .	47
4.3	Field distribution and parity . . . . .	53
<b>5</b>	<b>Discussion and Suggestions</b>	<b>57</b>
5.1	Dependence of resonance frequency on position of blocking element . . . . .	57
5.2	Natural resonance frequency . . . . .	58
5.3	Simplifying the problem by considering fewer Bloch modes . . . . .	59
<b>6</b>	<b>Conclusion and Outlook</b>	<b>61</b>
6.1	Review of thesis . . . . .	61
6.2	Outlook . . . . .	63
<b>A</b>	<b>Appendix for theoretical concepts</b>	<b>65</b>
A.1	Maxwell's equations ins frequency domain . . . . .	65
A.2	Derivation of wave equations . . . . .	66
A.3	Derivation of field components . . . . .	68
A.4	Decoupling of eigenvalue problems . . . . .	69
<b>B</b>	<b>Appendix for computational method</b>	<b>71</b>
B.1	Li's Factorization Rules . . . . .	71
B.2	Evaluation of $\varepsilon_j$ and $a_j$ elements . . . . .	73

B.3	Evaluation of scalar product integral . . . . .	73
B.4	Transmission and reflection matrices . . . . .	75
B.5	Implementation of scattering matrix formalism . . . . .	75
B.6	Derivation of generalized eigenvalue problem for Bloch modes . . . . .	76
B.7	Evaluation of power flow integral . . . . .	77
B.8	Derivation of transmission and reflection matrices between periodic sections	80
B.9	Visualization of field profile in all supercells . . . . .	83
<b>C</b>	<b>Appendix for validation of method implementation</b>	<b>87</b>
C.1	Gap map computations . . . . .	87
<b>D</b>	<b>Appendix for computations on PhC waveguides and microcavities</b>	<b>89</b>
D.1	Derivation of phase factors in coupled-mode theory . . . . .	89
<b>E</b>	<b>Miscellaneous plots</b>	<b>91</b>
E.1	Full field distributions . . . . .	91
E.2	Transmission spectra, $r_{block} = 0.80 r/a$ . . . . .	94
E.3	Transmission spectra $r_{block} = 0.30 r/a$ . . . . .	96
E.4	Resonance frequency and direct transmission coefficient . . . . .	97
E.5	Field distribution in mid of waveguide . . . . .	98
<b>F</b>	<b>CLEO-Europe 2015 submission</b>	<b>101</b>
	<b>Bibliography</b>	<b>103</b>

---

## Introduction

### Photonic crystals

Since the end of the last century the interest in Photonic Crystals (PhCs) have increased. The interest increased rapidly around 2000 during the dotcom boom, where a small Danish company (Crystal Fibre A/S) specialised in designing photonic crystal fibres was started. These photonic crystal fibres was among the first commercial applications of photonic crystals and a lot of research is ongoing in order to develop other commercial applications, such as in-plane PhC lasers [1] and integrated optics [2]. As opposed to the crystal fibres these are realised in PhC slabs and in general a lot of fundamental research on engineering the properties of these slabs is carried out.

Placing a waveguide close to a cavity in a PhC slab leads to transmission and reflection phenomena that has potential applications within photonic switching [3] or PhC lasing [1]. A photonic switch can be realised by the interaction between a waveguide mode and a cavity mode, which will result in a dip in the transmission spectrum when the resonance mode of the cavity is excited. The transmission spectrum will in this case be Lorentzian and a result of a computation on such a system is seen in Figure 1.1. This system is able to be operated as a photonic switch by changing the resonance frequency and thereby changing the transmission at a certain frequency. Placing a blocking element in the waveguide will change the interference between the cavity mode and the waveguide mode such that it no longer produces a Lorentzian transmission spectrum - instead the spectrum now follows the Fano line shape function and it has been reported that these Fano structures are more promising as a photonic switch due to the asymmetric and sharp spectral response of a Fano resonance [4]. Two different Fano resonance spectra computed in this project are seen in Figures 1.2 and 1.3.

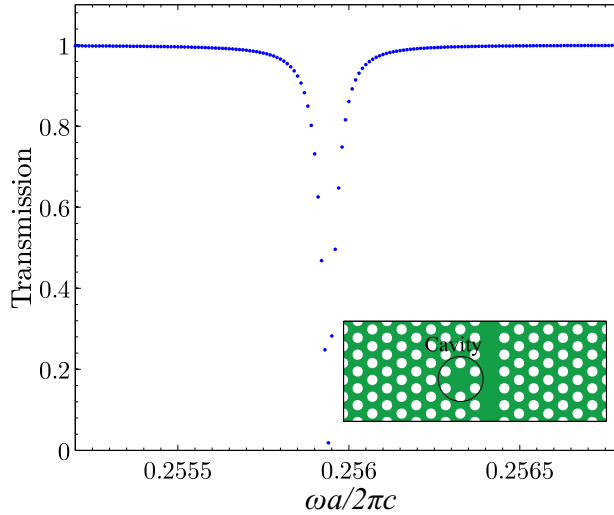


**Figure 1.1:** In the inset the PhC structure is seen. The structure consist of a waveguide and a cavity and as seen this structure leads to a Lorentzian shaped transmission spectrum.

For enabling integrated photonic chips that can meet the increasing demand for information capacity, ultra-compact structures performing signal processing such as modulation and switching at high speed and with low energy consumption are essential [5]. A promising candidate meeting these demands are the PhC slab [6], since this allows for integration of lasers [7], modulators [8], switches [9] and detectors [10]. All these operations need to be processed with low energy consumption and for switching the transmission is changed by altering the resonance frequency of the cavity by applying a control signal changing the refractive index [6]. The less the resonance frequency needs to be changed for switching on and off, the less energy is required in the control signal and therefore the asymmetric behaviour of Fano resonances are superior to Lorentzian resonances in terms of energy consumption. Therefore research in these Fano resonances is important for realizing high speed photonic chips with low energy consumption.

In Figures 1.2 and 1.3 two transmission spectra with different Fano line shape symmetry are seen. The transmission minimum in Figure 1.2 (1.3) is red (blue) shifted relative to the maximum and these two symmetries are referred to as red and blue parity. From coupled-mode theory this parity is found to be related to the coupling between the cavity and the waveguide mode [11], [12], [13], but the only known method for determining the parity is to do a computation of the transmission spectrum and by fitting this to coupled-mode theory determine this coupling. For designing PhC switches it is important to know the parity, and therefore increasing the understanding on how the parity of a PhC Fano structure is determined is essential. Coupled-mode theory lays the mathematical foundation for finding the parity but a more physically intuitive way is still not existing.

This project seeks this intuitive way on determining the parity by increasing the understanding on how the parity changes as function of the position of the blocking element in the waveguide. This leads to the hypothesis motivating this thesis, that there exist a correlation between the parity and the electromagnetic field distribution in a Fano structure.

The hypothesis is investigated by simulations, using the Fourier modal method for computing the transmission and electromagnetic fields in the Fano structures. This method is based on an eigenmode expansion, which is very suitable for computations on periodic structures such as PhCs [14]. There exist different computational methods for finding the electromagnetic field in optical geometries and a discussion on the choice of method is given later on in section 3.4.

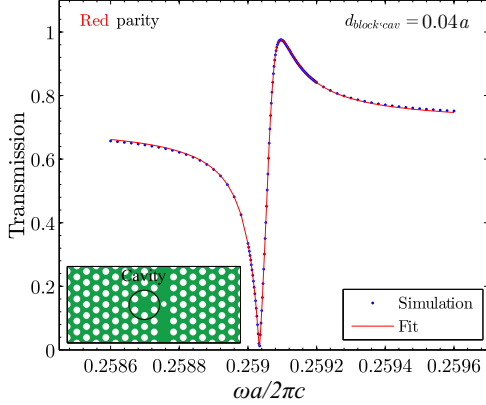


**Figure 1.2:** In the inset the PhC structure consisting of a blocked waveguide and a cavity is seen. The blocking element is shifted along the waveguide relative to the mid point of the cavity and this leads to a Fano transmission spectrum with red parity.

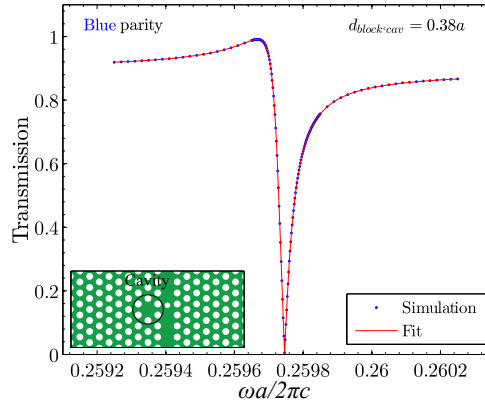


**Figure 1.3:** In the inset the PhC structure consisting of a blocked waveguide and a cavity is seen. The blocking element is shifted further along the waveguide relative to the mid point of the cavity than in Figure 1.2 and this leads to a Fano transmission spectrum with blue parity.

## Outline of thesis

**Chapter 2:** The theoretical groundwork of the investigations is laid, by giving a summary of basic electromagnetism starting from Maxwell's equations and give a short description on the most important properties of PhCs and the effects of introducing defects. Coupled-mode theory will not be given in this chapter, instead the simulation results will be compared with and explained by coupled-mode theory, when presented.

**Chapter 3:** The Fourier modal method used for the simulations is gone through and an overview of the implementation of the method is provided. The developed code is benchmarked by comparing computational results with the equivalent from literature. The chapter ends with a discussion on the choice of Fourier modal method as the method for simulating PhC structures.

**Chapter 4:** The acquired computational results are presented. Firstly, central results from the coupled-mode theory are presented and these are then used for fitting and analysing the computed transmission spectra.

**Chapter 5:** Based on discussing the obtained results presented in Chapter 4, three suggestions for future work are given.

**Chapter 6:** The work presented in this thesis is concluded upon and based on the suggestions for future work an outlook is provided.

Thereafter a number of appendices are found and these are referred to along the way in the thesis. The appendices include derivations, evaluation of expressions and additional results. Part of this work have been submitted for CLEO-Europe 2015 and the submission abstract is found in Appendix F.

---

## Theoretical Concepts

This chapter lays the theoretical groundwork for doing computations on PhC structures. This includes Maxwell's equations, waveguide theory and properties of PhCs.

### 2.1 Maxwell's Equations

Maxwell's equations are the most fundamental equations in electromagnetism and therefore a natural starting point. On the basic differential form in the time-domain these are [15, 16]:

$$\nabla \times \mathbf{E}(\mathbf{r}, t) = -\partial_t \mathbf{B}(\mathbf{r}, t), \quad (2.1.1)$$

$$\nabla \times \mathbf{H}(\mathbf{r}, t) = \partial_t \mathbf{D}(\mathbf{r}, t) + \mathbf{J}(\mathbf{r}, t), \quad (2.1.2)$$

$$\nabla \cdot \mathbf{D}(\mathbf{r}, t) = \rho(\mathbf{r}, t), \quad (2.1.3)$$

$$\nabla \cdot \mathbf{B}(\mathbf{r}, t) = 0, \quad (2.1.4)$$

where  $\mathbf{E}$ ,  $\mathbf{B}$ ,  $\mathbf{H}$  and  $\mathbf{D}$  are the electric field, the magnetic induction, the magnetic field and the electric displacement respectively.  $\rho$  and  $\mathbf{J}$  are free electric charges and current densities.

The relation between the electric and magnetic field is found through the constitutive material equations: [15, 16]

$$\mathbf{D}(\mathbf{r}, t) = \varepsilon_0 \mathbf{E}(\mathbf{r}, t) + \mathbf{P}(\mathbf{r}, t), \quad (2.1.5)$$

$$\mathbf{B}(\mathbf{r}, t) = \mu_0 \mathbf{H}(\mathbf{r}, t) + \mathbf{M}(\mathbf{r}, t), \quad (2.1.6)$$

where  $\mathbf{P}$  and  $\mathbf{M}$  are the polarization and magnetization of the material and  $\varepsilon_0$  and  $\mu_0$  are the vacuum permittivity and permeability respectively.

In this work only nondispersive media have been simulated and in that case the constitutive equations, (2.1.5) and (2.1.6), are reduced to [16]:

$$\mathbf{D}(\mathbf{r}, t) = \varepsilon_0(1 + \chi_e(\mathbf{r}))\mathbf{E}(\mathbf{r}, t) = \varepsilon_0\varepsilon(\mathbf{r})\mathbf{E}(\mathbf{r}, t), \quad (2.1.7)$$

$$\mathbf{B}(\mathbf{r}, t) = \mu_0(1 + \chi_m(\mathbf{r}))\mathbf{H}(\mathbf{r}, t) = \mu_0\mu(\mathbf{r})\mathbf{H}(\mathbf{r}, t), \quad (2.1.8)$$

where  $\varepsilon(\mathbf{r})$  and  $\mu(\mathbf{r})$  are the relative electric permittivity (dielectric function) and magnetic permeability for the material defined from the electric and magnetic susceptibilities,  $\chi_e(\mathbf{r})$  and  $\chi_m(\mathbf{r})$ . The refractive index for a material is then defined from these material parameters as [15, 16]:

$$n = \sqrt{\mu\varepsilon}. \quad (2.1.9)$$

Maxwell's equations are in equations (2.1.1)-(2.1.4) stated in the time-domain but by Fourier transforming the fields these equations can be given in the frequency-domain as well. This leads to [15, 16]:

$$\nabla \times \mathbf{E}(\mathbf{r}, \omega) = -i\omega\mathbf{B}(\mathbf{r}, \omega) = -i\omega\mu_0\mu(\mathbf{r}, \omega)\mathbf{H}(\mathbf{r}, \omega), \quad (2.1.10)$$

$$\nabla \times \mathbf{H}(\mathbf{r}, \omega) = i\omega\mathbf{D}(\mathbf{r}, \omega) + \mathbf{J}_s(\mathbf{r}) = i\omega\varepsilon_0\varepsilon(\mathbf{r}, \omega)\mathbf{E}(\mathbf{r}, \omega) + \mathbf{J}_s(\mathbf{r}). \quad (2.1.11)$$

These are then Maxwell's equations in the frequency domain, which are used to derive second order wave equations. Note that  $\varepsilon$  is the effective dielectric constant. The derivation of these from Maxwell's equations ((2.1.1)-(2.1.4)) are found in Appendix A.1.

## 2.2 Wave Equations

Equations (2.1.10) and (2.1.11) can now be used to derive second-order wave equations only involving the electric or magnetic field and the source current density. Dividing equation (2.1.11) with  $\varepsilon(\mathbf{r}, \omega)$  and taking the curl on both sides will lead to [16]:

$$\nabla \times \frac{1}{\varepsilon(\mathbf{r}, \omega)} \nabla \times \mathbf{H}(\mathbf{r}, \omega) = i\omega\varepsilon_0 \nabla \times \mathbf{E}(\mathbf{r}, \omega) + \nabla \times \left( \frac{\mathbf{J}_s(\mathbf{r}, \omega)}{\varepsilon(\mathbf{r}, \omega)} \right). \quad (2.2.1)$$

Using equation (2.1.10) and the relation between the speed of light in vacuum and the vacuum permittivity and permeability,  $c_0 = (\varepsilon_0\mu_0)^{-1/2}$ , a wave equation only involving the magnetic field will appear [16]:

$$\nabla \times \frac{1}{\varepsilon(\mathbf{r}, \omega)} \nabla \times \mathbf{H}(\mathbf{r}, \omega) - \left(\frac{\omega}{c_0}\right)^2 \mu(\mathbf{r}, \omega) \mathbf{H}(\mathbf{r}, \omega) = \nabla \times \left(\frac{\mathbf{J}_s(\mathbf{r}, \omega)}{\varepsilon(\mathbf{r}, \omega)}\right). \quad (2.2.2)$$

A similar approach will lead to the wave equation only involving the electric field:

$$\nabla \times \frac{1}{\mu(\mathbf{r}, \omega)} \nabla \times \mathbf{E}(\mathbf{r}, \omega) - \left(\frac{\omega}{c_0}\right)^2 \varepsilon(\mathbf{r}, \omega) \mathbf{E}(\mathbf{r}, \omega) = -i\omega\mu_0 \mathbf{J}_s(\mathbf{r}, \omega). \quad (2.2.3)$$

In this project only non-magnetic materials ( $\mu = 1$ ), without any current sources ( $\mathbf{J}_s = 0$ ) has been simulated. This reduces equations (2.2.2) and (2.2.3) to [16]:

$$\nabla \times \frac{1}{\varepsilon(\mathbf{r}, \omega)} \nabla \times \mathbf{H}(\mathbf{r}, \omega) = k_0^2 \mathbf{H}(\mathbf{r}, \omega), \quad (2.2.4)$$

$$\nabla \times \nabla \times \mathbf{E}(\mathbf{r}, \omega) = k_0^2 \varepsilon(\mathbf{r}, \omega) \mathbf{E}(\mathbf{r}, \omega), \quad (2.2.5)$$

where  $k_0 = \omega/c_0$  is the wave number in vacuum.

Using the vector identity  $\nabla \times \nabla \times \mathbf{F} = -\nabla^2 \mathbf{F} + \nabla(\nabla \cdot \mathbf{F})$  and Gauss's law with no free charges ( $\rho = 0$  in equation (2.1.3),  $\nabla \cdot (\varepsilon \mathbf{E}) = 0$ ), on equation (2.2.5) another form of the wave equation for the electric field will appear [16]:

$$\nabla^2 \mathbf{E}(\mathbf{r}, \omega) + \nabla(\mathbf{E}(\mathbf{r}, \omega) \cdot \nabla \ln \varepsilon(\mathbf{r}, \omega)) + \varepsilon(\mathbf{r}, \omega) k_0^2 \mathbf{E}(\mathbf{r}, \omega) = 0 \quad (2.2.6)$$

In the same manner another expression for the magnetic field wave equation can be derived by taking the curl of equation (2.1.11), using equations (2.1.10) and (2.1.11), exploit the vector identity,  $\nabla \times \nabla \times \mathbf{F} = -\nabla^2 \mathbf{F} + \nabla(\nabla \cdot \mathbf{F})$  and use that  $\nabla \cdot \mathbf{H} = 0$  for non-magnetic materials (see equation (2.1.4) and (2.1.8)). And exploit the vector relation  $\nabla \times (\varepsilon \mathbf{E}) = \varepsilon \nabla \times \mathbf{E} + \nabla \varepsilon \times \mathbf{E}$ . Doing this will lead to [16]:

$$\nabla^2 \mathbf{H}(\mathbf{r}, \omega) + \nabla \ln(\varepsilon(\mathbf{r}, \omega)) \times \nabla \times \mathbf{H}(\mathbf{r}, \omega) + k_0^2 \varepsilon(\mathbf{r}, \omega) \mathbf{H}(\mathbf{r}, \omega) = 0. \quad (2.2.7)$$

See Appendix A.2 for the full derivations of equations (2.2.6) and (2.2.7).

Solving the eigenvalue problem given in the wave equations (2.2.6) and (2.2.7) will then give the electric and magnetic field.

## 2.3 The 2D Eigenvalue Problem for Waveguides

The PhC geometries investigated in this thesis can be divided into layers with uniformity along the  $z$ - and  $y$ -axis, thereby the dielectric function only depend on  $x$  in each layer. In Figure 2.1 a waveguide uniform only in the  $z$ -direction and a waveguide uniform in both the  $z$ - and  $y$ -direction is illustrated. Having uniformity in the  $z$ - and  $y$ -direction means that the spatial dependence of the electric and magnetic field can be written as [16]:

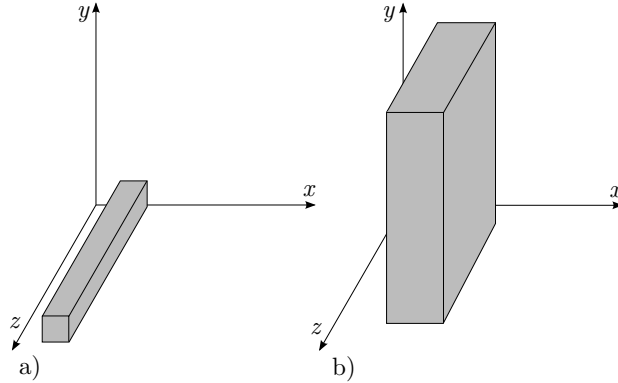


**Figure 2.1:** Waveguides with a uniform dielectric function along a) the  $z$ -direction and b) both the  $z$ - and  $y$ -direction - a so-called slab waveguide.

$$\mathbf{E}(\mathbf{r}) = \mathbf{e}(\mathbf{r}_\perp) \exp(i\beta z), \quad (2.3.1)$$

$$\mathbf{H}(\mathbf{r}) = \mathbf{h}(\mathbf{r}_\perp) \exp(i\beta z), \quad (2.3.2)$$

where  $z$  is the propagation direction.

The time dependent electric and magnetic field, will be considered in the general form:

$$\mathbf{E}(\mathbf{r}, t) = \mathbf{E}(\mathbf{r}) \exp(-i\omega t), \quad \mathbf{H}(\mathbf{r}, t) = \mathbf{H}(\mathbf{r}) \exp(-i\omega t). \quad (2.3.3)$$

Using the electric field given above and exploiting that the dielectric constant does not have a  $z$ -dependence, the eigenvalue problems given in equations (2.2.6) and (2.2.7) can be written as:

$$\nabla_\perp^2 \mathbf{e} + (\nabla_\perp + i\beta \hat{\mathbf{z}}) (\mathbf{e} \cdot \nabla \ln \varepsilon(\mathbf{r}_\perp)) + \varepsilon(\mathbf{r}_\perp) k_0^2 \mathbf{e} = \beta^2 \mathbf{e}, \quad (2.3.4)$$

$$\nabla^2 \mathbf{h} + k_0^2 \varepsilon(\mathbf{r}_\perp) \mathbf{h} + \nabla \ln(\varepsilon(\mathbf{r}_\perp)) \times \nabla \times \mathbf{h} = \beta^2 \mathbf{h}, \quad (2.3.5)$$

where  $\nabla_\perp$  denotes the transverse part of the  $\nabla$ -operator. Equation 2.3.4 is a second order eigenvalue problem, with  $\beta$  as the eigenvalue. By using that the equation can be decoupled into a transverse and a  $z$ -part, a first order eigenvalue problem emerges for the transverse part:

$$\nabla_\perp^2 \mathbf{e}_\perp + \nabla_\perp (\mathbf{e}_\perp \cdot \nabla \ln \varepsilon(\mathbf{r}_\perp)) + \varepsilon(\mathbf{r}_\perp) k_0^2 \mathbf{e}_\perp = \beta^2 \mathbf{e}_\perp, \quad (2.3.6)$$

and this is a standard eigenvalue problem of the form  $\hat{O} \mathbf{e}_\perp = \lambda \mathbf{e}_\perp$ . This equation is essentially what we need to solve in order to find the eigenmodes and eigenvalues of a waveguide. But in order to get the full six component electromagnetic field just solving equation (2.3.6) is not enough, since it only gives the transverse components of the electric field. The  $e_z$  component can be found using  $\nabla(\varepsilon \mathbf{E}) = 0$  leading to [16]:

$$e_z = \frac{-\nabla_{\perp} \cdot (\varepsilon \mathbf{e}_{\perp})}{i\beta\varepsilon}. \quad (2.3.7)$$

This gives the full electric field and by using equation (2.1.10) (with  $\mu = 1$ ) the magnetic field components are found as:

$$\mathbf{h}_{\perp} = \frac{1}{\mu_0\omega} \hat{\mathbf{z}} \times \left[ \beta \mathbf{e}_{\perp} - \nabla_{\perp} \left( \frac{\nabla_{\perp} \cdot (\varepsilon \mathbf{e}_{\perp})}{\beta\varepsilon} \right) \right] \quad (2.3.8)$$

$$h_z = \frac{\hat{\mathbf{z}} \cdot \nabla \times \mathbf{e}_{\perp}}{i\mu_0\omega}. \quad (2.3.9)$$

Equations (2.3.7) through (2.3.9) also gives the relation between the components of the forward and backward propagating electromagnetic waves. The forward propagating mode profile is given as:

$$\begin{bmatrix} \mathbf{E}^+(\mathbf{r}) \\ \mathbf{H}^+(\mathbf{r}) \end{bmatrix} = \begin{bmatrix} \mathbf{e}^+(\mathbf{r}) \\ \mathbf{h}^+(\mathbf{r}) \end{bmatrix} \exp(i\beta z) = \begin{bmatrix} \mathbf{e}_{\perp}(\mathbf{r}_{\perp}) + e_z(\mathbf{r}_{\perp}) \\ \mathbf{h}_{\perp}(\mathbf{r}_{\perp}) + h_z(\mathbf{r}_{\perp}) \end{bmatrix} \exp(i\beta z). \quad (2.3.10)$$

The backward propagating mode profile is then found by interchanging  $\beta$  with  $-\beta$  in equations (2.3.7) to (2.3.10) leading to [16]:

$$\begin{bmatrix} \mathbf{E}^-(\mathbf{r}) \\ \mathbf{H}^-(\mathbf{r}) \end{bmatrix} = \begin{bmatrix} \mathbf{e}^+(\mathbf{r}) \\ \mathbf{h}^+(\mathbf{r}) \end{bmatrix} \exp(-i\beta z) = \begin{bmatrix} \mathbf{e}_{\perp}(\mathbf{r}_{\perp}) - e_z(\mathbf{r}_{\perp}) \\ -\mathbf{h}_{\perp}(\mathbf{r}_{\perp}) + h_z(\mathbf{r}_{\perp}) \end{bmatrix} \exp(-i\beta z). \quad (2.3.11)$$

Thereby the relation between the transverse forward and backward propagating electric and magnetic field components are:

$$\mathbf{e}_{\perp}^- = \mathbf{e}_{\perp}^+, \quad e_z^- = -e_z^+, \quad (2.3.12)$$

$$\mathbf{h}_{\perp}^- = -\mathbf{h}_{\perp}^+, \quad h_z^- = h_z^+. \quad (2.3.13)$$

By decoupling the transverse and lateral part of the magnetic components in equation (2.3.5) the eigenvalue problem becomes:

$$\nabla^2 \mathbf{h}_{\perp} + k_0^2 \varepsilon(\mathbf{r}_{\perp}) \mathbf{h}_{\perp} + \nabla \ln(\varepsilon(\mathbf{r}_{\perp})) \times \nabla \times \mathbf{h}_{\perp} = \beta^2 \mathbf{h}_{\perp}, \quad (2.3.14)$$

and the  $h_z$  component can simply be determined from  $\nabla \cdot \mathbf{H} = 0$  giving:

$$h_z = \frac{i}{\beta} \nabla_{\perp} \cdot \mathbf{h}_{\perp}. \quad (2.3.15)$$

More detailed derivations of all the field components are found in Appendix A.3. The derivation of the electric field components for the case where only the transverse magnetic field is known are also given in this appendix.

## Slab Waveguides

As stated in the top of the previous section the geometries considered in this report only has an  $x$ -dependence on the dielectric constant as illustrated in Figure 2.1b). Such geometries are called slab waveguides and the eigenvalue problems given in equations (2.3.5) and (2.3.6) simplifies since  $\partial_y \mathbf{e} = 0$  and  $\partial_y \mathbf{h} = 0$ , due to the independence on the  $y$ -coordinate. Using this equation (2.3.6) decouples into two equations [16] (see Appendix A.4 for a detailed derivation):

$$\partial_x^2 e_x + \partial_x(e_x \partial_x \ln \varepsilon(x)) + \varepsilon(x) k_0^2 e_x = \beta^2 e_x, \quad (\text{TM}) \quad (2.3.16)$$

$$\partial_x^2 e_y + \varepsilon(x) k_0^2 e_y = \beta^2 e_y, \quad (\text{TE}) \quad (2.3.17)$$

and similarly equation (2.3.5) decouples into:

$$\partial_x^2 h_x + \varepsilon(x) k_0^2 h_x = \beta^2 h_x, \quad (\text{TE}) \quad (2.3.18)$$

$$\partial_x^2 h_y + \varepsilon(x) k_0^2 h_y - (\partial_x \ln \varepsilon(x)) \partial_x h_y = \beta^2 h_y. \quad (\text{TM}) \quad (2.3.19)$$

The  $z$ -component of the electric and magnetic field is then computed using equations (2.3.7) and (2.3.9) and this gives for (TE):  $e_z = 0$ , since  $\partial_y \mathbf{e} = 0$  and  $e_x = 0$  and for (TM):  $h_z = 0$ , since  $\partial_y \mathbf{h} = 0$  and  $e_y = 0$ . Thereby, solutions where the electric field is polarized only along the  $y$ -direction is referred to as transverse electric (TE) modes. And in the same way solutions where the magnetic field is polarized only in the  $y$ -direction is referred to as transverse magnetic (TM) modes.

The method for solving equations (2.3.17) and (2.3.19) is described in Chapter 3.

## 2.4 Photonic Crystals

This section provides a very brief summary on the properties of photonic crystals and introduce basic terms that are used throughout the report.

A crystal is by definition a material, which is periodic in all directions. A *photonic* crystal (PhC) is thus a crystal that has photonic properties. These photonic properties relates to how light propagates through the PhC. For some geometries band gaps appear meaning that polarized light at certain wavelengths cannot propagate through the PhC and these band gaps are actually the most interesting feature of PhCs, since they allow the creation of waveguides by introducing a line defect in the PhC [17]. The band gaps arises when no light modes are allowed inside the PhC for a range of frequencies. A PhC band diagram for TM polarized light is shown in Figure 2.2 for a triangular lattice (see Figure 2.4), where  $r/a = 0.30$  and the refractive index of the background is  $n_b = 3.1$ . A band gap is clearly visible for frequencies between  $0.235 (2\pi c/a)$  and  $0.305 (2\pi c/a)$ . In Figure 2.3 a line defect (see Figure 2.6) is introduced and this results in waveguide modes inside the band gap of the bulk PhC. A slow light and a fast light region is indicated, and the terms 'slow' and 'fast' are related to the group velocity, which is given as the slope of the dispersion curve [18]:

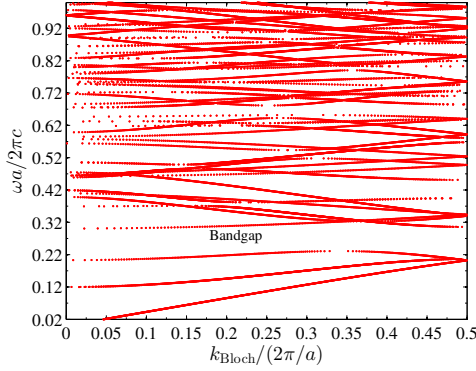


**Figure 2.2:** A band diagram computed using the implementation of the Fourier modal method for a triangular PhC as shown in Figure 2.4.

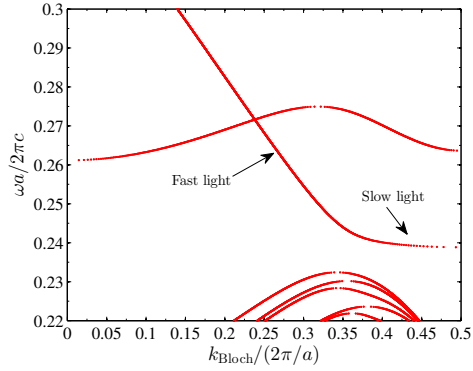


**Figure 2.3:** A zoom on the band gap, where a line defect in the PhC has been introduced. This line defect gives rise to waveguide modes inside the band gap.

$$v_g = \frac{d\omega}{dk}. \quad (2.4.1)$$

Furthermore two waveguide modes are identified in Figure 2.3 - an even and odd modes band. The even modes band are the 'hockey stick'-shaped band upon which the fast and slow light region is indicated. The hill-shaped band is the odd modes band. This thesis only deals with even modes, due to their larger group velocity and thereby their larger confinement in the waveguide region.

There are many types of 2D PhCs, but in this project only two crystal types have been investigated - triangular and square crystal lattices. Such crystals are seen in Figures 2.4 and 2.5, where air holes in a dielectric medium and dielectric rods in air are the two different ways the PhCs are illustrated. In a triangular PhC every hole/rod has 6 nearest neighbours, whereas in the square PhC every hole/rod only has 4 nearest neighbours.

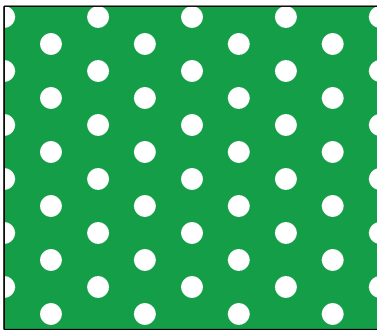


**Figure 2.4:** Photonic crystal consisting of a triangular lattice of air holes in a dielectric medium.

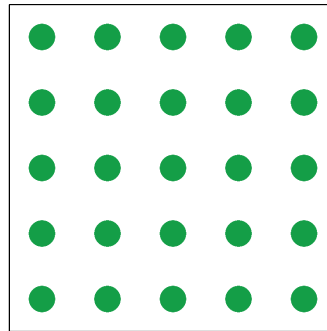


**Figure 2.5:** Photonic crystal consisting of a square lattice of dielectric rods in air.

As mentioned PhCs are most interesting when the wavelength of the light lies inside a band gap, due to the possibility of guiding the line by defects in the PhC. There are many types of defects and three of these are: point, line and broken-line defects and these three types of defects are illustrated in Figures 2.6 and 2.7. Point defects are defects where a hole/rod is removed in the PhC. This leads to a micro cavity in the PhC where light can be trapped. A line defect is where a column of holes/rods are removed and such a defect can guide light at certain wave lengths inside a band gap of the PhC, thereby acting as a waveguide. The broken-line defect is simply multiple neighbouring point defects in the same column. This leads to larger cavities than just a single point defect.

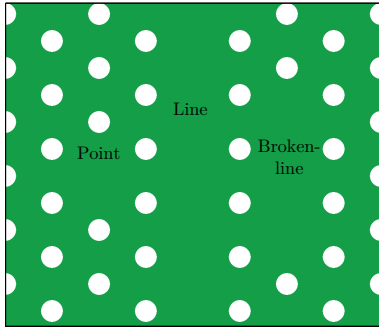


**Figure 2.6:** The different kinds of defects shown in triangular PhC.

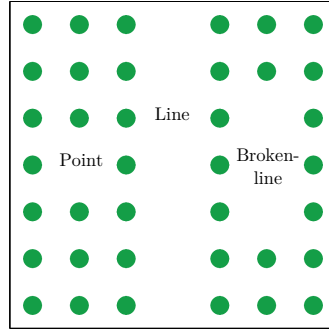


**Figure 2.7:** Photonic crystal consisting of a square lattice of dielectric rods in air.

The specific features of PhCs that appear when both waveguides and cavities are present will be introduced and explained when the results are presented in the report.

## 2D versus 3D computations

There are no such thing as a 2D PhC in real life and therefore doing 2D computations misses some physics that 3D computations takes into account. But implementing the third dimension out of the plane in Figures 2.4-2.7 is time demanding and in some cases a bit overkill. For the investigations in this project where a physical understanding on what happens when having a waveguide and a cavity close to each other a 2D computation is sufficient to do some qualitative investigations. For instance, if the Q-factor of the cavity is to be computed, then a 3D computation is needed, since light will both leak out in the plane but also out of the plane into the air modes.

The investigations performed are all in the fast light region of the band (see Figure 2.3) and fast light is more confined within the waveguide than slow light. This is seen in Figures 2.8 and 2.9, where the magnetic field mode,  $H_y$ , distribution of fast and slow light in a 2D PhC are plotted respectively. As seen in Figure 2.8 the fast light mode is very confined within the waveguide making 2D computations a good approximation for the 3D PhC slab, whereas for slow light 2D computations are not a good approximation since the mode profile extents further out both into the bulk, but also into the air. In a PhC slab a large part of the slow light will thereby be in the air region and this demands either a 3D computation or a 2D effective medium computation, where an effective refractive index is used to account for the extension of the light into the air. So as long as the

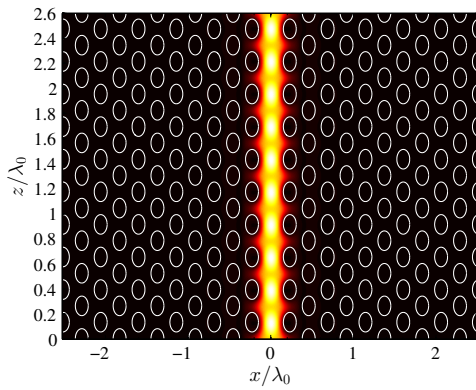


**Figure 2.8:** Distribution of fast light in a PhC waveguide. As seen the mode is very confined within the waveguide region.  $\omega = 0.26(2\pi c/a)$  in Figure 2.3.

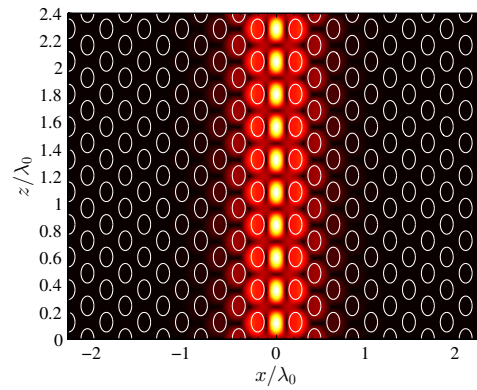


**Figure 2.9:** Distribution of slow light in a PhC waveguide. As seen the mode is extending out of the waveguide region.  $\omega = 0.24(2\pi c/a)$  in Figure 2.3.

computations are for fast light and only for qualitative purposes, 2D computations are sufficient.



---

## Computational Method

This chapter goes through the computational method used for obtaining optical properties of PhC microcavities and waveguides. The method used is the Fourier Modal method and the first section of this chapter goes through this method in detail with some derivations left out in Appendix B. Then an overview of the implementation of the method is provided followed by a validation of the implemented method, by reproduction of results from the literature. The chapter ends with a discussion on why the Fourier modal method is suitable for simulations on PhCs and the final section gives examples of observed numerical errors in the computational results.

### 3.1 The Fourier Modal Method

In section 2.3 the 2D eigenvalue problem for slab waveguides was given and solving these eigenvalue problems (equations (2.3.17) and (2.3.19)) in all layers in a structure is the first step towards computing the full 2D electromagnetic field inside any PhC structure.

#### Solving the 2D eigenvalue problem

As mentioned there are two cases of interest when investigating electromagnetic waves propagating through a waveguide - when the wave is TE polarized and when it is TM polarized. In section 2.3 the eigenvalue problems for these cases were given and now it is time to solve these equations ((2.3.17) and (2.3.19)) in each layer. In Figure 3.1 a single layer geometry is illustrated, where there is no variation in the refractive index in the propagation direction ( $z$ -direction).

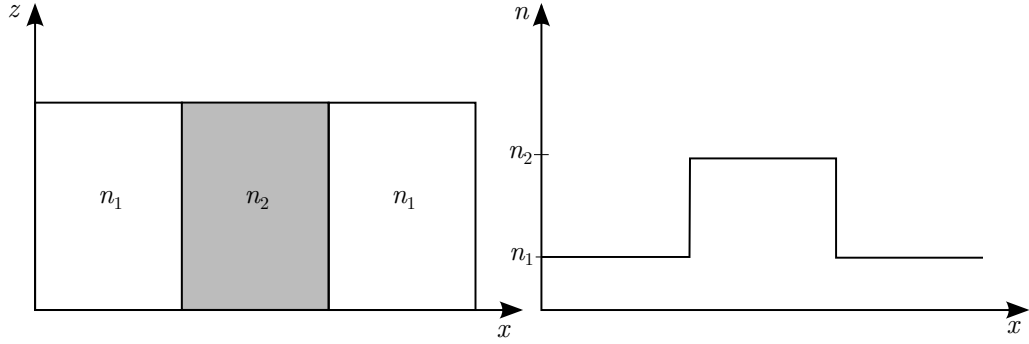


**Figure 3.1:** Illustration of one layer, where there is no variation in the refractive index in the  $z$ -direction. The refractive index profile for the layer is seen to the right.

**TM Polarization** The eigenvalue problem for TM polarization given in equation (2.3.19) is rewritten:

$$\partial_x^2 h_y + \varepsilon(x) k_0^2 h_y - (\partial_x \ln \varepsilon(x)) \partial_x h_y = \beta^2 h_y \quad \Rightarrow \quad (3.1.1)$$

$$\varepsilon(x) \left( \partial_x \frac{1}{\varepsilon(x)} \partial_x + k_0^2 \right) h_y = \beta^2 h_y. \quad (3.1.2)$$

The field mode profiles are expanded as plane waves:

$$h_{ym}(x) = \sum_{j=-M}^{j=M} v_{m,j} \exp(i(jK + \alpha/Lx)x), \quad (3.1.3)$$

$$e_{xm}(x) = \sum_{j=-M}^{j=M} u_{m,j} \exp(i(jK + \alpha/Lx)x), \quad (3.1.4)$$

$$e_{zm}(x) = \sum_{j=-M}^{j=M} w'_{m,j} \exp(i(jK + \alpha/Lx)x), \quad (3.1.5)$$

and the dielectric constant and its inverse are expanded on plane wave as well:

$$\varepsilon(x) = \sum_{j=-M}^{j=M} \varepsilon_j \exp(ijKx), \quad (3.1.6)$$

$$\frac{1}{\varepsilon(x)} = \sum_{j=-M}^{j=M} a_j \exp(ijKx), \quad (3.1.7)$$

$$(3.1.8)$$

where the elements  $\varepsilon_j$  and  $a_j$  are given by the integrals:

$$\varepsilon_j = \frac{1}{L_x} \int_0^{L_x} \varepsilon(x) \exp(-ijKx) dx, \quad (3.1.9)$$

$$a_j = \frac{1}{L_x} \int_0^{L_x} \frac{1}{\varepsilon(x)} \exp(-ijKx) dx, \quad (3.1.10)$$

which for the simple dielectric profiles considered in this report can be evaluated analytically, since  $\varepsilon(x)$  is piecewise constant (a step function) in each layer of the PhC-structures. See Appendix B.2 for the evaluation.

In order to put equation 3.1.2 into matrix form we need to employ Li's Factorization Rules (see Appendix B.1). Thereby the type of the products:  $(1/\varepsilon(x))\partial_x h_y$  and  $\varepsilon(x) (\partial_x(1/\varepsilon(x))\partial_x + k_0^2) h_y$ , need to be determined.

Physically it is required that all field components tangential to the variation in the dielectric constant,  $\varepsilon$ , must be continuous. For TM polarization this means that  $h_y$  and  $e_z$  is continuous. Maxwell's equation in the frequency domain (equation (2.1.11) with  $\mathbf{J}_s(\mathbf{r}) = 0$ ) then gives the following relation between  $h_y$  and  $e_z$  [16]:

$$e_z = \frac{i}{\omega\varepsilon_0\varepsilon} \partial_x h_y, \quad (3.1.11)$$

and since  $e_z$  is continuous,  $(1/\varepsilon)\partial_x h_y$  also has to be continuous. Both  $1/\varepsilon$  and  $\partial_x h_y$  are discontinuous functions, so therefore their product is of type 2 (see Appendix B.1 for details) and the fastest convergence is given by equation (B.1.9). The total product,  $\varepsilon (\partial_x(1/\varepsilon)\partial_x + k_0^2) h_y$ , thus consists of two discontinuous function:  $\varepsilon$  and the parenthesis times  $h_y$ , and since their product equals a continuous function,  $\beta^2 h_y$ , the product is of type 2. Thereby equation (3.1.2) is written in matrix form by applying the inverse product rule twice [16]:

$$\overline{\overline{A}}^{-1} \left( \overline{\overline{KE}}^{-1} \overline{\overline{K}} + k_0^2 \overline{\overline{I}} \right) \overline{v} = \beta^2 \overline{v}, \quad (3.1.12)$$

where  $\overline{\overline{A}}$  is the Toeplitz matrix with elements  $a_j$  given in equation (3.1.10),  $\overline{\overline{K}}$  is the  $N \times N$  matrix with diagonal elements  $(iK[-M\dots M] + i\alpha/L_x)$ ,  $\overline{\overline{E}}$  is the Toeplitz matrix with elements  $\varepsilon_j$  given in equation (3.1.9),  $k_0 = 2\pi/\lambda$  and  $\overline{\overline{I}}$  is the identity matrix. The definition of the Toeplitz matrix is given in equation (B.1.7) in Appendix B.1. The elements of  $\overline{\overline{K}}$  comes from differentiating equation (3.1.3) with respect to  $x$ .

Using equation (2.1.11) the electric field component  $e_x$  is found as:

$$e_x = \frac{\beta}{\omega\varepsilon_0\varepsilon(x)} h_y. \quad (3.1.13)$$

Now using the direct rule on equation (3.1.13) (since  $(1/\varepsilon(x))h_y$  is discontinuous and thus of type 1) and the inverse rule on equation (3.1.11) (since  $(1/\varepsilon)\partial_x h_y$  is continuous as discussed above) the electric field expansion vectors are found as [16]:

$$\bar{u}_m = \frac{\beta_m \bar{A} \bar{v}_m}{\omega \varepsilon_0}, \quad (3.1.14)$$

$$\bar{w}'_m = \frac{i}{\omega \varepsilon_0} \bar{E}^{-1} \bar{K} \bar{v}_m. \quad (3.1.15)$$

Thereby all three field components of the TM polarized electromagnetic field are found.

**TE Polarization** For TE polarization the eigenvalue equation is given in equation (2.3.17) and for simplicity the equation is stated once more here:

$$\partial_x^2 e_y + \varepsilon(x) k_0^2 e_y = \beta^2 e_y, \quad (\text{TE}). \quad (3.1.16)$$

As for the TM polarization the field modes are expanded as plane waves:

$$e_{ym}(x) = \sum_{j=-M}^{j=M} u_{m,j} \exp(i(jK + \alpha/Lx)x), \quad (3.1.17)$$

$$h_{xm}(x) = \sum_{j=-M}^{j=M} v_{m,j} \exp(i(jK + \alpha/Lx)x), \quad (3.1.18)$$

$$h_{zm}(x) = \sum_{j=-M}^{j=M} w_{m,j} \exp(i(jK + \alpha/Lx)x), \quad (3.1.19)$$

$$(3.1.20)$$

and the dielectric constant is still expanded as in equation (3.1.6). For TE polarization  $e_y$  and  $h_z$  is continuous, since these fields are tangential to the variation in the refractive index,  $n = \sqrt{\varepsilon}$ . From equation (2.1.10) the relation between  $e_y$  and  $h_z$  is found to be:

$$h_z = \frac{-i}{\omega \mu_0} \partial_x e_y. \quad (3.1.21)$$

In equation (3.1.16) the product  $\varepsilon(x)e_y$  must be of type 1, since  $\varepsilon(x)$  is a discontinuous function and  $e_y$  is continuous and thus their product must be discontinuous. Thereby the direct rule gives the fastest convergence according to Li's Factorization rules (see Appendix B.1). Equation (3.1.16) can thus be written in matrix form as [16]:

$$\left( \bar{K}^2 + k_0^2 \bar{E} \right) \bar{u} = \beta^2 \bar{u}, \quad (3.1.22)$$

where  $\bar{K}$ ,  $k_0$  and  $\bar{E}$  are stated above.

$h_x$  is found from Maxwell's equation (2.1.10) and this gives:

$$h_x = -\frac{\beta}{\omega \mu_0} e_y. \quad (3.1.23)$$

Using equations (3.1.21) and (3.1.23) the Fourier series of the magnetic mode profiles with mode number  $m$  are determined as:

$$\overline{v}_m = -\frac{\beta_m}{\omega\mu_0}\overline{u}_m \quad (3.1.24)$$

$$\overline{w}_m = \frac{-1}{i\omega\mu_0}\overline{\overline{K}}\overline{u}_m. \quad (3.1.25)$$

Thereby the eigenmodes in each layer of the PhC is found by solving either equation (3.1.12) or (3.1.22) depending on the wanted polarization and then using the relations between the Fourier coefficients stated in either equations (3.1.14) and (3.1.15) for TM polarization or equations (3.1.24) and (3.1.25) for TE polarization. In Matlab these equations are solved by using the EIG command and this gives all the eigenvectors as the columns in a matrix and all the eigenvalues in a diagonal matrix.

For layers of uniform refractive index, that is  $\varepsilon(x) = \varepsilon_1$ , there is no reason to solve the eigenvalue problem, since the solutions are already known. For such layers the eigenvectors are the columns of a diagonal matrix with 1 in the diagonal and with eigenvalues  $\beta^2 = \varepsilon k_0^2 - (mK + \alpha/L_x)^2$ , where  $m = -M \dots M$ .

Having determined the eigenmodes in each layer it is time for investigating what happens at the layer interfaces.

### Transmission and reflection at layer interfaces

For determining the transmission and reflection at a layer interface a simple two layer geometry is considered as illustrated in Figure 3.2a.

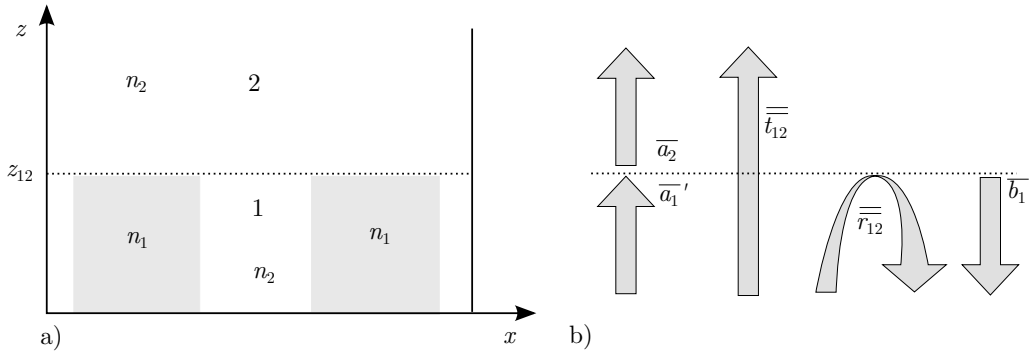


**Figure 3.2:** a) A simple two-layer geometry used in the derivation of transmission and reflection matrices between two interfaces.  $n_1$  and  $n_2$  are the refractive indices of the grey and white shaded areas respectively. b) Reflection and transmission at an interface and the field amplitudes. Note that ' (read prime) means 'pointing toward interface' and when there is no ' it means 'pointing away from interface'.

Consider the case where the bottom of the interface is illuminated with a single mode,  $a_{1n} = \delta_{mn}$ . This field is travelling forward in layer 1 as illustrated in Figure 3.2b until it reaches the interface, where it will be partly transmitted and partly reflected. By using

equations (2.3.1) and (2.3.2) and sum over all eigenmodes of the layers the electric and magnetic field in the two layers can be written as [16]:

$$\mathbf{E}_1(\mathbf{r}) = a'_{1m} \mathbf{e}_{1m}^+(\mathbf{r}_\perp) \exp(i\beta_{1m}(z - z_{12})) + \sum_{j=1}^N b_{1j} \mathbf{e}_{1j}^-(\mathbf{r}_\perp) \exp(-i\beta_{1j}(z - z_{12})), \quad (3.1.26)$$

$$\mathbf{E}_2(\mathbf{r}) = \sum_{j=1}^N a_{2j} \mathbf{e}_{2j}^+(\mathbf{r}_\perp) \exp(i\beta_{2j}(z - z_{12})), \quad (3.1.27)$$

$$\mathbf{H}_1(\mathbf{r}) = a'_{1m} \mathbf{h}_{1m}^+(\mathbf{r}_\perp) \exp(i\beta_{1m}(z - z_{12})) + \sum_{j=1}^N b_{1j} \mathbf{h}_{1j}^-(\mathbf{r}_\perp) \exp(-i\beta_{1j}(z - z_{12})), \quad (3.1.28)$$

$$\mathbf{H}_2(\mathbf{r}) = \sum_{j=1}^N a_{2j} \mathbf{h}_{2j}^+(\mathbf{r}_\perp) \exp(i\beta_{2j}(z - z_{12})), \quad (3.1.29)$$

where the sum in all four fields are over all eigenmodes in each layer.

Now the transmission and reflection matrices are introduced as  $\overline{t_{12}}$  and  $\overline{r_{12}}$  where the elements are defined by the relations [16]:

$$a_{2j} = t_{12;jm} a'_{1m}, \quad (3.1.30)$$

$$b_{1j} = r_{12;jm} a'_{1m}. \quad (3.1.31)$$

For simplicity  $a'_{1m} = 1$  in the following derivation without any loss of generality. The coefficients in the transmission and reflection matrices are found by requiring continuity of the tangential field components across the interface. That means setting  $z = z_{12}$  in equations (3.1.26) and (3.1.27) should give the same electric field and likewise for the magnetic field in equations (3.1.28) and (3.1.29). Doing this, remembering that  $\mathbf{h}^- = -\mathbf{h}^+ = -\mathbf{h}$  and  $\mathbf{e}^- = \mathbf{e}^+ = \mathbf{e}$  (as discussed in section 2.3) and using the definitions of the transmission and reflection matrix elements, the requirement of continuity leads to [16]:

$$\mathbf{e}_{\perp 1m}(\mathbf{r}_\perp) + \sum_{j=1}^N \mathbf{e}_{\perp 1j}(\mathbf{r}_\perp) r_{12;jm} = \sum_{j=1}^N \mathbf{e}_{\perp 2j}(\mathbf{r}_\perp) t_{12;jm}, \quad (3.1.32)$$

$$\mathbf{h}_{\perp 1m}(\mathbf{r}_\perp) - \sum_{j=1}^N \mathbf{h}_{\perp 1j}(\mathbf{r}_\perp) r_{12;jm} = \sum_{j=1}^N \mathbf{h}_{\perp 2j}(\mathbf{r}_\perp) t_{12;jm}. \quad (3.1.33)$$

There are now two procedures to get the transmission and reflection matrices. One using the Fourier series  $\bar{u}$  and  $\bar{v}$  and one using the eigenmodes  $\mathbf{e}_\perp$  and  $\mathbf{h}_\perp$ . [16] In this project the ladder procedure has been used so this will be gone through in details.

Before proceeding with working on equations (3.1.32) and (3.1.33) in order to determine the transmission and reflection matrices a scalar product is introduced for normalizing the mode profiles [16]:

$$\langle \mathbf{e}_m | \mathbf{h}_n \rangle = \int (\mathbf{e}_{\perp m} \times \mathbf{h}_{\perp n}) \cdot \hat{\mathbf{z}} d\mathbf{r}_{\perp} = \int (\mathbf{e}_m \times \mathbf{h}_n) \cdot \hat{\mathbf{z}} d\mathbf{r}, \quad (3.1.34)$$

where the subindex  $\perp$  is skipped in the following for simplicity. An evaluation of this integral is found in Appendix B.3 and the results for TM and TE polarization are simply stated here:

$$\langle \mathbf{e}_m | \mathbf{h}_n \rangle = L_x \sum_j u_{m,j} v_{n,-j} \quad \text{TM}, \quad (3.1.35)$$

$$\langle \mathbf{e}_m | \mathbf{h}_n \rangle = -L_x \sum_j u_{m,j} v_{n,-j} \quad \text{TE}. \quad (3.1.36)$$

These two equations are thus the  $(m, n)$ -element in a scalar product matrix between two layers. To compute all elements, it is exploited that Matlab gives the eigenvectors,  $\bar{u}$  and  $\bar{v}$ , as columns in a matrix,  $\bar{u}$  and  $\bar{v}$ , when found by using the command EIG. Thereby the scalar product is quickly computed using matrix products instead of sums. Using equations (3.1.35) and (3.1.36) the scalar product matrices between layer  $m$  and  $n$  are thus computed as:

$$\overline{\langle \mathbf{e}_m | \mathbf{h}_n \rangle} = L_x \bar{u}_m^T \bar{v}_{n,\uparrow} \quad \text{TM}, \quad (3.1.37)$$

$$\overline{\langle \mathbf{e}_m | \mathbf{h}_n \rangle} = -L_x \bar{u}_m^T \bar{v}_{n,\uparrow} \quad \text{TE}, \quad (3.1.38)$$

where  $T$  means transpose and  $\uparrow$  means that the matrix is flipped up-down - meaning that the top rows are now at the bottom and the bottom rows are now at the top of the matrix.

All eigenmodes have been normalised according to the normalization constant  $C_m = \langle \mathbf{e}_m | \mathbf{h}_m \rangle$ , by performing the substitution:  $(\mathbf{e}_m, \mathbf{h}_m) \rightarrow (\mathbf{e}_m, \mathbf{h}_m) / \sqrt{C_m}$ . The normalization constant is computed using either equation (3.1.37) or (3.1.38) depending on the polarization. After this normalization the scalar product of the field modes are orthonormal to each other  $\langle \mathbf{e}_{q,m} | \mathbf{h}_{q,n} \rangle = \delta_{mn}$ .

For uniform layers the eigenvectors as mentioned in section 3.1 are given in a diagonal matrix with 1 in the diagonal. This means that the normalization constant  $C_m = 0$  as illustrated below for TE polarization (the same is apparent for TM polarization) with the eigenvectors  $\bar{u} = (1, 0)$  and  $\bar{v} = c \cdot (1, 0)$ , where  $c$  is a constant given by equation (3.1.24).

$$\langle \mathbf{e}_m | \mathbf{h}_m \rangle = L_x \sum_j u_{m,j} v_{m,-j} = L_x c (1 \cdot 0 + 0 \cdot 1) = 0. \quad (3.1.39)$$

Therefore the linear combinations of the eigenmodes  $(1,-1)$  and  $(1,1)$  are preferable to work with, since this assures that  $C_m \neq 0$ .

Turning back to equations (3.1.32) and (3.1.33), these are written in a bra and a ket version respectively:

$$\langle \mathbf{e}_{1m} | + \sum_{j=1}^N \langle \mathbf{e}_{1j} | r_{12;jm} = \sum_{j=1}^N \langle \mathbf{e}_{2j} | t_{12;jm}, \quad (3.1.40)$$

$$| \mathbf{h}_{1m} \rangle - \sum_{j=1}^N | \mathbf{h}_{1j} \rangle r_{12;jm} = \sum_{j=1}^N | \mathbf{h}_{2j} \rangle t_{12;jm}, \quad (3.1.41)$$

and multiplying these two equations with  $| \mathbf{h}_{1n} \rangle$  and  $\langle \mathbf{e}_{1n} |$  respectively leads to:

$$\delta_{mn} + r_{12;nm} = \sum_{j=1}^N \langle \mathbf{e}_{2j} | \mathbf{h}_{1n} \rangle t_{12;jm}, \quad (3.1.42)$$

$$\delta_{mn} - r_{12;nm} = \sum_{j=1}^N \langle \mathbf{e}_{1n} | \mathbf{h}_{2j} \rangle t_{12;jm}. \quad (3.1.43)$$

Then adding and subtracting these equations gives:

$$2\delta_{mn} = \sum_{j=1}^N (\langle \mathbf{e}_{2j} | \mathbf{h}_{1n} \rangle + \langle \mathbf{e}_{1n} | \mathbf{h}_{2j} \rangle) t_{12;jm}, \quad (3.1.44)$$

$$r_{12;nm} = \frac{1}{2} \sum_{j=1}^N (\langle \mathbf{e}_{2j} | \mathbf{h}_{1n} \rangle - \langle \mathbf{e}_{1n} | \mathbf{h}_{2j} \rangle) t_{12;jm}, \quad (3.1.45)$$

and these two equations can be written in matrix form. The details on how this has been performed are seen in Appendix B.4. The resulting equations in matrix form are:

$$\overline{\overline{t}}_{12} = 2 \left( \overline{\overline{\langle \mathbf{e}_2 | \mathbf{h}_1 \rangle}}^T + \overline{\overline{\langle \mathbf{e}_1 | \mathbf{h}_2 \rangle}} \right)^{-1}, \quad (3.1.46)$$

$$\overline{\overline{r}}_{12} = \frac{1}{2} \left( \overline{\overline{\langle \mathbf{e}_2 | \mathbf{h}_1 \rangle}}^T + \overline{\overline{\langle \mathbf{e}_1 | \mathbf{h}_2 \rangle}} \right) \overline{\overline{t}}_{12}. \quad (3.1.47)$$

The PhCs simulated in this project of course consist of more than two layers, and finding the transmission and reflection matrices between any layer is simply done by replacing 1 and 2 with  $q$  and  $q + 1$ , where  $q$  is the layer number. For finding the transmission and reflection matrices when going from layer 2 to 1, then the subscripts 1 and 2 in equations (3.1.46) and (3.1.47) are simply interchanged.

### Multiple interfaces - S Matrix theory

In a multiple layer geometry not only the direct transmission and reflection between adjacent layers contribute to the total transmission and reflection properties, but also the round trips that the light can complete within each layer. Scattering matrix theory considers these round trips in the transmission and reflection matrices. Firstly, a three layer structure will be considered in order to clarify the algorithm for determining all the transmission and reflection matrices. A three-layer geometry is seen in Figure 3.3.

The structure is illuminated both from the top with mode  $n$ ,  $b'_{3n}$  and from the bottom with mode  $m$ ,  $a'_{1m}$ . The magnetic field in each layer are then given as:

$$\mathbf{H}_1(\mathbf{r}) = a'_{1m} \mathbf{h}_{1m}^+(\mathbf{r}_\perp) \exp(i\beta_{1m}(z - z_{12})) + \sum_{j=1}^N b_{1j} \mathbf{h}_{1j}^-(\mathbf{r}_\perp) \exp(-i\beta_{1j}(z - z_{12})), \quad (3.1.48)$$

$$\mathbf{H}_2(\mathbf{r}) = \sum_{j=1}^N a_{2j} \mathbf{h}_{2j}^+(\mathbf{r}_\perp) \exp(i\beta_{2j}(z - z_{12})) + \sum_{j=1}^N b_{2j} \mathbf{h}_{2j}^-(\mathbf{r}_\perp) \exp(-i\beta_{2j}(z - z_{23})), \quad (3.1.49)$$

$$\mathbf{H}_3(\mathbf{r}) = \sum_{j=1}^N a_{3j} \mathbf{h}_{3j}^+(\mathbf{r}_\perp) \exp(i\beta_{3j}(z - z_{23})) + b'_{3n} \mathbf{h}_{3n}^-(\mathbf{r}_\perp) \exp(-i\beta_{3n}(z - z_{23})), \quad (3.1.50)$$

and similar equations can be written for the electric field.

The propagation matrices in layer two are defined such that  $a'_{2j} = p_{2j}^+ a_{2j}$  and  $b'_{2j} = p_{2j}^- b_{2j}$ . The propagation constants are given as  $p_{2j}^+ = p_{2j}^- = \exp(i\beta_{2j}L_2)$ , where  $L_2 = z_{23} - z_{12}$  is the length of layer 2. Note that the forward and backward propagation constant are equal, but distinguishing between these two are important when moving on to Bloch modes, where they are no longer identical. Therefore the + and - signs are kept in order for this section to be compatible with the implementation of Bloch modes. With the above definition of the propagation constants the propagation matrices  $\overline{\overline{p}}_q^\pm$  are diagonal matrices with the propagation constants  $p_{qj}^\pm$  in the diagonal [16].

Now consider Figure 3.3. The reflection matrices  $\overline{\overline{r}}_{12}$ ,  $\overline{\overline{r}}_{21}$ ,  $\overline{\overline{r}}_{23}$  and  $\overline{\overline{r}}_{32}$  and the corresponding transmission matrices are found from equations (3.1.47) and (3.1.46).

The reflection matrix  $\overline{\overline{r}}_{13}$  has several contributions. The first contribution is the direct reflection between layer 1 and 2,  $\overline{\overline{r}}_{12}$ . But not all light is reflected at this interface. The transmitted light will propagate forward, then some of the light will be reflected at the interface between layer 2 and 3 and then propagate backward and be partly transmitted into layer 1. This journey can be described by the matrix  $\overline{\overline{t}}_{21} \overline{\overline{p}}_2^- \overline{\overline{r}}_{23} \overline{\overline{p}}_2^+ \overline{\overline{t}}_{12}$ . Only part of the light is transmitted from layer 2 to layer 1 and the light that is not transmitted is reflected once more and this round trip in layer 2 is described by the matrix  $\overline{\overline{r}}_{21} \overline{\overline{p}}_2^- \overline{\overline{r}}_{23} \overline{\overline{p}}_2^+$ . The light can then complete multiple round trips in layer 2 and for each round trip some

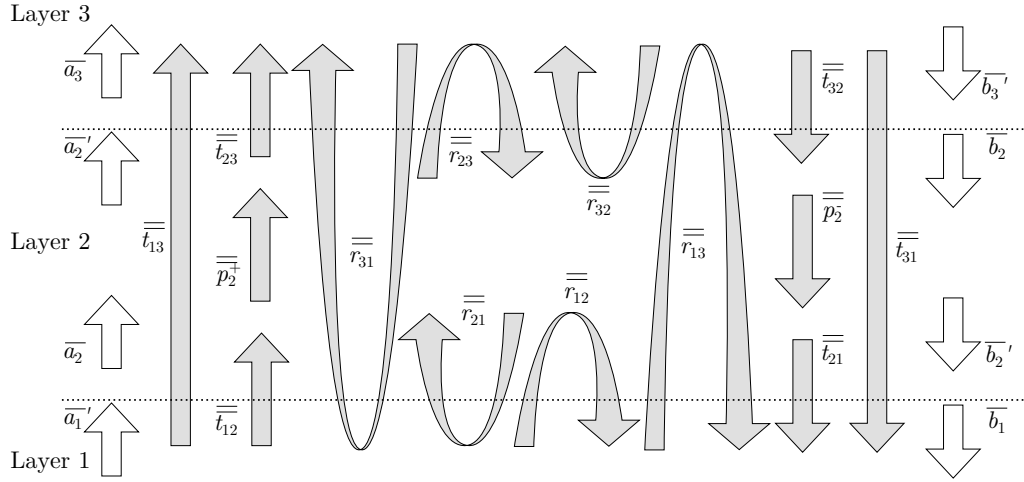


**Figure 3.3:** Illustration of the field coefficients and the transmission and reflection matrices of layer 1, 2 and 3 in a three-layer geometry.

light will transmit into layer 1 contributing to the reflection matrix,  $\overline{\overline{r}}_{13}$ , which is then given by: [16]

$$\begin{aligned} \overline{\overline{r}}_{13} = & \overline{\overline{r}}_{12} + \overline{\overline{t}}_{21} \overline{\overline{p}}_2 \overline{\overline{r}}_{23} \overline{\overline{p}}_2^+ \overline{\overline{t}}_{12} + \overline{\overline{t}}_{21} \overline{\overline{p}}_2 \overline{\overline{r}}_{23} \overline{\overline{p}}_2^+ (\overline{\overline{r}}_{21} \overline{\overline{p}}_2 \overline{\overline{r}}_{23} \overline{\overline{p}}_2^+) \overline{\overline{t}}_{12} \\ & + \overline{\overline{t}}_{21} \overline{\overline{p}}_2 \overline{\overline{r}}_{23} \overline{\overline{p}}_2^+ (\overline{\overline{r}}_{21} \overline{\overline{p}}_2 \overline{\overline{r}}_{23} \overline{\overline{p}}_2^+)^2 \overline{\overline{t}}_{12} + \overline{\overline{t}}_{21} \overline{\overline{p}}_2 \overline{\overline{r}}_{23} \overline{\overline{p}}_2^+ (\overline{\overline{r}}_{21} \overline{\overline{p}}_2 \overline{\overline{r}}_{23} \overline{\overline{p}}_2^+)^3 \overline{\overline{t}}_{12} + \dots, \end{aligned} \quad (3.1.51)$$

where the sum goes to infinity, since infinite round trips need to be taken into account. The geometric series  $\overline{\overline{I}} + \overline{\overline{M}} + \overline{\overline{M}}^2 + \overline{\overline{M}}^3 + \dots = (\overline{\overline{I}} - \overline{\overline{M}})^{-1}$ , where  $\overline{\overline{I}}$  is the identity matrix, will now be applied. This relation holds when the absolute eigenvalues for the matrix  $\overline{\overline{M}}$  are below 1. [16] Using this series equation 3.1.51 reduces to:

$$\overline{\overline{r}}_{13} = \overline{\overline{r}}_{12} + \overline{\overline{t}}_{21} \overline{\overline{p}}_2 \overline{\overline{r}}_{23} \overline{\overline{p}}_2^+ \left( \overline{\overline{I}} - \overline{\overline{r}}_{21} \overline{\overline{p}}_2 \overline{\overline{r}}_{23} \overline{\overline{p}}_2^+ \right)^{-1} \overline{\overline{t}}_{12}. \quad (3.1.52)$$

For the transmission from layer 1 to 3,  $\overline{\overline{t}}_{13}$ , there is likewise two contributions: the direct contribution where the light is transmitted from layer 1 to 2 and then propagating forward in layer 2 and finally is transmitted to layer 3, and the round trip contribution where light completes the same round trip in layer 2 as described above. The result is:

$$\overline{\overline{t}}_{13} = \overline{\overline{t}}_{23} \overline{\overline{p}}_2^+ \left( \overline{\overline{I}} - \overline{\overline{r}}_{21} \overline{\overline{p}}_2 \overline{\overline{r}}_{23} \overline{\overline{p}}_2^+ \right)^{-1} \overline{\overline{t}}_{12}. \quad (3.1.53)$$

The reflection and transmission matrices from layer 3 to 1 are found with the same considerations above. The same round trip matrix as before,  $\overline{\overline{r}}_{21} \overline{\overline{p}}_2 \overline{\overline{r}}_{23} \overline{\overline{p}}_2^+$ , is used since it might be numerically preferable only to calculate this inverse matrix once. [16] The resulting matrices are:

$$\overline{\overline{r}}_{31} = \overline{\overline{r}}_{32} + \overline{\overline{t}}_{23} \overline{\overline{p}}_2^+ \left( \overline{\overline{I}} - \overline{\overline{r}}_{21} \overline{\overline{p}}_2^- \overline{\overline{r}}_{23} \overline{\overline{p}}_2^+ \right)^{-1} \overline{\overline{r}}_{21} \overline{\overline{p}}_2^- \overline{\overline{t}}_{32}, \quad (3.1.54)$$

$$\overline{\overline{t}}_{31} = \overline{\overline{t}}_{21} \overline{\overline{p}}_2^- \overline{\overline{t}}_{32} + \overline{\overline{t}}_{21} \overline{\overline{p}}_2^- \overline{\overline{r}}_{32} \overline{\overline{p}}_2^+ \left( \overline{\overline{I}} - \overline{\overline{r}}_{21} \overline{\overline{p}}_2^- \overline{\overline{r}}_{23} \overline{\overline{p}}_2^+ \right)^{-1} \overline{\overline{r}}_{21} \overline{\overline{p}}_2^- \overline{\overline{t}}_{32}. \quad (3.1.55)$$

The field expansion vectors in layer 1 and 3 are thus easily computed as:  $\overline{\overline{a}}_3 = \overline{\overline{t}}_{13} \overline{\overline{a}}_1' + \overline{\overline{r}}_{31} \overline{\overline{b}}_3'$  and  $\overline{\overline{b}}_1 = \overline{\overline{r}}_{13} \overline{\overline{a}}_1' + \overline{\overline{t}}_{31} \overline{\overline{b}}_3'$ . The expansion vectors inside layer 2 both has the direct and the round trip contributions from the illuminating fields,  $\overline{\overline{a}}_1'$  and  $\overline{\overline{b}}_3'$ . For  $\overline{\overline{a}}_2$  the round trip matrix is chosen as  $\overline{\overline{r}}_{21} \overline{\overline{p}}_2^- \overline{\overline{r}}_{23} \overline{\overline{p}}_2^+$  and using the same geometric series as above the  $\overline{\overline{a}}_2$  expansion vector become [16]:

$$\overline{\overline{a}}_2 = \left( \overline{\overline{I}} - \overline{\overline{r}}_{21} \overline{\overline{p}}_2^- \overline{\overline{r}}_{23} \overline{\overline{p}}_2^+ \right)^{-1} \left( \overline{\overline{t}}_{12} \overline{\overline{a}}_1' + \overline{\overline{r}}_{21} \overline{\overline{p}}_2^- \overline{\overline{t}}_{32} \overline{\overline{b}}_3' \right). \quad (3.1.56)$$

The corresponding expression for the expansion vector for the backward propagating wave in layer 2,  $\overline{\overline{b}}_2$ , is [16]:

$$\overline{\overline{b}}_2 = \left( \overline{\overline{I}} - \overline{\overline{r}}_{23} \overline{\overline{p}}_2^+ \overline{\overline{r}}_{21} \overline{\overline{p}}_2^- \right)^{-1} \left( \overline{\overline{r}}_{23} \overline{\overline{p}}_2^+ \overline{\overline{t}}_{12} \overline{\overline{a}}_1' + \overline{\overline{t}}_{32} \overline{\overline{b}}_3' \right). \quad (3.1.57)$$

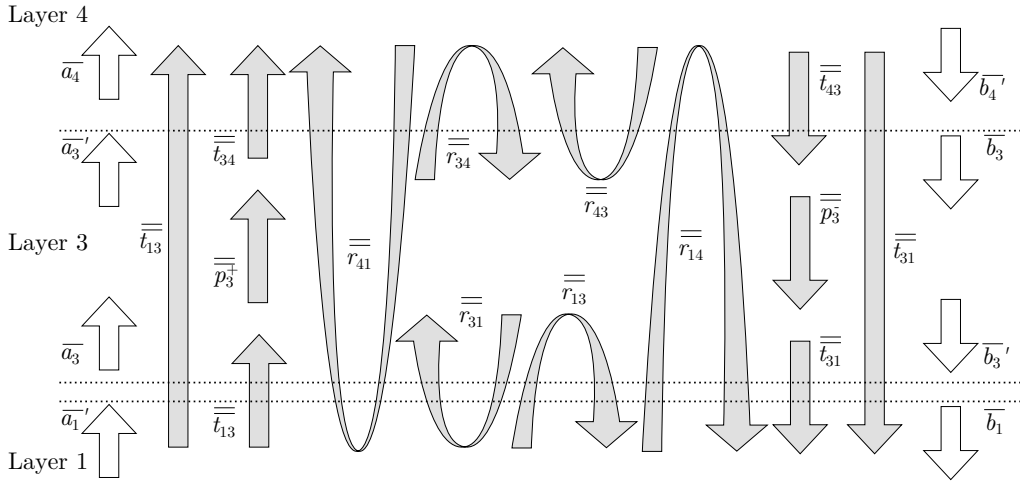


**Figure 3.4:** Illustration of the field coefficients and the transmission and reflection matrices of layer 1, 3 and 4 in a four-layer geometry.

Now that the reflection and transmission matrices for the three-layer geometry has been determined, the next step is to consider an  $N$ -layer geometry as sketched in Figure 3.5. The method for determining all the transmission and reflection matrices is simply to conceptually reduce the  $N$ -layer geometry to a three-layer structure. The first step is of course to determine all reflection and transmission matrices between neighbouring layers by using equations (3.1.47) and (3.1.46). Then  $\overline{\overline{r}}_{13}$ ,  $\overline{\overline{t}}_{13}$ ,  $\overline{\overline{r}}_{31}$  and  $\overline{\overline{t}}_{31}$  can be determined

using equations (3.1.52)-(3.1.55). The next step is thus to calculate  $\overline{\overline{r_{14}}}$ ,  $\overline{\overline{t_{14}, r_{41}}}$  and  $\overline{\overline{t_{41}}}$  and this is done by using equations (3.1.52)-(3.1.55) one more time and exchanging all 3's with 4's and all 2's with 3's. This is illustrated in Figure 3.4. This iterative procedure is repeated until layer  $N$ . The recursive relations for the scattering matrices concerning layer 1 and  $q$  are thus [16]:

$$\overline{\overline{r_{1,q+1}}} = \overline{\overline{r_{1q}}} + \overline{\overline{t_{q1} p_q^-}} \overline{\overline{r_{q,q+1} p_q^+}} \left( \overline{\overline{I}} - \overline{\overline{r_{q1} p_q^-}} \overline{\overline{r_{q,q+1} p_q^+}} \right)^{-1} \overline{\overline{t_{1q}}}, \quad (3.1.58)$$

$$\overline{\overline{t_{1,q+1}}} = \overline{\overline{t_{q,q+1} p_q^+}} \left( \overline{\overline{I}} - \overline{\overline{r_{q1} p_q^-}} \overline{\overline{r_{q,q+1} p_q^+}} \right)^{-1} \overline{\overline{t_{1q}}}, \quad (3.1.59)$$

$$\overline{\overline{r_{q+1,1}}} = \overline{\overline{r_{q+1,q}}} + \overline{\overline{t_{q+1,q} p_q^+}} \left( \overline{\overline{I}} - \overline{\overline{r_{q1} p_q^-}} \overline{\overline{r_{q,q+1} p_q^+}} \right)^{-1} \overline{\overline{r_{q1} p_q^-}} \overline{\overline{t_{q+1,q}}}, \quad (3.1.60)$$

$$\overline{\overline{t_{q+1,1}}} = \overline{\overline{t_{q1} p_q^-}} \overline{\overline{t_{q+1,q}}} + \overline{\overline{t_{q1} p_q^-}} \overline{\overline{r_{q+1,q} p_q^+}} \left( \overline{\overline{I}} - \overline{\overline{r_{q1} p_q^-}} \overline{\overline{r_{q,q+1} p_q^+}} \right)^{-1} \overline{\overline{r_{q1} p_q^-}} \overline{\overline{t_{q+1,q}}}, \quad (3.1.61)$$

where  $q$  is the layer number and is iterated from layer 2 to  $N - 1$ .

To obtain the relations relating the  $N$ 'th layer with layer  $q - 1$ , the iteration is from layer  $N - 1$  to 2 instead of layer 2 to  $N - 1$  as above. These relations are found with similar considerations as for the relations above - that is conceptually reducing the  $N$ -layer geometry to a three-layer structure and in that way iterate through all the layers. The resulting relations are [16]:

$$\overline{\overline{r_{q-1,N}}} = \overline{\overline{r_{q-1,q}}} + \overline{\overline{t_{q,q-1} p_q^-}} \overline{\overline{r_{q,N} p_q^+}} \left( \overline{\overline{I}} - \overline{\overline{r_{q,q-1} p_q^-}} \overline{\overline{r_{q,N} p_q^+}} \right)^{-1} \overline{\overline{t_{q-1,q}}}, \quad (3.1.62)$$

$$\overline{\overline{t_{q-1,N}}} = \overline{\overline{t_{q,N} p_q^+}} \left( \overline{\overline{I}} - \overline{\overline{r_{q,q-1} p_q^-}} \overline{\overline{r_{q,N} p_q^+}} \right)^{-1} \overline{\overline{t_{q-1,q}}}, \quad (3.1.63)$$

$$\overline{\overline{r_{N,q-1}}} = \overline{\overline{r_{N,q}}} + \overline{\overline{t_{q,N} p_q^+}} \left( \overline{\overline{I}} - \overline{\overline{r_{q,q-1} p_q^-}} \overline{\overline{r_{q,N} p_q^+}} \right)^{-1} \overline{\overline{r_{q,q-1} p_q^-}} \overline{\overline{t_{N,q}}}, \quad (3.1.64)$$

$$\overline{\overline{t_{N,q-1}}} = \overline{\overline{t_{q,q-1} p_q^-}} \overline{\overline{t_{N,q}}} + \overline{\overline{t_{q,q-1} p_q^-}} \overline{\overline{r_{q,N} p_q^+}} \left( \overline{\overline{I}} - \overline{\overline{r_{q,q-1} p_q^-}} \overline{\overline{r_{q,N} p_q^+}} \right)^{-1} \overline{\overline{r_{q,q-1} p_q^-}} \overline{\overline{t_{N,q}}}. \quad (3.1.65)$$

All the equations (3.1.58)-(3.1.65) will from now on be referred to as the *scattering matrix formalism*. How these equations have been implemented in the code is explained in Appendix B.5.

The field expansion vectors,  $\overline{a_q}$  and  $\overline{b_q}$ , can now be computed in all layers using the matrices found using the iterative matrix formalism. By again conceptually reduce the  $N$ -layer geometry to a three-layer structure and use the same considerations of round trips inside layer  $q$ , as when deriving equations (3.1.56) and (3.1.57), the field expansion vectors inside layer  $q$  will come out as [16]:

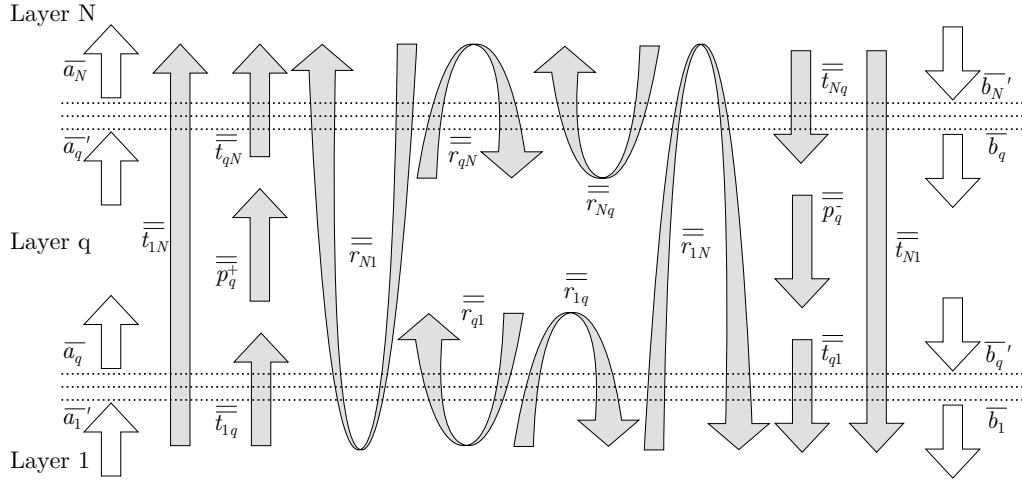


**Figure 3.5:** Illustration of the field coefficients and the transmission and reflection matrices of layer 1, q and N in a multilayer geometry.

$$\bar{a}_q = \left( \bar{I} - \bar{r}_{q1} \bar{p}_q \bar{r}_{qN} \bar{p}_q^+ \right)^{-1} \left( \bar{t}_{1q} \bar{a}'_1 + \bar{r}_{q1} \bar{p}_q \bar{t}_{Nq} \bar{b}'_N \right), \quad (3.1.66)$$

$$\bar{b}_q = \left( \bar{I} - \bar{r}_{qN} \bar{p}_q^+ \bar{r}_{q1} \bar{p}_q^- \right)^{-1} \left( \bar{r}_{qN} \bar{p}_q^+ \bar{t}_{1q} \bar{a}'_1 + \bar{t}_{Nq} \bar{b}'_N \right), \quad (3.1.67)$$

and using these field expansion vectors both the electric and magnetic field in any layer  $q$  are [16]:

$$\mathbf{E}_q(\mathbf{r}) = \sum_{j=1}^N a_{qj} \mathbf{e}_{qj}^+(\mathbf{r}_\perp) \exp(i\beta_{qj}(z - z_{q-1,q})) + \sum_{j=1}^N b_{qj} \mathbf{e}_{qj}^-(\mathbf{r}_\perp) \exp(-i\beta_{qj}(z - z_{q,q+1})), \quad (3.1.68)$$

$$\mathbf{H}_q(\mathbf{r}) = \sum_{j=1}^N a_{qj} \mathbf{h}_{qj}^+(\mathbf{r}_\perp) \exp(i\beta_{qj}(z - z_{q-1,q})) + \sum_{j=1}^N b_{qj} \mathbf{h}_{qj}^-(\mathbf{r}_\perp) \exp(-i\beta_{qj}(z - z_{q,q+1})). \quad (3.1.69)$$

Thereby both the magnetic and electric field are determined in all layers in any given geometry. However, this is the brute force way of calculating the fields when the geometries possess periodicity as is the case for PhCs. This periodicity can be exploited using Bloch's theorem which will be explained in the next section.

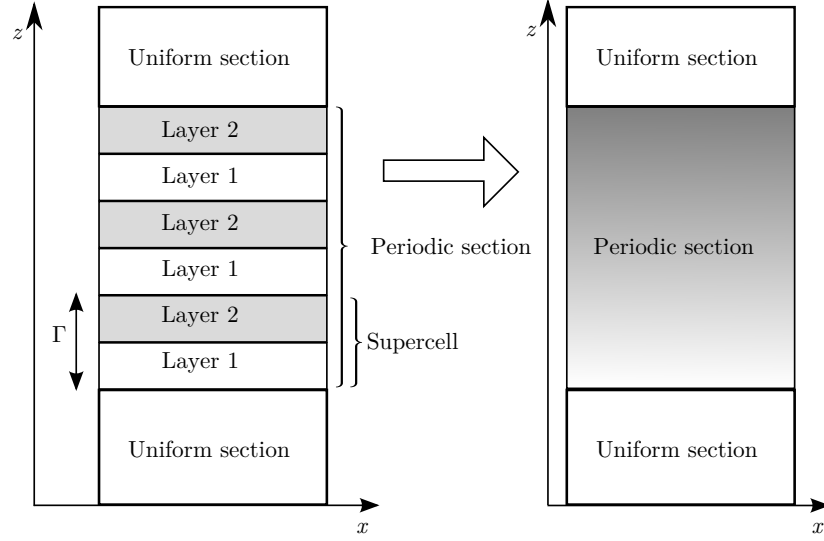


**Figure 3.6:** Illustration of how a geometry consisting of many layers is reduced to a three section geometry by exploiting the periodicity in the periodic section. Each periodic section consists of a number of supercells and these supercells again consists of a number of layers.

### Periodic structures - Bloch modes

Bloch's theorem is applicable, whenever a potential is periodic. Therefore it is natural to use Bloch's theorem on PhCs since these are indeed periodic structures and thereby possess periodic potentials. The periodicity in potential is realized with the periodicity in the dielectric function, such that  $\varepsilon(z + \Gamma) = \varepsilon(z)$ , where  $\Gamma$  is the period. Bloch's theorem then states, that the solutions to the wave equation in this periodic geometry can be written as a product of a periodic function along  $z$  and a phase term [16]:

$$\Psi_{wm}(z + \Gamma) = \Psi_{wm}(z)\Lambda_{wm}, \quad (3.1.70)$$

where  $\Psi_{wm} = (\Psi_{wm}^E, \Psi_{wm}^H)$  are referred to as the Bloch modes of the periodic section  $w$  and  $\Lambda_{wm}$  are the phase term for the  $m$ 'th Bloch mode in the  $w$ 'th periodic section. As mentioned earlier distinguishing between forward,  $\Psi_m^+$ , and backward,  $\Psi_m^-$ , propagating Bloch modes is needed. [16]. Using equation (3.1.70) the propagation of the forward and backward travelling Bloch modes over  $p$  periods inside the  $w$ 'th periodic section are described by:

$$\Psi_{wm}^+(z + p\Gamma) = \Lambda_{wm}^p \Psi_m^+, \quad (3.1.71)$$

$$\Psi_{wm}^-(z - p\Gamma) = \Lambda_{wm}^{-p} \Psi_m^+. \quad (3.1.72)$$

The electric and magnetic fields were expanded on eigenmodes inside layers with uniform refractive index in  $z$  in equations (3.1.68) and (3.1.69). The fields will now be expanded on Bloch modes instead of eigenmodes inside periodic sections instead of layers. The advantage of expanding on Bloch modes instead of eigenmodes is that a complicated

$N$ -layer structure is reduced to a problem only involving a few periodic sections. This is illustrated in Figure 3.6, where a geometry consisting of uniform sections in each end and a periodic section with many layers in between are reduced to a three-section geometry, where the periodic section is treated as one unit instead of treating all the layers within individually. For uniform sections the fields are expanded on eigenmodes as in equations (3.1.68) and (3.1.69) but in periodic sections consisting of  $p$  supercells the fields are expanded on Bloch modes as [16]:

$$\mathbf{E}_w(\mathbf{r}) = \sum_{m=1}^N (a_{wm} \Psi_{wm}^{E+}(\mathbf{r}) + b_{wm} \Psi_{wm}^{E-}(\mathbf{r})), \quad (3.1.73)$$

$$\mathbf{H}_w(\mathbf{r}) = \sum_{m=1}^N (a_{wm} \Psi_{wm}^{H+}(\mathbf{r}) + b_{wm} \Psi_{wm}^{H-}(\mathbf{r})). \quad (3.1.74)$$

The advantage of this formalism is that, the computation time is independent of the number of supercells, since once the Bloch modes in the first supercell is known Bloch's theorem gives the Bloch modes in all other supercells within the periodic section. This reduces the computation time drastically compared to the formalism of expanding the fields directly on eigenmodes.

The first step of this formalism is thus to find these Bloch modes in the supercells. For doing this the Bloch modes of the electric and magnetic field is written as a linear combination of forward and backward propagating eigenmodes relative to a position  $z'$  inside the supercell as:

$$\begin{aligned} \Psi_{wm}^{E\pm}(\mathbf{r}_\perp, z) = & \sum_{j=1}^N [c_{mj}^\pm \mathbf{e}_{qj}^+(\mathbf{r}_\perp) \exp(i\beta_j(z-z')) \\ & + d_{mj}^\pm \mathbf{e}_{qj}^-(\mathbf{r}_\perp) \exp(-i\beta_j(z-z'))], \end{aligned} \quad (3.1.75)$$

$$\begin{aligned} \Psi_{wm}^{H\pm}(\mathbf{r}_\perp, z) = & \sum_{j=1}^N [c_{mj}^\pm \mathbf{h}_{qj}^+(\mathbf{r}_\perp) \exp(i\beta_j(z-z')) \\ & + d_{mj}^\pm \mathbf{h}_{qj}^-(\mathbf{r}_\perp) \exp(-i\beta_j(z-z'))], \end{aligned} \quad (3.1.76)$$

where  $\overline{c_m^\pm}$  and  $\overline{d_m^\pm}$  are the expansion vectors for the  $m$ 'th Bloch mode at  $z = z'$ . It should be stressed that equations (3.1.75) and (3.1.76) are only valid in layer  $q$  in supercell  $w$ . Therefore  $z'$  is chosen as the position of the bottom layer interface and the eigenmodes are then those belonging to the adjacent layer above this interface. Finding the Bloch modes in all layers in all supercells in all periodic sections is only necessary when visualizing the field, which is explained in Appendix B.9. First the Bloch mode expansion vectors need to be determined.

In order to determine these a three-layer supercell is considered as sketched in Figure 3.7. Here  $z' = z_{01}$  and the field are thus expanded on the eigenmodes of layer 1. In the  $S$  matrix formalism the relation between  $\overline{c}_1$ ,  $\overline{c}_4$ ,  $\overline{d}'_1$  and  $\overline{d}''_4$  are:

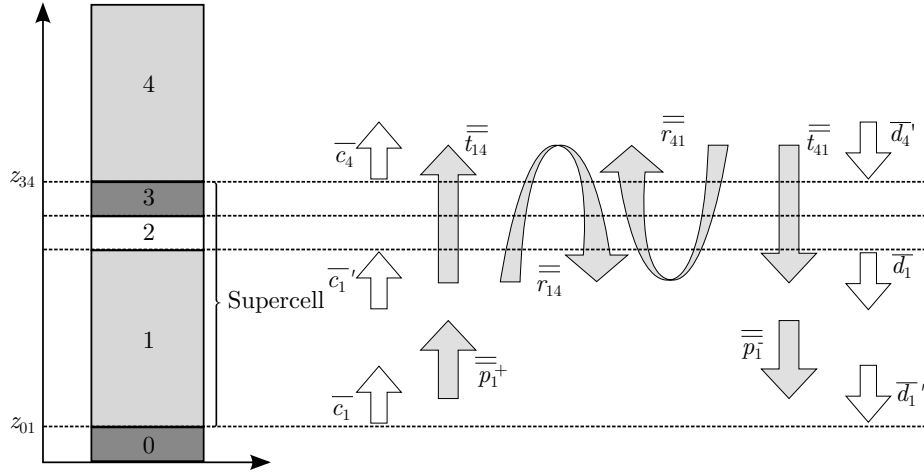


**Figure 3.7:** A three-layer supercell with transmission and reflection matrices and Bloch expansion vectors.

$$\bar{c}_4 = \bar{t}_{14} \bar{p}_1^+ \bar{c}_1 + \bar{r}_{41} \bar{d}'_4, \quad (3.1.77)$$

$$\bar{d}'_1 = \bar{p}_1^- \bar{r}_{14} \bar{p}_1^+ \bar{c}_1 + \bar{p}_1^- \bar{t}_{41} \bar{d}'_3. \quad (3.1.78)$$

These equations can be put into matrix form as:

$$\begin{bmatrix} \bar{c}_4 \\ \bar{d}'_1 \end{bmatrix} = \begin{bmatrix} \bar{S}_{11} & \bar{S}_{12} \\ \bar{S}_{12} & \bar{S}_{22} \end{bmatrix} \begin{bmatrix} \bar{c}_1 \\ \bar{d}'_4 \end{bmatrix} = \begin{bmatrix} \bar{t}_{14} \bar{p}_1^+ & \bar{r}_{41} \\ \bar{p}_1^- \bar{r}_{14} \bar{p}_1^+ & \bar{p}_1^- \bar{t}_{41} \end{bmatrix} \begin{bmatrix} \bar{c}_1 \\ \bar{d}'_4 \end{bmatrix}. \quad (3.1.79)$$

Bloch's theorem provides another relation between the expansion vectors in layer 1 and 4:

$$\begin{bmatrix} \bar{c}_4 \\ \bar{d}'_1 \end{bmatrix} = \Lambda \begin{bmatrix} \bar{c}_1 \\ \bar{d}'_1 \end{bmatrix}, \quad (3.1.80)$$

and by insertion in equation (3.1.79) the outcome is:

$$\begin{bmatrix} \bar{S}_{11} & \bar{0} \\ \bar{S}_{21} & -\bar{I} \end{bmatrix} \begin{bmatrix} \bar{c}_1 \\ \bar{d}'_1 \end{bmatrix} = \Lambda \begin{bmatrix} \bar{I} & -\bar{S}_{12} \\ \bar{0} & -\bar{S}_{22} \end{bmatrix} \begin{bmatrix} \bar{c}_1 \\ \bar{d}'_1 \end{bmatrix}, \quad (3.1.81)$$

where  $\bar{I}$  is the identity matrix and  $\bar{0}$  is the empty matrix. All matrices are of size  $N \times N$ . Equation (3.1.81) is a generalized eigenvalue problem and the steps between equations (3.1.79)-(3.1.80) and (3.1.81) are found in Appendix B.6.

Solving the generalized eigenvalue problem in equation (3.1.81) thus leads to the Bloch expansion vectors  $\bar{c}_1$  and  $\bar{d}'_1$ , and the phase term,  $\Lambda$ , for the supercell considered. It is easy to generalize this to supercells consisting of  $n$  layers simply by replacing 4 with  $n+1$

**Table 3.1:** The three different classes of Bloch modes and their propagation direction.

Class	Eigenvalue, $\Lambda_m$	Direction
I	$ \Lambda_m  < 1$	+
II	$ \Lambda_m  > 1$	-
III	$ \Lambda_m  = 1$	+ or -

in equation (3.1.79) and thereby find the scattering matrices  $\overline{\overline{S}}_{11}$ ,  $\overline{\overline{S}}_{12}$ ,  $\overline{\overline{S}}_{21}$  and  $\overline{\overline{S}}_{22}$  for any supercell.

In Matlab the EIG command is able to solve equation (3.1.81) and the first output is a  $2N \times 2N$  matrix with the  $N$  first rows being the  $\overline{c}_1$  vectors and the  $N$  last rows being the  $\overline{d}_1$  vectors, where  $N$  is the number of eigenmodes included in the calculation. The second output is a  $2N \times 2N$  diagonal matrix with the eigenvalues  $\Lambda_m$  in the diagonal.

Thereby  $N$  eigenmodes leads to  $2N$  Bloch modes where  $N$  of these are forward travelling and  $N$  are backward travelling. There are in general three classes of Bloch modes and these are given in Table 3.1.

Class I with  $|\Lambda_m| < 1$  must be forward propagating since the field cannot increase in amplitude in the propagation direction:

$$\Psi_m^+(z + \Gamma) = \Lambda_m \Psi_m^+(z), \quad (3.1.82)$$

this ensures that  $|\Psi_m^+(z + \Gamma)| < |\Psi_m^+(z)|$ . With a similar argument class II Bloch modes with  $|\Lambda_m| > 1$  must be backward propagating such that:

$$\Psi_m^-(z) = \Lambda_m \Psi_m^-(z - \Gamma), \quad (3.1.83)$$

in this way  $|\Psi_m^-(z - \Gamma)| < |\Psi_m^-(z)|$ , which ensures that the field does not blow up in the propagation direction.

In order to find the propagation direction of class III Bloch modes, the direction of the power flow,  $P_m$ , of each Bloch mode with  $|\Lambda_m| = 1$  needs to be computed. The power flow is found by integrating the  $z$ -component of its time-averaged Poynting vector as: [16]

$$P_m = \frac{1}{2} \int \text{Re} (\Psi_m^E \times \Psi_m^{H*}) \cdot \hat{\mathbf{z}} d\mathbf{r}_\perp, \quad (3.1.84)$$

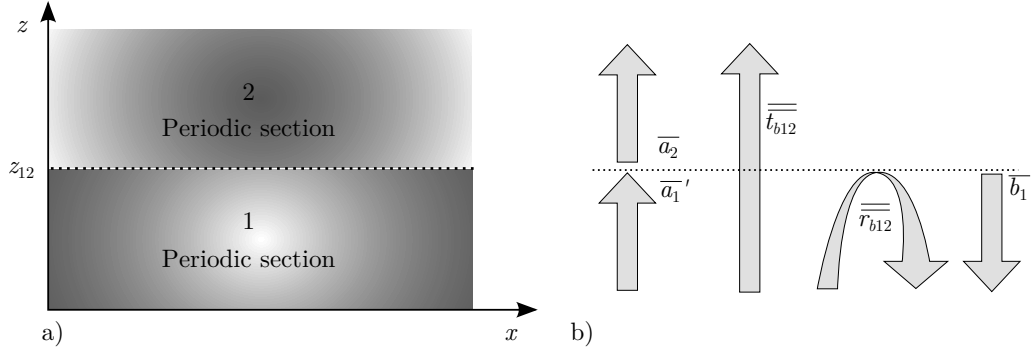
where Re and \* denotes the real part and complex conjugation respectively. This integral can be evaluated, which is done step by step in Appendix B.7 and the results for TM and TE polarization are stated here:

$$\overline{\overline{P}} = \frac{1}{2} \text{Re} \left( \overline{\overline{c}}^T \overline{\overline{W}} (\overline{\overline{c}}^* - \overline{\overline{d}}^*) + \overline{\overline{d}}^T \overline{\overline{W}} (\overline{\overline{c}}^* - \overline{\overline{d}}^*) \right) \quad \text{TM}, \quad (3.1.85)$$

$$\overline{\overline{P}} = -\frac{1}{2} \text{Re} \left( \overline{\overline{c}}^T \overline{\overline{W}} (\overline{\overline{c}}^* - \overline{\overline{d}}^*) + \overline{\overline{d}}^T \overline{\overline{W}} (\overline{\overline{c}}^* - \overline{\overline{d}}^*) \right) \quad \text{TE}, \quad (3.1.86)$$

**Table 3.2:** Scheme for determining the propagation direction of class III Bloch modes.

Power flow	Direction
$P_m > 0$	+
$P_m < 0$	-

**Figure 3.8:** a) Illustration of two adjacent periodic section at an interface. b) The Bloch transmission and reflection matrices and the Bloch mode amplitudes.

where  $\bar{c}$  and  $\bar{d}$  are matrices with those Bloch expansion vectors with  $|\Lambda_m| = 1$  in the columns. The power flows for the Bloch modes are then the diagonal elements of  $\bar{P}$ , such that  $P_m = \bar{P}(m, m) = P_{m,m}$ . The matrix  $\bar{W}$  is defined as:

$$\bar{W} = \bar{u}^T \bar{v}^* \quad (3.1.87)$$

where  $\bar{u}(\bar{v})$  is the matrix with expansion vectors in the columns of the electric (magnetic) field perpendicular to the propagation direction.

The propagation direction of class III Bloch modes are then based on the sign of  $P_m$  as shown in Table 3.2.

When all Bloch modes have been classified,  $N$  of these are forward propagating given by  $(\bar{c}_m^+, \bar{d}_m^+)$  and  $N$  of these should be backward propagating given by  $(\bar{c}_m^-, \bar{d}_m^-)$ .

### Interface between periodic sections

Having determined the Bloch modes in all periodic section of a given structure the next step is to consider what happens at the section interfaces. The steps are very similar to those leading to the transmission and reflection matrices in equations (3.1.46) and (3.1.47). Figure 3.8 illustrates the Bloch mode amplitudes and the Bloch transmission and reflection matrices at an interface.

In order to simplify the derivation of the Bloch transmission and reflection amplitudes, only a single Bloch mode field are approaching the interface from the bottom. This means that  $a'_{1n} = \delta_{mn}$  in Figure 3.8. Thereby the boundary conditions for the electric and magnetic fields expanded on Bloch modes (equations (3.1.73) and (3.1.74)) becomes [16]:

$$\Psi_{\perp 1m}^{E+}(\mathbf{r}_{\perp}) + \sum_j^N \Psi_{\perp 1j}^{E-}(\mathbf{r}_{\perp}) r_{b,12;jm} = \sum_j^N \Psi_{\perp 2j}^{E+}(\mathbf{r}_{\perp}) t_{b,12;jm}, \quad (3.1.88)$$

$$\Psi_{\perp 1m}^{H+}(\mathbf{r}_{\perp}) + \sum_j^N \Psi_{\perp 1j}^{H-}(\mathbf{r}_{\perp}) r_{b,12;jm} = \sum_j^N \Psi_{\perp 2j}^{H+}(\mathbf{r}_{\perp}) t_{b,12;jm}. \quad (3.1.89)$$

Inserting the expressions for the Bloch modes (equations (3.1.75) and (3.1.76)) into these equations and using that  $\mathbf{e}_{\perp}^{+} = \mathbf{e}_{\perp}^{-} = \mathbf{e}_{\perp}$  and  $\mathbf{h}_{\perp}^{+} = -\mathbf{h}_{\perp}^{-} = \mathbf{h}_{\perp}$ , the equations above will give:

$$\begin{aligned} \sum_l^N \mathbf{e}_{\perp 1l}(\mathbf{r}_{\perp}) \left( (c_{1ml}^{+} + d_{1ml}^{\prime+}) + \sum_j^N (c_{1jl}^{-} + d_{jl}^{\prime-}) \right) r_{b,12;jm} \\ = \sum_{j,l}^N \mathbf{e}_{\perp 2l}(\mathbf{r}_{\perp}) (c_{2jl}^{+} + d_{2jl}^{\prime+}) t_{b,12;jm}, \end{aligned} \quad (3.1.90)$$

$$\begin{aligned} \sum_l^N \mathbf{h}_{\perp 1l}(\mathbf{r}_{\perp}) \left( (c_{1ml}^{+} - d_{1ml}^{\prime+}) + \sum_j^N (c_{1jl}^{-} - d_{jl}^{\prime-}) \right) r_{b,12;jm} \\ = \sum_{j,l}^N \mathbf{h}_{\perp 2l}(\mathbf{r}_{\perp}) (c_{2jl}^{+} - d_{2jl}^{\prime+}) t_{b,12;jm}. \end{aligned} \quad (3.1.91)$$

By using the same technique of multiplying the bra version of equation (3.1.90) with  $|\mathbf{h}_{1n}\rangle$  and the ket version of equation (3.1.91) with  $\langle \mathbf{e}_{1n}|$  as in the derivation of the transmission and reflection matrices between adjacent layers (equations (3.1.46) and (3.1.47)), and then introducing matrix notation will lead to the following expressions for the transmission and reflection matrices for adjacent periodic sections [16]:

$$\begin{aligned} \overline{\overline{t}}_{b,12} = & \left[ \left( \overline{\overline{c}}_1^{-} + \overline{\overline{d}}_1^{\prime-} \right)^{-1} \overline{\overline{\langle \mathbf{e}_2 | \mathbf{h}_1 \rangle}}^T \left( \overline{\overline{c}}_2^{+} + \overline{\overline{d}}_2^{\prime+} \right) \right. \\ & \left. - \left( \overline{\overline{c}}_1^{-} - \overline{\overline{d}}_1^{\prime-} \right)^{-1} \overline{\overline{\langle \mathbf{e}_1 | \mathbf{h}_2 \rangle}} \left( \overline{\overline{c}}_2^{+} - \overline{\overline{d}}_2^{\prime+} \right) \right]^{-1} \\ & \times \left[ \left( \overline{\overline{c}}_1^{-} + \overline{\overline{d}}_1^{\prime-} \right)^{-1} \left( \overline{\overline{c}}_1^{+} + \overline{\overline{d}}_1^{\prime+} \right) - \left( \overline{\overline{c}}_1^{-} - \overline{\overline{d}}_1^{\prime-} \right)^{-1} \left( \overline{\overline{c}}_1^{+} + \overline{\overline{d}}_1^{\prime+} \right) \right], \end{aligned} \quad (3.1.92)$$

$$\overline{\overline{r}}_{b,12} = \left( \overline{\overline{c}}_1^{-} + \overline{\overline{d}}_1^{\prime-} \right)^{-1} \overline{\overline{\langle \mathbf{e}_2 | \mathbf{h}_1 \rangle}}^T \left( \overline{\overline{c}}_2^{+} + \overline{\overline{d}}_2^{\prime+} \right) \overline{\overline{t}}_{b,12} - \left( \overline{\overline{c}}_1^{-} + \overline{\overline{d}}_1^{\prime-} \right)^{-1} \left( \overline{\overline{c}}_1^{+} + \overline{\overline{d}}_1^{\prime+} \right), \quad (3.1.93)$$

and the corresponding expression for  $\overline{\overline{t}}_{b,21}$  and  $\overline{\overline{r}}_{b,21}$  are found by inverting all superscript + and - and by interchanging the indices 1 and 2. The full derivation from equations (3.1.88) and (3.1.89) to (3.1.92) and (3.1.93) are found in Appendix B.8.

All transmission and reflection matrices between periodic sections are found by using the scattering matrix formalism given in equations (3.1.58)-(3.1.65). The only thing to

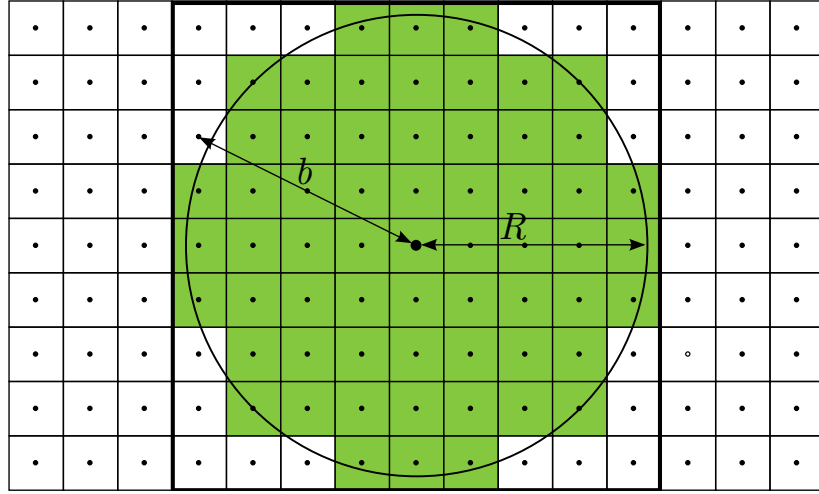


**Figure 3.9:** Illustration of how the holes/rods in the PhC is made.  $R$  is the wanted radius and  $b$  is the distance from the center of the circle to the center of the grid points within the big square. The green and white colours indicate that there is a difference in the refractive of the grid points.

remember is that the propagations matrices in periodic section  $w$ ,  $\overline{\overline{p_w^+}}$  and  $\overline{\overline{p_w^-}}$ , are in general no longer identical for forward and backward travelling waves. These are given as the diagonal matrices with  $\Lambda_m^+$  in the diagonal for forward propagation and with  $1/\Lambda_m^-$  in the diagonal for backward propagation.

When all transmission and reflection matrices between all layers in one supercell in each periodic section and all the transmission and reflection matrices relating the periodic sections have been found, the field profile in the whole geometry can be determined. This is done in Appendix B.9.

## 3.2 Overview of method implementation

In the preceding section the Fourier Modal Method has been explained and derived. This section will give a short overlook on how the method has been implemented in Matlab.

**Constructing the PhC** The first step is to construct the PhC with the defects of interest. Creating perfect circles for the holes/rods in the PhC is impossible, therefore a staircase approximation is needed. There are several ways to do this and the approximation used in this project is rather ad hoc and could/should be improved for future work. The approximation used is illustrated in Figure 3.9. When the center of a hole/rod has been found, a virtual circle is drawn with the wanted radius,  $R$ . Then for all grid points (the small squares with a dot in the center) within the big square their center distance,  $b$ , to the center of the circle is found. If  $b \leq R$ , the grid point is a part of the hole/rod of the PhC. In that way all the holes/rods and defects are made. The PhC is thus a matrix with the refractive index of each grid point as elements.

**Layers, supercells and periodic sections of PhC** After constructing the PhC and the defects, the next step is to divide it into layers, supercells and periodic sections as indicated in Figures 3.10 and 3.11.

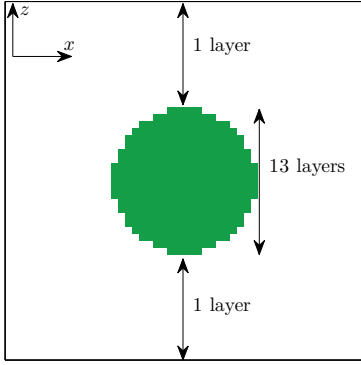


**Figure 3.10:** One rod with the layers indicated. The white region is air and the green region is a dielectric material.

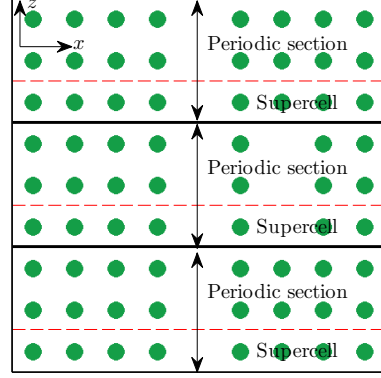


**Figure 3.11:** PhC consisting of three periodic sections, where each periodic section consists of three supercells. The black horizontal lines indicate the interface between the periodic sections and the red broken lines indicate the supercell in each section.

**Determine eigenvectors in all layers** After all the geometric considerations the eigenvalue problem for each layer is set up and solved for the polarization of interest. This is performed by first computing the  $\overline{\overline{EE}}$  Toeplitz matrix and if the polarization is TM also the  $\overline{\overline{AA}}$  Toeplitz matrix by using equations (3.1.9) and (3.1.10) respectively for computing the elements. The evaluations of these integrals in Appendix B.2 are used in practice.

Having computed these matrices either the eigenvalue problem in equation (3.1.22) or (3.1.12) is solved for all layers in the PhC depending on the wanted polarization. Then the corresponding eigenvectors are computed using either the relations in equations (3.1.24) and (3.1.25) for TE polarization or the relations given in equations (3.1.14) and (3.1.15) for TM polarization.

**Transmission and reflection at interfaces** The transmission and reflection matrices between adjacent interfaces are computed using equations (3.1.46) and (3.1.47). As seen the scalar product for the adjacent layers first needs to be computed. This is done by using either equation (3.1.38) or (3.1.37), depending on the polarization.

It should be stated that the transmission and reflection matrices are only computed for one supercell in each periodic section. The propagation matrices are also computed for one supercell per periodic section.

**Scattering matrix formalism** The next step is computing the transmission and reflection matrices between all layers in the supercells. This is done by using the scattering

matrix formalism (equations (3.1.58)- (3.1.65)) iteratively. The  $N$ 'th layer in these computations are not the last layer of the supercell but actually the first layer of the next supercell, such that the transmission matrix  $\overline{\overline{t}}_{1N}$  gives the transmission from the first layer of a supercell to the first layer of the next supercell.

**Bloch modes** The Bloch eigenvalue problem in equation (3.1.81) is set up and solved. Then the Bloch eigenvectors are characterized as either forward or backward propagating by using the schemes in Tables 3.1 and 3.2 together with either equation (3.1.86) or (3.1.85) depending on polarization.

**Transmission and reflection at periodic section interfaces** Using equations (3.1.92) and (3.1.93) the transmission and reflection matrices between adjacent periodic sections are computed. As seen the scalar product needs to be computed and this is again done by using either equation (3.1.38) or (3.1.37) - where the subindex 1 means the first layer of the periodic section *before* the interface and the subindex 2 means the first layer of the periodic section *after* the interface.

The forward and backward propagation matrices are constructed with the Bloch eigenvalues for forward and backward travelling Bloch modes in the diagonal.

**Scattering matrix formalism - periodic sections** The scattering matrix formalism in equations (3.1.58)- (3.1.65) are used to find the transmission and reflection matrices between all periodic sections.

**Visualization of the field** This part has only been done in a few cases, since it is not always necessary to visualize the magnetic or electric field. First the eigenmodes in all layers in the supercell for each periodic section is computed using either equations (3.1.17) - (3.1.19) or (3.1.3) - (3.1.5). The mode profiles are then normalized using either the scalar product in equation (3.1.38) or (3.1.37).

The Bloch modes are found in every supercell in all periodic sections using Bloch's theorem (equation (3.1.70)). The amplitude of the Bloch modes in each periodic section is computed using equations (B.9.1) and (B.9.2). Then  $\overline{a}_q^\dagger$  and  $\overline{b}_q^\dagger$  are computed for the first layer of all supercells using equations (B.9.11) and (B.9.12). Using the scattering matrix formalism for the field amplitudes in equations (3.1.66) and (3.1.67)  $\overline{a}_q^\dagger$  and  $\overline{b}_q^\dagger$  are computed for all layers in all supercells. In the end the fields are found by using equations (B.9.15) and (B.9.16).

### 3.3 Validation of method implementation

Before proceeding to do computations on new PhC waveguide and cavity designs it is important to validate that the scripts actually produce viable results. This section therefore validates the results of the implementation by comparing them with results from the literature. In [17] there are various results that can be used as benchmarks for the scripts build in this project.

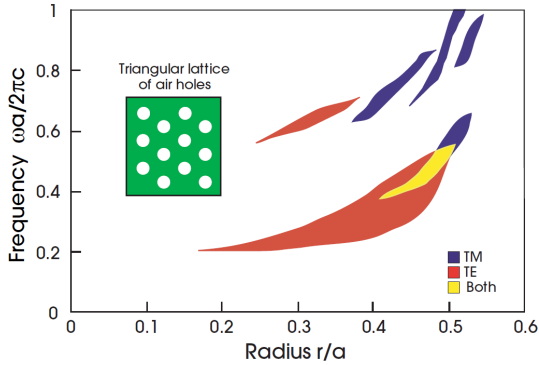


**Figure 3.12:** Figure 6 in Appendix C from [17]. The dielectric constant of the PhC medium is  $\epsilon = 11.4$ . Note that the convention in [17] regarding polarization is opposite than the one used in this thesis - such that TE is TM and vice versa.

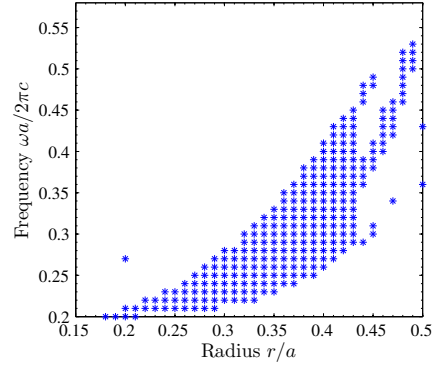


**Figure 3.13:** TM gap map of a triangular lattice of air holes with  $\epsilon = 11.4$ . For  $r/a \geq 0.44$  the gap map does not behave as in Figure 3.12. The outlying point at  $r/a = 0.2$  is due to numerical instability.

**Table 3.3:** Simulation parameters used for computing the gap map in Figure 3.13.

Number of plane waves, $N$	Number of grid points in unit cell, $N_{g,unit}$	Number of unit cells, $N_{unit}$
27	51	1

The first computations performed was so-called *gap map computations*, which essentially is a map showing, at what frequencies and radius of holes/rods in a PhC there is a band gap. In [17] results from such computations are given in the Appendix and in Figure 3.12 one of these figures has been reused for comparison purposes. In Figure 3.13 the result from doing such a gap map computation with the scripts developed in this thesis is seen. Comparing Figure 3.13 with the lower red band in Figure 3.12 it is observed that they are quite similar for  $r/a < 0.44$ . For some reason the computations gives some fishy results when  $r/a \geq 0.44$ . It is still unknown why. Furthermore a single point in Figure 3.13 at  $r/a = 0.2$  lies outside the rest of the gap map. This is due to numerical instability when using the scattering matrix formalism, where Matlab gives a warning about badly scaled matrices. The warning stems from the matrix divisions in equations (3.1.58)-(3.1.65). This warning concerning numerical instability have been observed various times and in a few cases it has affected the results. Section 3.5 discusses this.

The gap map in Figure 3.13 has been performed by using the steps in section 3.2 from the top to *Bloch modes*. If there is no Bloch eigenvalue whose absolute equals 1,  $|\Lambda_m| = 1$ , then there is a band gap for the given radius of holes/rods and at the given frequency of the light. Computing this only requires one unit cell and the unit cell used is seen in Figure 3.14. Other parameters used in the computation are seen in Table 3.3.

More gap map computations are found in Appendix C.1.

In [17] a band diagram of a square rods PhC waveguide is also found and this is seen in Figure 3.16. The result of a computation on the same structure is presented in Figure 3.17, where the PhC structure is seen in Figure 3.15. The two band diagrams are very alike and only minor differences are present. These differences could be due to the

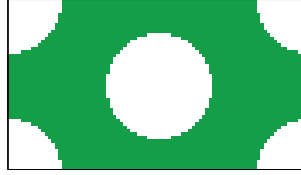


**Figure 3.14:** The unit cell of the triangular PhC of air holes used for the gap map calculations in Figure 3.13.

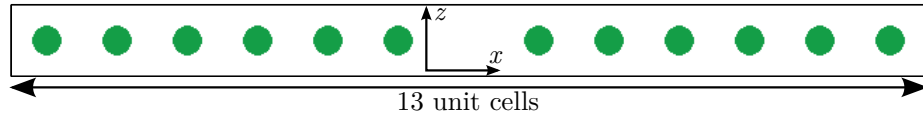


**Figure 3.15:** PhC structure used for computing the band diagram in Figure 3.17.

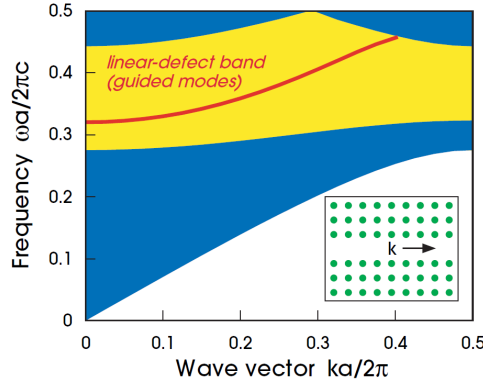


**Figure 3.16:** Figure 19 in Chapter 5 from [17]. The dielectric constant of the PhC rods are  $\epsilon = 8.9$ . The band diagram is for TE modes.

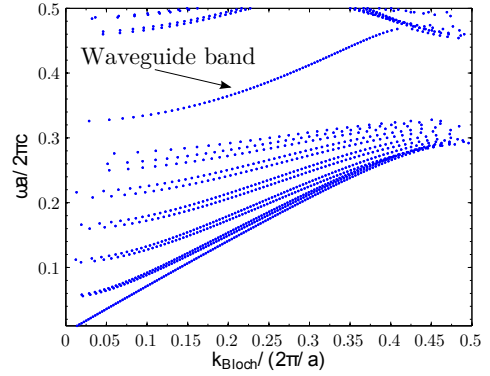


**Figure 3.17:** TE band diagram of a square rods PhC with  $\epsilon = 8.9$ . The structure is seen above in Figure 3.15.

**Table 3.4:** Simulation parameters for the band diagram in Figure 3.17.

Number of plane waves, $N$	Number of grid points in unit cell, $N_{g,unit}$	$N_{unit}$	$\epsilon_{rods}$
20	51	13	8.9

staircase approximation or to not having included enough plane waves in the expansion. The simulation parameters for Figure 3.17 are given in Table 3.4.

The developed scripts thereby produce results, that are close to those of the literature and therefore it is concluded, that the implementation of the Fourier modal method is viable. Furthermore physical inspection of the results is always a good idea - for example assuring that the fields are continuous over all interfaces is a fast and easy way of validating the code.

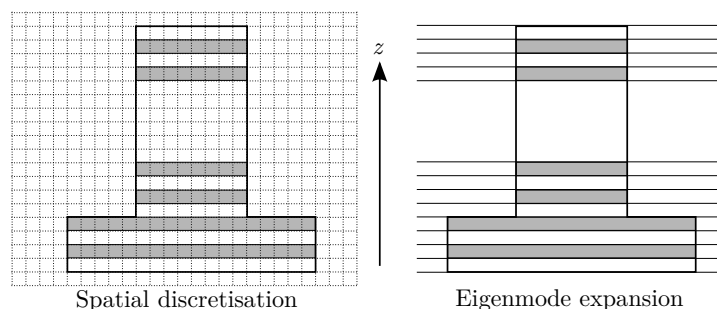


**Figure 3.18:** FDTD uses a discretisation of the structure, whereas the Fourier modal method uses an expansion on eigenmodes.

### 3.4 Why use Fourier Modal method

The Fourier modal method is only one of many methods that is able to solve Maxwell's equations in order to obtain the electromagnetic field in complex structures. Other methods include the finite-difference time-domain method (FDTD) and a semianalytical approach. In [14] these three methods are compared when simulating a 2D PhC. First of all the difference between FDTD and the Fourier modal method is that FDTD uses a spatial discretisation of the field, whereas the Fourier modal method uses an eigenmode expansion as illustrated in Figure 3.18. In a grid point expansion technique the number of grid points introduces a large number of unknowns to solve for and therefore naturally performs slower than an eigenmode expansion technique [19].

In [14] advantages and disadvantages of using semianalytical techniques, vectorial eigenmode expansion and FDTD are discussed and listed. The advantages of using vectorial eigenmode expansion (which is what the Fourier modal method is using), that has been used in this project are [14]:

1. The computation time is linear in the number of layers and do not depend on the thickness of these layers, since the propagation through layers is handled analytically. This is not the case for FDTD.
2. The possibility of introducing a Bloch mode formalism drastically decreases the computation time, when periodicity in the structure is present.
3. No reflections from the end facets of the computation domain of the PhC.

The disadvantages listed in [14] are:

1. Less advantageous if there is no repetition of layers.
2. For curved nonrectangular objects, many layers are needed.
3. The technique relies on an absorbing boundary condition.
4. If the structure is excited by waveguides running in different directions, considerable performance is lost.

The first disadvantage is not relevant for this project, since for the PhC structures considered there are indeed a repetition of layers exploited by implementing a Bloch mode expansion. The second disadvantage is present in this project, since the round holes in the PhC is realised by a staircase approximation, that becomes more precise with the number of layers used. The absorbing boundaries are not necessary in this project, due to the band gaps of the bulk PhC. The band gap secures that no light reaches the walls of the computational domain and therefore it would be overkill to implement absorbing boundaries. The fourth disadvantage is not relevant for the simulations performed.

Thereby the only disadvantage listed in [14] that is present for the simulations in this project is the second one, whereas the three advantages listed above are all relevant for the simulations performed. All the advantages and disadvantages of using a semianalytical technique or FDTD listed in [14] will not be restated here, but the biggest disadvantage of using FDTD on PhCs is that the phase errors accumulate for larger structures and this might lead to changes in the resonance frequencies, when a cavity is present [14]. The biggest disadvantage of using a semianalytical technique is the computation time.

Considering the advantages and disadvantages of an eigenmode expansion technique, the Fourier modal method is very suited for computations on PhC structures.

### 3.5 Observed errors in method implementation

The implementation of the Fourier modal method gives a 'warning' in Matlab that cannot be completely neglected, since it in some cases affects the results. When computing the scattering matrices using equations (3.1.58)-(3.1.65) the following warning has been observed: "Warning: Matrix is close to singular or badly scaled. Results may be inaccurate. RCOND = 8.798187e-17.". This warning is given when computing the matrix inverse in equations (3.1.58)-(3.1.65). For equation (3.1.58) the matrix inverse is computed in the following way in Matlab:

$$\overline{\overline{r}}_{1,q+1} = \overline{\overline{r}}_{1q} + \overline{\overline{t}}_{q1} \overline{\overline{p}}_q \overline{\overline{r}}_{q,q+1} \overline{\overline{p}}_q^+ \left( \overline{\overline{I}} - \overline{\overline{r}}_{q1} \overline{\overline{p}}_q \overline{\overline{r}}_{q,q+1} \overline{\overline{p}}_q^+ \right)^{-1} \overline{\overline{t}}_{1q} \quad (3.5.1)$$

$$= \overline{\overline{r}}_{1q} + \overline{\overline{t}}_{q1} * \overline{\overline{p}}_q * \overline{\overline{r}}_{q,q+1} * \overline{\overline{p}}_q^+ * \left( \overline{\overline{I}} - \overline{\overline{r}}_{q1} * \overline{\overline{p}}_q * \overline{\overline{r}}_{q,q+1} * \overline{\overline{p}}_q^+ \right) \setminus \overline{\overline{t}}_{1q}. \quad (3.5.2)$$

By doing the matrix inverse with the \-operator in Matlab the number of RCOND-warnings are greatly reduced, but has not completely disappeared. The matrices should not be badly scaled although some elements are approaching zero, which is the source of the warning. It should be emphasized that the warning only shows up a couple of times when computing the scattering matrices of multiple layers and in many cases the warning does not affect the results in an observable way.

In Figures 3.19 and 3.20 two computed transmission spectra for two different PhC cavity and waveguide structures are seen. The transmission spectrum in Figure 3.19 has three points that deviates from the rest but in Figure 3.20 no points deviates from the fitted line. This shows that the warning message given by Matlab in some cases affects the results such that a few points deviates from the overall trend and in some cases it does not affect the results at all. However, the source of the warning message should be

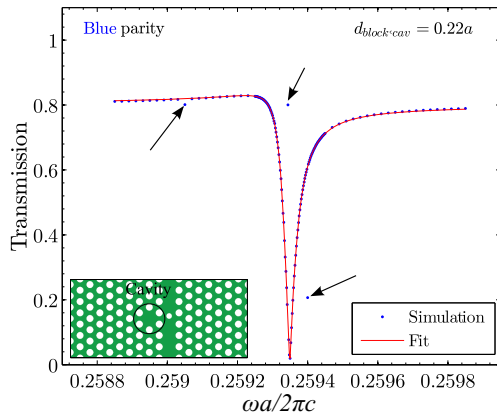


**Figure 3.19:** Transmission spectrum for a PhC cavity and waveguide structure. As seen three points deviates from the overall trend.

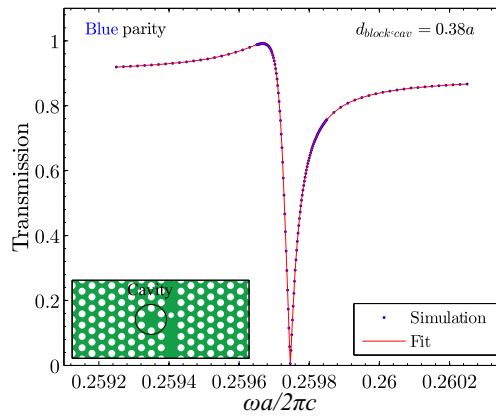


**Figure 3.20:** Transmission spectrum for a PhC cavity and waveguide structure, where no points deviates from the overall trend.

investigated, but since it has only affected the results in a negligible way this has not been prioritized.

The transmission spectra shown in Figures 3.19 and 3.20 for PhC cavity and waveguide structures will be investigated and explained more thoroughly in Chapter 4.



---

## Computations on PhC waveguides and microcavities

In this chapter the developed code is used for investigating the transmission properties of PhC waveguides when a microcavity is placed nearby. The results will be discussed and explained by using the coupled-mode theory derived in [11], [12] and [6].

### 4.1 Cavity resonances

Fano resonances has been reported in many PhC structures ([11], [6], [4], [3]) and has received a lot of attention due to the possible application as a photonic switch. The term Fano resonance stems from the Fano lineshape function, which is a function that is a result of an interaction between a Lorentzian field and a background field that does not vary over the linewidth of the Lorentzian field [20]. In the simulations performed in this project, this interaction is realised by a blocked waveguide next to a cavity such that, the light has two distinguishable paths for reaching the end of the waveguide. This is illustrated in Figure 4.1. In order to understand the origin of these Fano resonances a summary of coupled-mode theory will be given. This will also serve as the theoretical foundation for understanding and discussing the computational results presented later in this chapter.

#### Coupled-mode theory

In Figure 4.1 a blocked waveguide next to a cavity is illustrated and as mentioned above the Fano resonance is a result of an interaction between a continuous background field

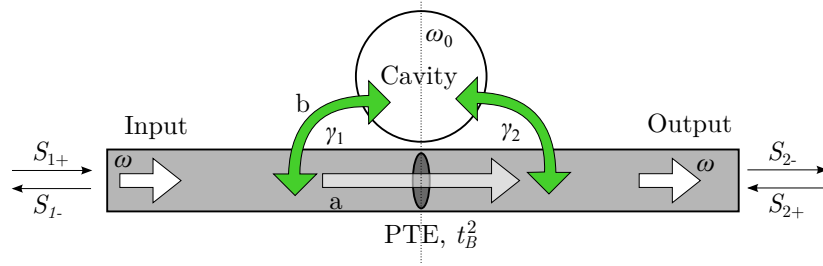


**Figure 4.1:** When the light travels through a waveguide which is blocked by a partly transmitting element, PTE, and a cavity is positioned next to the waveguide, the light can travel through two distinguishable paths - by a) transmission through the PTE or by b) coupling from the waveguide mode to the cavity mode.

and a Lorentzian field. The path a in Figure 4.1 gives the background field and the path b gives the Lorentzian field, i.e. a discrete resonance.  $\gamma_1$  and  $\gamma_2$  are the decay rates from the cavity into the input and output port. The coupling of the waveguide to the resonator (cavity) is described by temporal coupled-mode theory ([11], [12], [6], [4]) and only the most central parts will be summarized here.

Referring to Figure 4.1 the temporal coupled-mode equations are [12], [6], [13]:

$$\frac{da}{dt} = (-i\omega_0 - \gamma_1 - \gamma_2 - \gamma_v) a + (d_1 \quad d_2) \begin{pmatrix} s_{1+} \\ s_{2+} \end{pmatrix}, \quad (4.1.1)$$

$$\begin{pmatrix} s_{1-} \\ s_{2-} \end{pmatrix} = C \begin{pmatrix} s_{1+} \\ s_{2+} \end{pmatrix} + \begin{pmatrix} d_1 \\ d_2 \end{pmatrix} a, \quad C = \begin{pmatrix} r_B & -it_B \\ -it_B & r_B \end{pmatrix}, \quad (4.1.2)$$

where  $|a|^2$  is the energy in the cavity,  $\omega_0$  is the resonance frequency,  $\gamma_v$  is the intrinsic cavity loss rate,  $\gamma_1$  and  $\gamma_2$  are decay rates from the cavity into the two ports,  $s_{1+}$  and  $s_{2+}$  are the amplitudes of the incoming waves in the two ports,  $s_{1-}$  and  $s_{2-}$  are the amplitudes of the outgoing waves in the two ports, and  $d_1$  and  $d_2$  are the complex coupling coefficients between the ports and the resonance.  $C$  is the scattering matrix representing the direct coupling between the incoming and outgoing waves, where  $r_B$  and  $t_B$  are the real and positive amplitude reflection and transmission coefficients, satisfying  $r_B^2 + t_B^2 = 1$ . Due to time-reversal and energy conservation [11],  $d_1 = \sqrt{2\gamma_1} \exp(i\theta_1)$  and  $d_2 = \sqrt{2\gamma_2} \exp(i\theta_2)$ . The transmission of the system from input to output is derived from the temporal coupled-mode equations and the result is [6]:

$$t(\omega) = -it_B - \frac{2(r_B \sqrt{\gamma_1 \gamma_2} \exp(i(\theta_2 - \theta_1)) - it_B \gamma_2)}{i(\omega_0 - \omega) + \gamma_1 + \gamma_2 + \gamma_v}. \quad (4.1.3)$$

The phase factors are determined by considering time-reversal symmetry and energy conservation as performed in Appendix D.1. The result is:

$$\exp(i(\theta_2 - \theta_1)) = \frac{it_B(\gamma_2 - \gamma_1) \pm \sqrt{4\gamma_1 \gamma_2 - t_B^2(\gamma_1 + \gamma_2)^2}}{2\sqrt{(1 - t_B^2)\gamma_1 \gamma_2}}, \quad (4.1.4)$$

Inserting this equation into equation (4.1.3) leads to the following transmission function:

$$t(\omega) = \frac{t_B(\omega_0 - \omega) \pm \sqrt{4\gamma_1\gamma_2 - t_B^2(\gamma_1 + \gamma_2)^2} - it_B\gamma_v}{i(\omega_0 - \omega) + \gamma_1 + \gamma_2 + \gamma_v}. \quad (4.1.5)$$

The sign (parity) of this Fano line shape function is determined by the phase shift  $\theta_2 - \theta_1$  in equation (4.1.4). The positive (negative) sign is for blue (red) parity, where the parity is defined by whether the transmission minimum is red or blue shifted relative to the transmission maximum. Determining the phase shift between the coupling coefficients is currently done by fitting transmission curves to coupled-mode theory.

For mirror symmetric systems the decay rates into the two ports are equal,  $\gamma_1 = \gamma_2 = \gamma_{in}/2$  and the transmission function becomes [3, 4, 6]:

$$t(\omega) = t_B^2 \pm it_B r_B - \frac{\gamma_{in}}{i(\omega_0 - \omega) + \gamma_{in} + \gamma_v}. \quad (4.1.6)$$

In this equation the positive sign corresponds to a cavity mode that is odd (blue parity) with respect to the mid plane and likewise the negative sign corresponds to a cavity mode that is even (red parity) with respect to the mid plane.

If there is no PTE,  $t_b = 1$ , and the system persists mirror symmetry,  $\gamma_1 = \gamma_2 = \gamma_{in}/2$ , then the Fano line shape function in equation (4.1.6) reduces to a Lorentzian line shape function:

$$t(\omega) = 1 - \frac{\gamma_{in}}{i(\omega_0 - \omega) + \gamma_{in} + \gamma_v}. \quad (4.1.7)$$

## Finding the resonance frequency

The Fano resonances has been realised in this project as sketched in Figure 4.1, where a cavity is blocked by a partly transmitting element (PTE, blocking element) and situated next to a cavity. The PTE has been moved back and forth with respect to the mirror plane in order to investigate how the parity changes. This is illustrated in Figure 4.2.

However, before investigating Fano resonances the band diagram of the waveguide in Figure 4.2 was computed. This band diagram is found in section 2.4 in Figure 2.3 and has been reinserted here for convenience in Figure 4.3. As stated in section 2.4 the 2D computations are closest to real life for fast light - therefore the frequencies chosen should be in the fast light region. Furthermore it is noticed, that there are two bands for the wave guide modes - an even modes band (the hockey stick shaped band) and an odd modes band (the hill shaped band). The even modes band is the most interesting one, since this allows for a single mode waveguide in the fast light region and furthermore the even mode is more confined within the waveguide. Thereby the resonance frequency of the cavity should be in a fast light region, where only even modes are allowed.

The determination of the resonance frequency of the cavity has been done by illuminating the PhC-structure in Figure 4.2 from below by a range of frequencies and then looking at the transmission spectrum of the propagating waveguide mode. The first two simulations was performed without a PTE and the results of these two simulations are

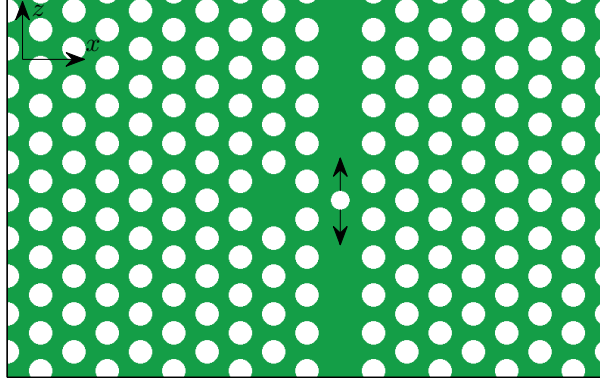


**Figure 4.2:** PhC with a blocked waveguide and a cavity. The arrows indicate that the PTE is moved back and forth relative to the mid-plane of the cavity in the simulations.

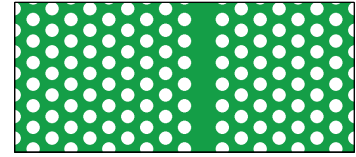
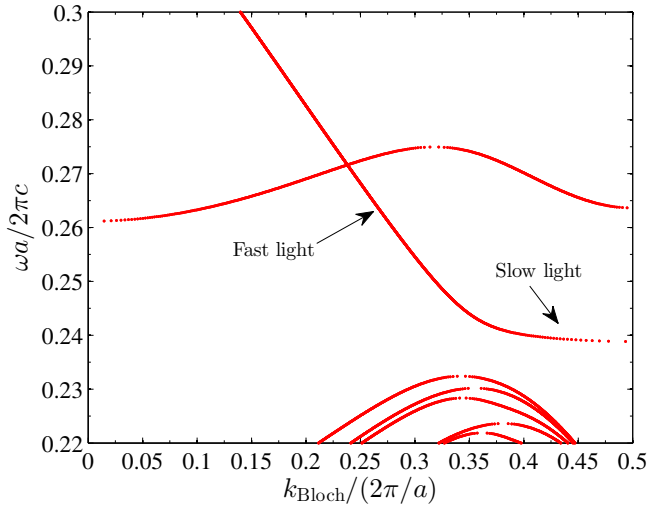


**Figure 4.4:** PhC with a line defect acting as a waveguide.

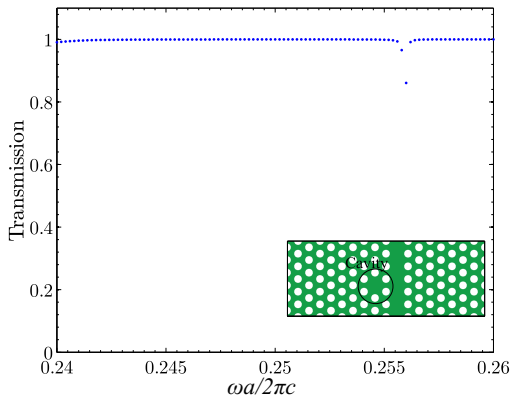
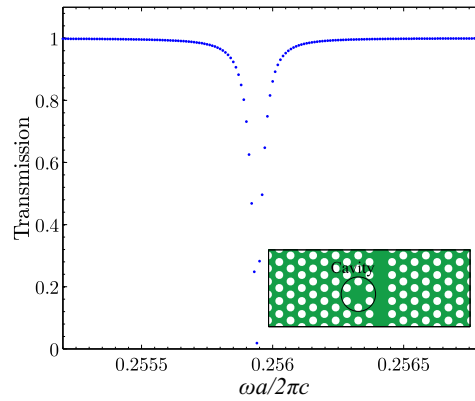
**Figure 4.3:** Band diagram for TM polarization of the PhC with a waveguide depicted in Figure 4.4. The band diagram is the one in Figure 2.3.

seen in Figures 4.6 and 4.7. The transmission spectra are Lorentzian shaped as predicted by the coupled-mode theory in equation 4.1.7. Table 4.1 provides the simulation parameters and the supercell for the waveguide region used in the computation are seen in Figure 4.5. As observed in Figure 4.7 the resonance frequency is  $\omega_0 = 0.2559 (2\pi c/a)$ , which as seen on the band diagram in Figure 4.3 is in a fast light single mode region.

The transmission spectrum is found from the Bloch transmission matrix,  $\overline{\overline{t_{b,1N}}}$ , describing the transmission of the Bloch modes from the first periodic section to the last. The transmission of the fundamental mode is then described by the first matrix element in the Bloch transmission matrix,  $t_{b,1N;11}$ , and it is the absolute of this matrix element,  $|t_{b,1N;11}|$ , that has been plotted in Figures 4.6 and 4.7. This approach is justified, since

**Table 4.1:** The simulation parameters used in the computation of the transmission spectra seen in Figures 4.6 and 4.7.

$n_b$	$n_h$	$r/a$	$N_{g_{unit}}$	Number of plane waves
3.1	1.0	0.30	81	101

**Figure 4.5:** Supercell for the geometry simulated in Figures 4.6 and 4.7.  $N_{g_{unit}}$  in Table 4.1 refers to the number of grid points used in the vertical direction for constructing one supercell. The definition of  $r$  and  $a$  is also illustrated.**Figure 4.6:** The first transmission simulation for finding the frequency range where the Fano resonance is seen.**Figure 4.7:** The second simulation, where the frequency range is narrowed based on the result from the first simulation.

only the fundamental mode is allowed to propagate in the waveguide - all higher order modes that has been excited by the interaction with the cavity will eventually extinguish. Therefore only the transmission of the fundamental mode is of interest.

## 4.2 Fano structures and parity

The Fano structures considered are as depicted in Figure 4.2, where the PTE (blocking element) has radius  $r_{block} = 0.80 r/a$  for the first set of simulations, such that the blocking element is a bit smaller than the holes in the bulk lattice. The other simulation parameters are as given in Table 4.1. The vertical distance between the center of the cavity and the center of the blocking element is varied, in order to investigate how the parity of the Fano lineshape function changes. The distance between the cavity and blocking element is defined as:  $d_{block,cav} = z_{block} - z_{cav}$ , which is illustrated in Figure 4.8.

The first Fano structure considered has mirror symmetry, i.e.  $d_{block,cav} = 0$  and the resulting transmission spectrum is seen in Figure 4.9. The spectrum has red parity, meaning that the transmission minimum is red shifted relative to the transmission maximum. Likewise blue parity is when the transmission minimum is blue shifted relative

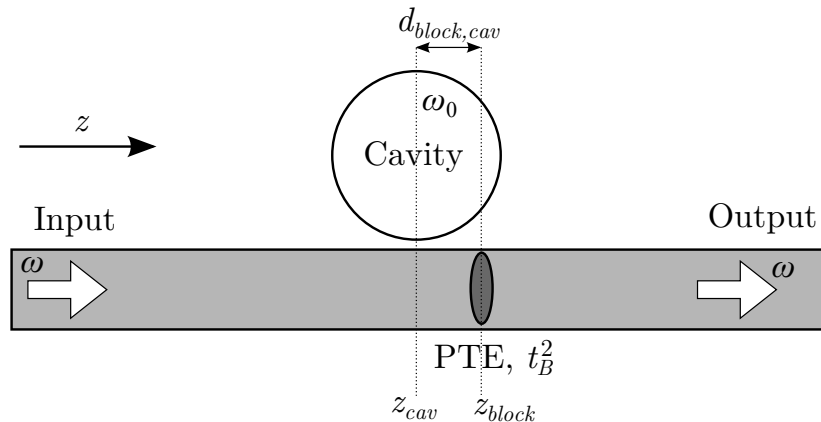


**Figure 4.8:** Illustration defining the distance between the blocking element (PTE) and the cavity.

to the transmission maximum. In the figure both the data obtained from the simulation and a curve fitted to this data are seen. The simulated data are fitted to equation (4.1.6), since the system has mirror symmetry, using Matlab's built-in `lsqcurvefit` that uses a least-squares method for determining the function parameters provided the data, starting guesses and lower and upper bounds on the parameters. It was observed that `lsqcurvefit` is highly sensitive to the starting guesses on the parameters and therefore some trial and error was needed in order to get some good fits. The fitted parameters for the transmission curve in Figure 4.9 are seen in Table 4.2.

**Table 4.2:** The fitted parameters for the simulation data presented in Figure 4.9.

$t_B$	$\omega_0$	$\gamma_{in}$	$\gamma_v$
0.7009	0.25907	$3.163 \times 10^{-5}$	$5.268 \times 10^{-10}$

The blocking element was then moved back and forth relative to the cavity position in steps of  $0.02a$ , where  $a$  is the lattice constant of the bulk PhC structure. As will be shown the resonance frequency of the cavity changes when the blocking element is moved. This is due to the cavity not being confined within the circle drawn in the inset in Figure 4.9, but instead the cavity does not have absolute borders. The cavity mode extends further out and therefore the resonance frequency changes when the environment around it is changed. Tools for determining the exact cavity mode has not been implemented in this project (an approach is suggested in [21]), but a decent approximation for the cavity mode is obtained when illuminating the waveguide with the resonance frequency of the cavity and thereby exiting the cavity mode. This has been done in order to visualise the cavity mode and the magnetic field of the TM polarized light is plotted in Figure 4.10. As seen the cavity mode extends out of the cavity and couples to the waveguide - thereby the resonance frequency of the cavity depends on the position of the blocking element. Furthermore it is noticed that the field inside the cavity has even symmetry with respect to the mid plane as expected when the transmission spectrum has red parity. Note that the field plot in Figure 4.10 is the absolute value of the field and therefore the symmetry is not directly visible. A field plot of the real value of the field is found in Appendix E in Figure E.1.

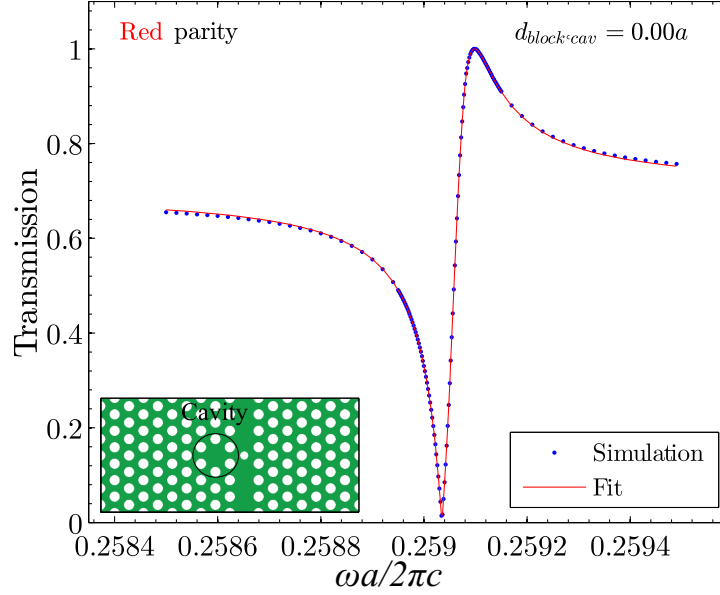


**Figure 4.9:** Transmission spectrum for symmetric Fano structure. The structure is seen in the inset.

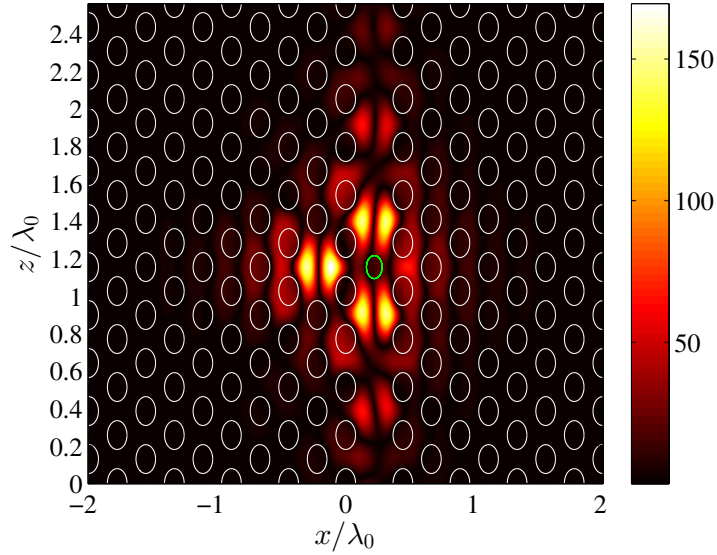


**Figure 4.10:** The absolute of the magnetic field,  $H_y$ , for the PhC structure illuminated with the cavity resonant mode. As seen the cavity mode is excited and extends out in the waveguide and the nearby environment of the cavity. The PhC structure is visualized by the white ellipses. The green ellipse indicate, that the blocking element has a different radius than the bulk holes.

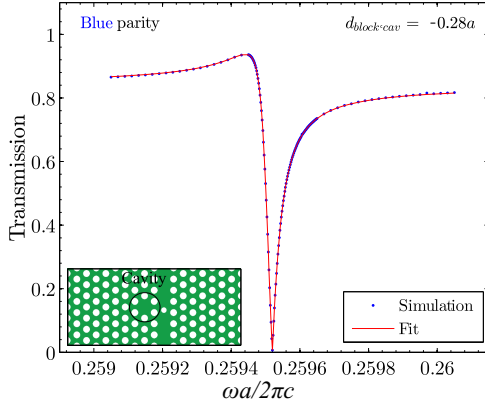


**Figure 4.11:** Transmission spectrum for  $d_{block,cav} = -0.28a$ , meaning that the blocking element is positioned  $0.28a$  before the cavity. The structure is seen in the inset.

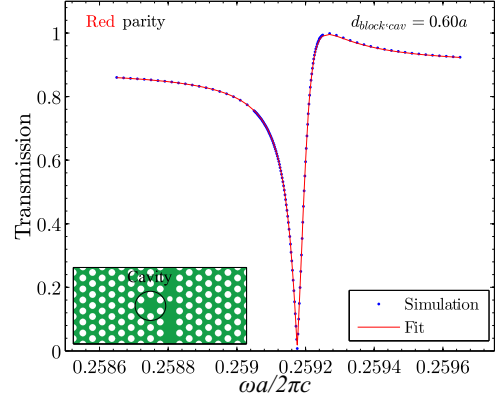


**Figure 4.12:** Transmission spectrum for  $d_{block,cav} = +0.60a$ , meaning that the blocking element is positioned  $0.60a$  after the cavity. The structure is seen in the inset.

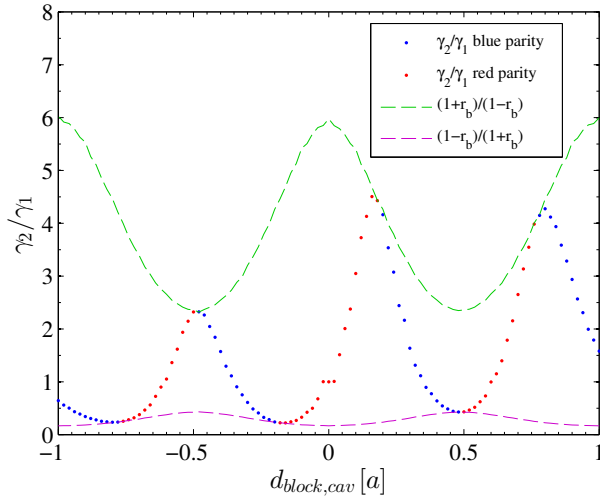


**Figure 4.13:** The decay rate ratio,  $\gamma_2/\gamma_1$ , plotted as function of the distance between the blocking element and the cavity. The green and purple broken line presents the theoretical upper and lower bound on the decay rate ratio. The color of the points indicates the parity of the transmission spectrum.

Now moving the blocking element back and forth in the waveguide results in many transmission spectra as the one in Figure 4.9 and they have all been fitted to equation (4.1.5), in order to extract the parameters  $t_B$ ,  $\omega_0$ ,  $\gamma_1$ ,  $\gamma_2$  and  $\gamma_v$ . The parity of each transmission spectrum determines the sign in equation (4.1.5), where + is for blue parity and - is for red parity. In Figures 4.11 and 4.12 two transmission spectra is seen for a block-cavity distance of  $-0.28a$  and  $0.60a$  respectively. More transmission spectra for  $r_{block} = 0.80 r/a$  are found in Appendix E.2.

In [13] a natural bound on the decay rate ratio  $\gamma_2/\gamma_1$  is derived. The upper and lower

bounds are  $(1 + r_B)/(1 - r_B)$  and  $(1 - r_B)/(1 + r_B)$  respectively. The decay rate ratio is plotted in Figure 4.13 as function of  $d_{block,cav}$ . It is noticed that the ratio fits nicely between the upper and lower bounds and furthermore it is noticed that the parity seem to change whenever the ratio hits the boundaries. This behaviour is a consequence of equation (4.1.4), since the real part becomes zero whenever the decay rate ratio equals either the upper or lower bound, indicating that the sign in equation (4.1.4) is changed. This is derived below for the upper bound, where  $\gamma_2/\gamma_1 = (1 + r_B)/(1 - r_B)$ :

$$\begin{aligned}
\Re[\exp(i(\theta_2 - \theta_1))] &= \cos(\theta_2 - \theta_1) = \\
&= \pm \frac{\sqrt{4\frac{\gamma_2}{\gamma_1} - (1 - r_B^2) \left(1 + \frac{\gamma_2}{\gamma_1}\right)^2}}{2r_B \sqrt{\frac{\gamma_2}{\gamma_1}}} \\
&= \pm \sqrt{\frac{4\frac{1+r_B}{1-r_B} - (1 + r_B)(1 - r_B) \left(1 + \frac{1+r_B}{1-r_B}\right)^2}{4r_B^2 \frac{1+r_B}{1-r_B}}} \\
&= \pm \sqrt{\frac{\frac{1}{r_B^2} - \frac{1}{4r_B^2} \left( (1 - r_B)^2 \left(1 + 2\frac{1+r_B}{1-r_B} + \left(\frac{1+r_B}{1-r_B}\right)^2\right) \right)}{\frac{1}{r_B^2} - \frac{1}{4r_B^2} \left( (1 - r_B)^2 + (1 + r_B)^2 + 2(1 + r_B)(1 - r_B) \right)}} = 0.
\end{aligned} \tag{4.2.1}$$

The derivation for the lower bound can be performed in a similar way. Thereby the coupled-mode theory mathematically predicts whenever the parity changes. The change in parity is likewise visualized in Figure 4.14 by plotting the real part of the phase difference in equation (4.1.4) as function of  $d_{block,cav}$ , where the parameters from the fit have been used for computing the phase difference. The parity indicated in the plot is found directly from the transmission spectra and as seen it changes whenever the phase difference crosses zero. Thereby the simulations support the prediction from coupled-mode theory.

As stated earlier the resonance frequency of the cavity is expected to depend on the relative position of the blocking element - at least when the blocking element is not too far away from the cavity. This is observed in Figure 4.15, where it is seen that the resonance frequency indeed depend on  $d_{block,cav}$ . Thereby the frequency range of interest is different for every transmission spectrum (see Figures 4.9, 4.11 and 4.12). In order to find the frequency range of interest the approximate resonance frequency is found by doing a transmission computation with larger frequency steps and then by reading off the approximate dip in the transmission spectrum the frequency range of interest is found. This is done for the blocking element positions  $0a$  to  $1.0a$  with step sizes of  $0.1a$ , so in total 11 times and then the frequency ranges for the blocking element positions in between could be estimated.

The exact same computations as presented above have been carried out for a smaller blocking element with radius  $r_{block} = 0.30r/a$  with the reasoning being that a smaller blocking element will alter the field in the waveguide less and thereby analysing the field

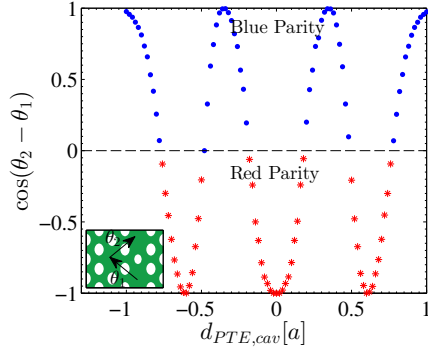


**Figure 4.14:** A plot of the real part of the computed phase difference in equation (4.1.4). The color indicates the parity.

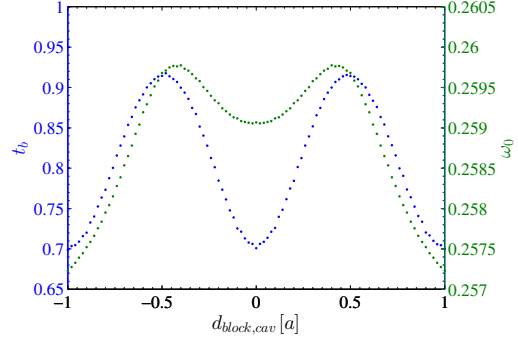


**Figure 4.15:** The direct transmission coefficient,  $t_B$ , and the cavity resonance frequency plotted as function of  $d_{block,cav}$ . As both parameters depend on the position of the blocking element.

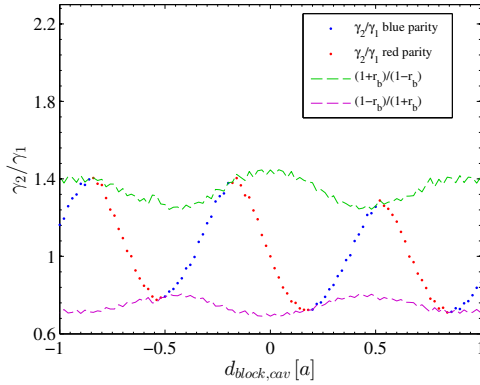


**Figure 4.16:** The decay rate ratio plotted as function of the distance between blocking element and cavity for  $r_{block} = 0.30r/a$ . As seen the parity changes whenever the ratio hits either the upper or lower boundary.

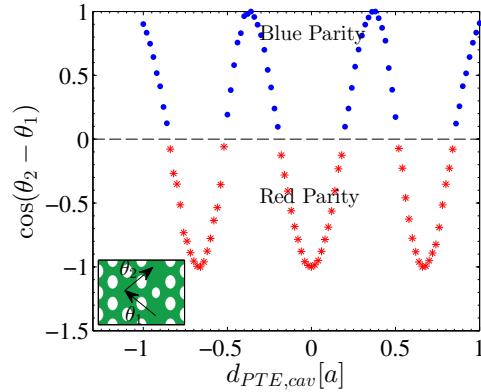


**Figure 4.17:** The phase difference plotted as function of the distance between blocking element and cavity for  $r_{block} = 0.30r/a$ . The parity changes when the sign of the phase difference changes.

distribution and parity might be simpler. The key results from these simulations are seen in Figures 4.16 and 4.17, where the decay rate ratio and the phase difference is plotted respectively. The plot for the resonance frequency and the direct transmission coefficient is found in Appendix E.

By comparing Figure 4.16 with its counterpart for  $r_{block} = 0.80r/a$  shown in Figure 4.13 it is noticed that the upper and lower boundaries are not as smooth as for the bigger blocking element. This is probably due to the staircase approximation used for constructing the PhCs. There have been used 81 grid points for each unit cell in the propagation direction and since this number has been kept constant through all the simulations this means that the staircase approximation uses less grid points for smaller

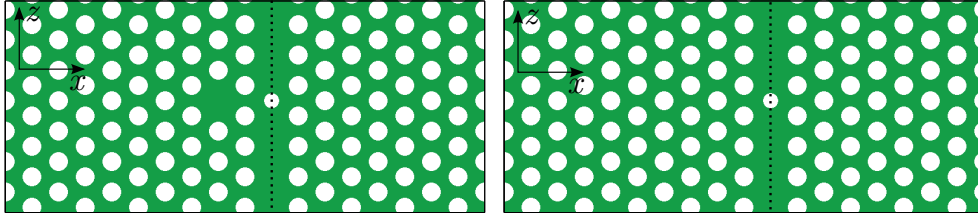


**Figure 4.18:** PhC Fano structure. The dotted line indicate the mid of the waveguide region, along which the field distribution is investigated.

**Figure 4.19:** Blocked waveguide. The dotted line indicate the mid of the waveguide region, along which the field distribution is investigated.

blocking elements, making the edge of the circle more rough. It should be stated that whether this is the source of the less smooth boundaries in Figure 4.16 have not been investigated - this could easily be done by increasing the number of grid points per unit cell and see how this affects the smoothness of the boundaries. The roughness could also be due to an increased uncertainty in the fitting parameters. As stated earlier the initial guesses on the parameters have a large effect on the outcome of the least squares method used by Matlab and it might be that these guesses need to be even better for smaller blocking element.

### 4.3 Field distribution and parity

As seen in the previous section, coupled-mode theory well describes and predicts the interference phenomena in PhC Fano structures. In this part the relation between field distribution and parity is investigated. For the first investigations the entire field was stored, but this took up 125 megabytes of space per field and this amount would quickly fill up my dropbox space and furthermore it was difficult to get any useful information out from the full field (full field computations are presented in Appendix E.1). Therefore a simpler approach is used where only the field along the mid of the waveguide is investigated as illustrated in Figure 4.18.

The idea of looking at the fields in the mid of the waveguide is to do qualitative observations of the field distribution along the waveguide and see whether there is a pattern, that can be related to the Fano parity. The first approach was to look at the field distribution at the resonance frequency in the full PhC Fano structure and compare this with the field distribution of the same system with no cavity - i.e. a blocked waveguide structure. The two structures are seen in Figures 4.18 and 4.19 respectively. These structures are illuminated with the resonance frequency of the Fano structure and for the mirror symmetric Fano structure ( $d_{block,cav} = 0.0a$ ) the resulting field distribution in the mid of the waveguide is seen in Figure 4.20 for  $r_{block} = 0.80r/a$ . As illustrated in Figure 4.2 the blocking element has been moved back and forth in the waveguide with steps of  $0.02a$  and for each new position a field distribution plot has been made. Some of these are found in Appendix E.5. Looking at all these field plots did not reveal any clear method for determining the parity from the field distribution along the mid of the waveguide.

Essentially the parity is determined by the phase difference between the complex coupling coefficients in and out of the cavity,  $d_1$  and  $d_2$ , given in equation (4.1.4). These

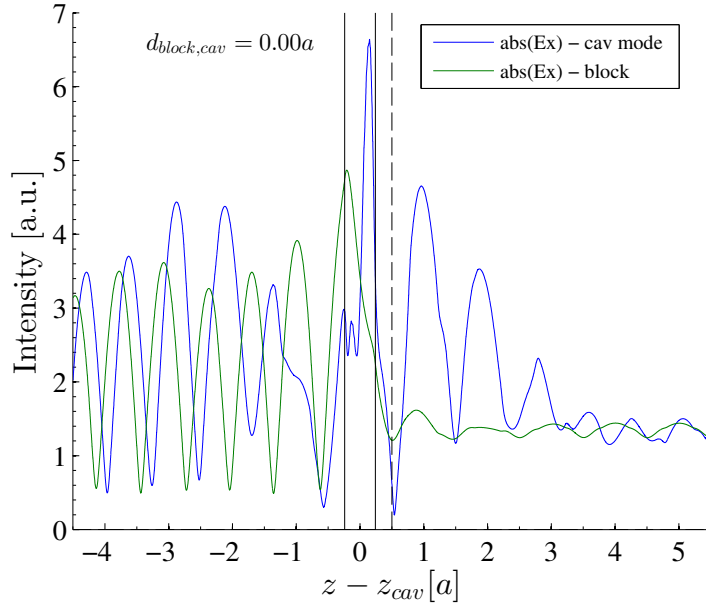


**Figure 4.20:** The absolute of  $E_x$  for both the Fano structure in Figure 4.18 and the blocked waveguide structure in Figure 4.19. The vertical black lines indicate the position of the blocking element and the vertical dashed line indicate the start of the periodic section after the blocking element.  $r_{block} = 0.80r/a$ . Both the structures are illuminated with the resonance frequency of the Fano structure.

coupling coefficients depend on the symmetry of the system and thereby on the distance between cavity and blocking element. For the systems investigated in this project, it is a bit difficult to separate the effects of the cavity and the blocking element, since the blocking element is part of the cavity. As presented in the previous section simulations with a smaller blocking element has been performed with the advantage being that a smaller blocking element has a smaller effect on the cavity mode. The blocking element is therefore reduced to  $r_{block} = 0.30r/a$ , and similar plots as the one presented in Figure 4.20 and the figures in Appendix E.5 has been made. But again these plots, did not give a clear correlation between field distribution and parity. Some of the plots are found in Appendix E.5.

As seen in Figures 4.14 and 4.17 the parity varies periodically and this motivated investigating the correlation between parity and the position of the blocking element in the waveguide field. In Figure 4.21 the  $E_x$  field distribution in the mid of a pure waveguide illuminated with the resonance frequency of the mirror symmetric Fano structure (see Figure 4.18) with  $r_{block} = 0.30r/a$ . The color in the plot indicate what parity the Fano structure has when the blocking element is put in that position in the waveguide. There seem to be a change in parity around the extrema of the real and imaginary part of the  $E_x$  field distribution. This finding is quite interesting, since this indicates that there might be a simple correlation between the field distribution in a pure waveguide, the position of the blocking element relative to the cavity and the parity of the Fano resonance. Taking a closer look at Figure 4.21 reveals, that the parity does not change at exactly the extrema but sometimes a bit before or after the extremum. This could be

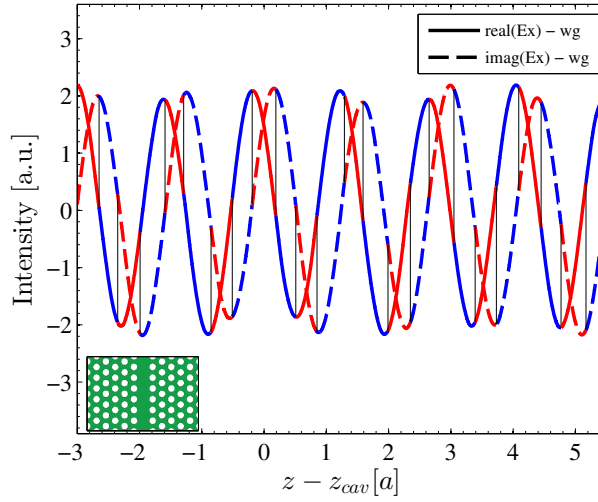


**Figure 4.21:** The real and imaginary part of the  $E_x$  field in the mid of the waveguide seen in the inset. The waveguide is illuminated with the resonance frequency of the mirror symmetric Fano structure seen in Figure 4.18, with  $r_{block} = 0.30r/a$ . The colors indicate the parity of the Fano structure when the blocking element is moved along the waveguide.

due to the dependence of the resonance frequency on the position of the blocking element - a different frequency of light in the waveguide will give a different distribution of the field components.

The result in Figure 4.21 is quite promising and this motivated another simulation, where the resonance frequency of the cavity was changed slightly by moving two of the holes surrounding the cavity a little as illustrated in Figure 4.22. Moving the blocking element with this new cavity resulted in new transmission spectra (some of which are found in Appendix E.3) and thereby the parity as function of the position of the blocking element.

Having determined the parity for different positions of the blocking element relative to the cavity, the pure waveguide mode is plotted in Figure 4.23 and coloured for illustrating the parity of the full PhC Fano structure at the different positions of the blocking element as in Figure 4.21. In contrast to the finding in Figure 4.21 the parity no longer seems to change at the extrema of the real and imaginary part of the  $E_x$ -field distribution. Thereby it can be concluded that only looking at the waveguide field distribution at one frequency for determining the parity is too simple.

To sum up the results presented in this chapter, it is concluded that the coupled-mode theory well describes the Fano resonances observed in the transmission spectra of different PhC cavity and waveguide configurations. Coupled-mode theory predicts the exact change in parity from the phase difference between the coupling coefficients in and out of the cavity as presented in Figures 4.14 and 4.17. It was found theoretically that the parity changes whenever  $\cos(\theta_2 - \theta_1) = 0$ , but relating this phase difference to the field distribution has not been fully achieved. There is therefore still work to be done and the next chapter will provide suggestions for future investigations.

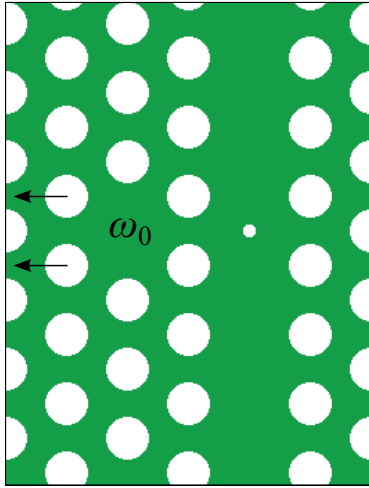


**Figure 4.22:** The resonance frequency of the cavity was changed by moving the two holes in the PhC  $0.1a$  in the direction of the arrows.

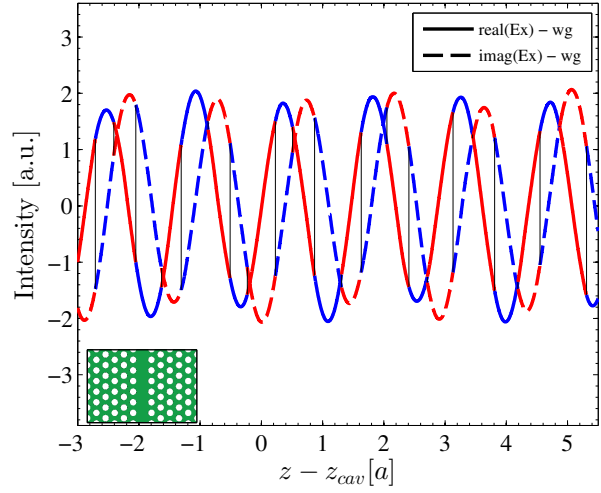


**Figure 4.23:** The real and imaginary part of the  $E_x$  field in the mid of the waveguide seen in the inset. The waveguide is illuminated with the resonance frequency of the mirror symmetric Fano structure seen in Figure 4.22, with  $r_{block} = 0.30 r/a$ . The colors indicate the parity of the Fano structure when the blocking element is moved along the waveguide.

---

## Discussion and Suggestions

This chapter will provide an overall discussion of the results presented in the previous chapter and give suggestions on the next investigations for finding an easier and faster way of determining the Fano parity of PhC cavity and waveguide structures.

### 5.1 Dependence of resonance frequency on position of blocking element

This project sought a correlation between how the field distributed in the waveguide at the resonance frequency of the cavity and the parity of the Fano resonance. As stated in the previous chapter, no clear correlation have been found, but it is still too soon to state that no correlation exists! The field distributions presented in Figures 4.21 and 4.23 are found by illuminating the waveguide with the resonance frequency of the mirror symmetric PhC Fano structure, but as stated earlier the resonance frequency depend on the position of the blocking element. This dependence is seen in Figures 4.15 and E.20 in section 4.2 and Appendix E.4. It would be interesting to investigate how the field distribution changes with frequency in order to see whether this can explain the different behaviours of Figures 4.21 and 4.23. It could be a coincident that the parity changes around the extrema of the pure waveguide mode in Figure 4.21, but it could also be a first step in finding a correlation between field distribution and parity.

Therefore a future investigation would be to determine how big an impact the dependence of the resonance frequency has on the field distribution in the pure waveguide.

Another approach could be to reduce the impact of the position of the blocking element on the resonance frequency of the cavity. This could be done by moving the cavity

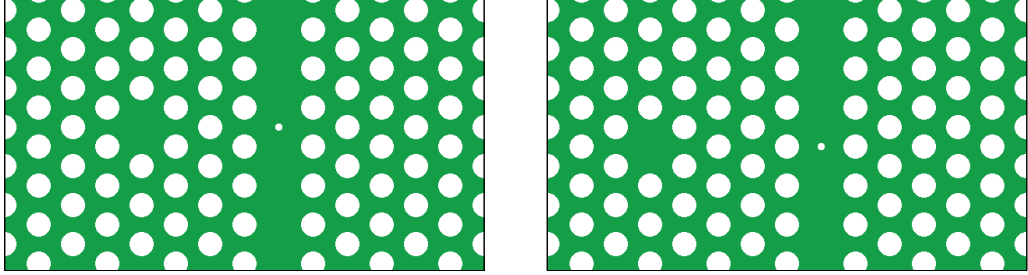


**Figure 5.1:** Increasing the cavity-waveguide distance should lower the dependence of the resonance frequency on the position of the blocking element.

further into the bulk of the PhC and thereby increasing the distance to the waveguide as illustrated in Figure 5.1. In [4] they have already investigated a similar system as the one depicted in Figure 5.1 to the left and in that paper a dependence of the resonance frequency on the size of the blocking element is reported but it is not investigated how much the resonance frequency changes when moving the blocking element (blocking element = PTE in [4]).

These investigations can be carried out with the already implemented code - all what's needed is time to do it.

## 5.2 Natural resonance frequency

There is no common widespread definition of what is meant by cavity modes even though the terms are widely used [22]. In [22] they argue that the best existing method for determining cavity mode volumes and resonance frequencies are by using quasinormal modes (QNMs) as used in [21]. QNMs have not been implemented in this project, due to lack of time and therefore an approximation of the cavity mode by illuminating the PhC Fano structures with their resonance frequency have been used in order to determine the mode profile of the cavity mode. As presented in the previous chapter no clear correlation between the field distribution of the cavity mode and the parity have been found, but it is discussable how good an approximation of the cavity mode it is to illuminate the Fano structures with their resonance frequencies.

The cavity mode for the mirror symmetric Fano structures seen in Figures 4.18, 4.22 and 5.1 should as well be mirror symmetric. This is not the case as seen in Figure 4.20 indicating that this approximation of the cavity mode is not completely valid. Although when illuminating the Fano structures at their resonance frequency almost all of the light will take the path through the cavity instead of the direct path transmitting through the blocking element, therefore the approximation is probably not too bad for the cavity mode on the output side of the blocking element.

All in all it would be a good idea to get the actual cavity mode profiles and do similar plots as presented in Figure 4.20 and in Figures E.21-E.28 in Appendix E.5 in order to look for patterns that can be related to the Fano parity. Therefore implementing QNMs would be another next step in this project.

The implementation will not be too difficult since the Fourier modal method with a Bloch mode expansion still can be used as presented in [23]. The difference being that

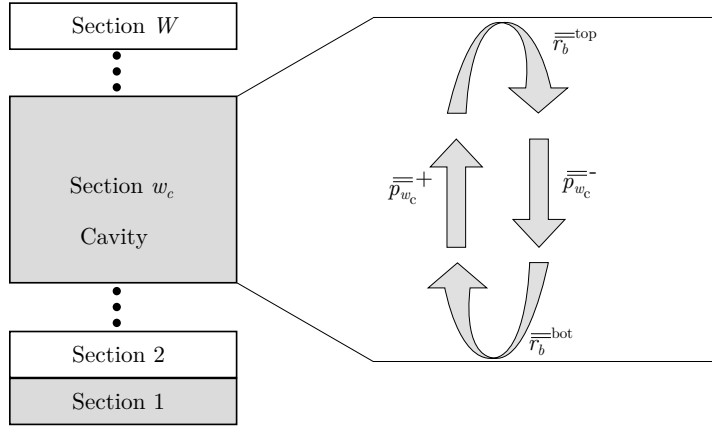


**Figure 5.2:** Illustration of the reflection and propagation matrices for the cavity section,  $w_c$ , of a structure consisting of  $W$  sections.

in addition the following eigenvalue problem for the cavity section needs to be solved [21, 23]:

$$\overline{\overline{M}}^{w_c}(\lambda_0)\overline{c}^{w_c} = \overline{c}^{w_c}, \quad (5.2.1)$$

where  $\overline{\overline{M}}^{w_c} = \overline{\overline{r}}_b^{\text{bot}} \overline{\overline{p}}_{w_c}^- \overline{\overline{r}}_b^{\text{top}} \overline{\overline{p}}_{w_c}^+$  and  $w_c$  refers to the cavity section.  $\overline{\overline{r}}_b^{\text{bot}}$  is the reflection matrix between the cavity section and all the sections below it and correspondingly  $\overline{\overline{r}}_b^{\text{top}}$  is the reflection matrix between the cavity section and all sections above it.  $\overline{\overline{p}}_{w_c}^\pm$  is the forward and backward propagation matrix inside the cavity section. Figure 5.2 illustrates the geometrical meaning of the matrices.

From equation 5.2.1 it is noted that the eigenvalue of  $\overline{\overline{M}}^{w_c}$  must be unity but this is not possible for real wavelengths,  $\lambda_0$ , since the elements of the reflection matrices,  $r$ , will be less than unity and absolute of the elements of the propagation matrices,  $|p_{w_c}^\pm|$ , will at maximum be unity. The leakage of the cavity can be taken into account by letting  $\lambda_0$  take complex values, since for complex wavelengths  $|p_{w_c}^\pm|$  can take values larger than unity, thereby making it possible for  $\overline{\overline{M}}^{w_c}$  to have an eigenvalue of unity [21, 23]. Thereby solving equation (5.2.1) will lead to a complex wavelength of the cavity mode. The complex part thus gives the leakage out of the cavity and the real part is the physical resonance wavelength.

### 5.3 Simplifying the problem by considering fewer Bloch modes

Basically the parity is determined by the phase difference of the complex couplings coefficients from the input port to the cavity and from the cavity to the output port. This phase difference completely determines the parity of the Fano resonance. An approach for getting a better understanding of these couplings coefficients could be to simplify the Bloch reflection and transmission matrices by considering only a few Bloch modes when constructing the reflection and transmission matrices between the periodic sections. So

instead of considering all  $N$  forward and backward propagating Bloch modes, then taking only 3 forward and 3 backward propagating modes for instance will result in  $3 \times 3$  transmission and reflection matrices - as can be seen from equations (3.1.92) and (3.1.93). The chosen modes should be the 3 forward and 3 backward propagating modes, whose absolute eigenvalue are closest to unity. The reasoning for doing this is that these few Bloch modes might give a good description of the full Bloch mode, since all the higher order modes are exponentially decaying.

By reducing the dimensionality of the transmission and reflection matrices all the higher order Bloch modes are filtered out, when looking at the field distributions as in Figure 4.20. This approach is quite straightforward to do with the already developed code, since all is needed is to pick out the wanted Bloch modes. The dimensions of the matrices should not cause any problems as will be shown here. The Bloch mode matrices,  $\overline{\overline{c_1^\pm}}$ ,  $\overline{\overline{c_2^\pm}}$ ,  $\overline{\overline{d_1^\pm}}$  and  $\overline{\overline{d_2^\pm}}$  will be  $N \times 3$  matrices. These are used in equations (3.1.92) and (3.1.93) for finding the reflection and transmission matrices between adjacent sections. In these equations the scalar product matrices,  $\overline{\langle \mathbf{e}_{2,1} | \mathbf{h}_{1,2} \rangle}$  are  $N \times N$  matrices and thereby the following product will result in  $N \times 3$  matrices as well:

$$\overline{\langle \mathbf{e}_2 | \mathbf{h}_1 \rangle}^T \left( \overline{\overline{c_2^+}} + \overline{\overline{d_2^+}} \right) = (N \times 3) \text{matrix.} \quad (5.3.1)$$

This product is then multiplied with  $\left( \overline{\overline{c_1^-}} + \overline{\overline{d_1^-}} \right)^{-1}$  and inverting a non-square matrix is possible by using pseudoinverse [24]. Matlab uses this automatically, when using the \-operator and thereby the product  $\left( \overline{\overline{c_1^-}} + \overline{\overline{d_1^-}} \right)^{-1} \overline{\langle \mathbf{e}_2 | \mathbf{h}_1 \rangle}^T \left( \overline{\overline{c_2^+}} + \overline{\overline{d_2^+}} \right)$  will give a  $3 \times 3$  matrix and the coupling between the cavity section and the in- and output port of the waveguide will be simpler to investigate.

---

## Conclusion and Outlook

This final chapter of the thesis will summarize and conclude on the work presented in the preceding chapters and provide an outlook for future work based on the suggestions given in Chapter 5.

### 6.1 Review of thesis

In this project optical simulation tools based on Fourier modal method and a Bloch modal formalism has been developed from scratch in Matlab and used for investigating PhC structures.

Chapter 2 started from Maxwell's equations and derived the 2D eigenvalue problems for TE and TM polarization in layers with uniformity in the propagation direction. Furthermore a brief crash course on the most basic optical properties of PhCs was given in this chapter and in the end of the chapter it was discussed what 2D computations of PhCs can be used for compared to 3D computations. As long as the simulations are within the fast light region 2D computations can be used for qualitative purposes.

Chapter 3 went through the implementation of the Fourier modal method, starting by solving the eigenvalue problems derived in Chapter 2 using a plane-wave expansion technique. Employing boundary conditions at the layer interfaces reflection and transmission matrices between adjacent layers was computed and then using a scattering matrix formalism, the complete transmission and reflection properties of the PhC structures was calculated. After this Bloch modes was introduced and the electromagnetic field was expanded on these. The Bloch modes was found by solving an eigenvalue problem for each periodic section, by using the scattering matrices computed from the eigenmodes. The

Bloch modes was classified as either forward or backward propagating and by employing boundary conditions at the periodic section interfaces, the transmission and reflection matrices for the Bloch modes between adjacent periodic sections was computed. The scattering matrix formalism was then used on these transmission and reflection matrices in order to get the complete transmission and reflection properties for the whole structure. How to visualize the fields in the periodic elements is described in details in Appendix B.9. The chapter then gave an overview of the implementation of the method and validated the method by comparing results produced with the developed code with similar results from the literature. Based on [14, 19] the chapter encompass a section with a discussion on why Fourier modal method is advantageous, when performing simulations on PhC structures. Especially the periodicity of PhCs are well exploited in the Fourier modal method with the Bloch modal expansion. The chapter finished with examples of observed numerical faults in the code, that origin from the scattering matrix algorithm given in equations (3.1.58)-(3.1.65) and concluded that the numerical instability only affects the results in a few cases, that are easily identified. Therefore the results are in general reliable.

Chapter 4 presented the obtained simulation results using the developed code. The first section introduced central results from the coupled-mode theory and gave the transmission function for general Fano structures, mirror-symmetric Fano structures and Lorentzian structures. The method for finding the resonance frequency of the Fano structures was outlined and it was assured that the resonance frequencies are within the fast light region of the band diagram, such that 2D computations are sufficient for qualitative purposes. The next section presented computed transmission spectra, which were fitted to the transmission functions derived from coupled-mode theory. The extracted parameters were then plotted and it was concluded that coupled-mode theory well describes the obtained simulation results. The parity changes in Figures 4.14 and 4.17, when  $\cos(\theta_2 - \theta_1) = 0$  as predicted by coupled-mode theory and since the phase difference completely determines the parity the next investigation of finding a correlation between field distribution and parity was motivated. This brings us to the last section of Chapter 4 that presented a plot of the field distribution of the cavity mode and block mode, but concluded that no correlation between these field distributions in the mid of the waveguide and the parity of the Fano resonances was found. It was found that the parity changes at the extrema of the real and imaginary parts of the  $E_x$  field distribution in the mid of a pure waveguide structure, but when the cavity of this Fano structure was changed a little, this behaviour was not reproduced. These results are seen in Figures 4.21 and 4.23. The chapter concluded that no correlation have been found (yet!) between field distribution and parity of Fano resonances.

Chapter 5 gave three suggestions for further investigations on determining a field-parity correlation. The first was to further investigate, whether the different results presented in Figures 4.21 and 4.23 can be explained by the dependence of the resonance frequency on the position of the blocking element. The next suggestion was to implement quasi-normal modes (QNMs) in order to visualize the cavity mode. In this project an approximation of the cavity mode has been realised by illuminating the PhC Fano structures at the resonance frequency. Therefore implementing QNMs might provide a better understanding on the correlation between field distribution and parity. The final suggestion was to simplify the transmission and reflection matrices by only considering a few Bloch modes. This could provide a better understanding on the coupling between the waveguide regions and the cavity region and thereby the phase differences that determines the parity

as presented in Chapter 4.

All this leads to the following overall conclusions on the work presented in this thesis:

1. Through theoretical considerations and 2D simulations it is concluded that the parity of PhC Fano structures are uniquely determined by the phase difference between the coupling coefficients between the cavity and the in- and output port of the waveguide.
2. There was not found a clear correlation between the field distribution in the mid of the waveguide and the parity of the Fano resonances, when the PhC waveguide and cavity structure was illuminated with their resonance frequency. Further investigations are needed and suggested for finding this correlation.

This brings us to the outlook of this thesis.

## 6.2 Outlook

In Chapter 5 three suggestions for future work were given and the order in which they should be carried out will be discussed here. The first suggestion (section 5.1) will take the least amount of time to carry out and will thereby quickly give an indication on what to do next. Therefore it is recommended that the next investigations should start with determining the impact of the resonance frequency on the field distribution in a pure waveguide. This will reveal whether the correlation between field extrema and change in parity presented in Figure 4.21 is a coincidence or a physical phenomena that is observed when the resonance frequency of the Fano structures have a minor effect on the pure waveguide field distribution.

Whether investigating the QNMs of the Fano structures or simplifying the transmission and reflection matrices are the best next step is hard to say. Considering fewer Bloch modes should be quite straightforward to implement, since the Fourier modal method is perfectly able to handle this. Therefore only minor changes in the code is needed for this investigation. However, QNMs will provide a visualization of the cavity modes and thereby might reveal a direct correlation between the distribution of the cavity mode and the block mode, and the resulting parity of the Fano structure. Implementing QNMs will probably take a bit more time but should not be too demanding. The experience made in this project though, is that writing the code is not what takes time - it is the debugging afterwards.

Simplifying the transmission and reflection matrices might make it possible for identifying the phase differences associated with coupling in and out of the waveguide region. As illustrated in Figure 6.1 the transmission and reflection matrices assures the continuity of the Bloch modes along the interface between the periodic sections. Considering fewer Bloch modes and their spatial distribution at the interface might make it possible to extract the phases that the field obtains when coupling in and out of the cavity region. How this should be realized is not fully developed or thought through but a better understanding on these phases from coupled-mode theory might be obtained from this approach. Thereby simplifying the transmission and reflection matrices is not the challenge here - instead the challenge is to try and extract the phase terms from these

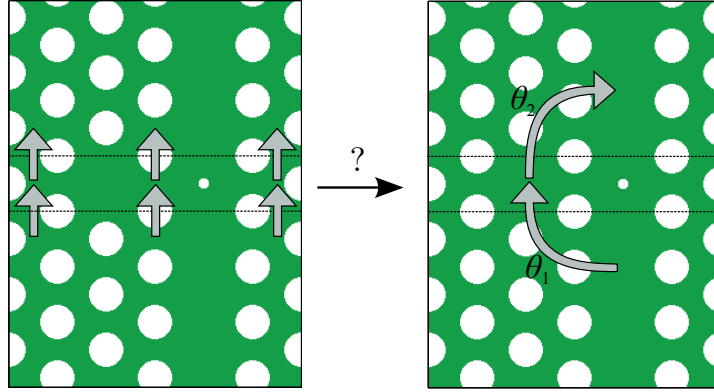


**Figure 6.1:** The transmission and reflection matrices matches the Bloch modes in each periodic section, such that they are continuous along the interface as indicated in the left figure. Considering fewer Bloch modes might give the opportunity to find the coupling between the Bloch mode in the waveguide region and the Bloch mode in the cavity region and the phase term related to this coupling.

matrices. Therefore implementing QNMs might be a better next step since this will probably give results before the other approach would.

The considerations on the next investigations are not hypothetical, since I have submitted for CLEO Europe 2015 in June and hopefully they will accept my submission (see Appendix F for the submission abstract). I start on my PhD in mid of March and will spend the first few months on (hopefully) finishing the research started in this thesis on a parity-field distribution correlation. This limits the amount of time for further investigations and therefore time is an important consideration when choosing what to do next.

The above gave the short term outlook. Expanding the outlook will motivate why researching these Fano structures are important as done in the introduction. You could ask the question, why bother being able to predict the parity of a given Fano structure when the parity is uniquely determined from computing the transmission spectrum? Researching in this field are still on a fundamental level, so the purpose of further investigations are to increase the understanding on what determines the parity. Increasing the understanding might provide new ideas for engineering the Fano structures, such that the parity is a choice rather than a consequence. As stated in the introduction Fano resonances can be used for optical switching [3] and in PhC lasers [1]. Thereby the devices using Fano resonances are already in the pipeline and therefore increasing the understanding on the parity of Fano structures are still an important research field.

---

## Appendix for theoretical concepts

### A.1 Maxwell's equations ins frequency domain

The Fourier transform of a field  $\mathbf{F}$  used in the following derivation is [15, 16]:

$$\mathbf{F}(\mathbf{r}, t) = \frac{1}{2\pi} \int_{-\infty}^{\infty} \mathbf{F}(\mathbf{r}, \omega) \exp(i\omega t) d\omega; \quad \mathbf{F}(\mathbf{r}, \omega) = \int_{-\infty}^{\infty} \mathbf{F}(\mathbf{r}, t) \exp(-i\omega t) dt, \quad (\text{A.1.1})$$

where  $\mathbf{F}$  can be replaced by either  $\mathbf{E}$  or  $\mathbf{H}$ . The Fourier transforms of the electric and magnetic susceptibilities,  $\chi_{e,m}$  are:

$$\chi_{e,m}(\mathbf{r}, \omega) = \int_{-\infty}^{\infty} \chi_{e,m}(\mathbf{r}, t) \exp(-i\omega t) dt. \quad (\text{A.1.2})$$

From equations (A.1.1) and (A.1.2) and using the convolution theorem of Fourier theory the electric displacement field,  $\mathbf{D}$ , in the frequency-domain is given as [16]:

$$\mathbf{D}(\mathbf{r}, \omega) = \varepsilon_0 \varepsilon(\mathbf{r}, \omega) \mathbf{E}(\mathbf{r}, \omega). \quad (\text{A.1.3})$$

The current density in equation (2.1.2) can be split into two terms, a source term,  $\mathbf{J}_s$ , and an induced current term,  $\mathbf{J}_c$ . The induced current can be described as a linear response expression in the time domain [16]:

$$\mathbf{J}_c(\mathbf{r}, t) = \int_0^{\infty} \sigma(\mathbf{r}, \tau) \mathbf{E}(\mathbf{r}, t - \tau) d\tau. \quad (\text{A.1.4})$$

This is actually Ohm's law, where  $\sigma$  is the conductivity of the material. By Fourier transforming this expression the induced current in the frequency domain is obtained:

$$\mathbf{J}_c(\mathbf{r}, \omega) = \sigma(\mathbf{r}, \omega) \mathbf{E}(\mathbf{r}, \omega). \quad (\text{A.1.5})$$

Fourier transforming Maxwell's Equation (2.1.2) and using equation (A.1.5) this equation in the frequency domain becomes:

$$\nabla \times \mathbf{H}(\mathbf{r}, \omega) = i\omega\epsilon_0 \left( \mathbf{D}(\mathbf{r}, \omega) - i \frac{\sigma(\mathbf{r}, \omega)}{\omega\epsilon_0} \mathbf{E}(\mathbf{r}, \omega) \right) + \mathbf{J}_s(\mathbf{r}) \quad (\text{A.1.6})$$

$$= i\omega\epsilon_0 \left( \epsilon(\mathbf{r}, \omega) - i \frac{\sigma(\mathbf{r}, \omega)}{\omega\epsilon_0} \right) \mathbf{E}(\mathbf{r}, \omega) + \mathbf{J}_s(\mathbf{r}), \quad (\text{A.1.7})$$

where the term in the parenthesis is referred to as the effective dielectric constant,  $\epsilon_{eff}$ . Note also that the current source only has a spatial dependence, since the time (and thereby frequency) dependence is entirely in the induced current. Fourier transforming the constitutive equation (2.1.8) gives the  $\mathbf{B}$ - $\mathbf{H}$  relation in the frequency domain:

$$\mathbf{B}(\mathbf{r}, \omega) = \mu_0\mu(\mathbf{r}, \omega)\mathbf{H}(\mathbf{r}, \omega). \quad (\text{A.1.8})$$

Now Maxwell's equations (2.1.1) and (2.1.2) can be derived in the frequency domain by inserting equation (A.1.1) for  $\mathbf{F} = \mathbf{E}$  and  $\mathbf{F} = \mathbf{H}$  and using the constitutive material equations (A.1.3) and (A.1.8). This leads to [15, 16]:

$$\nabla \times \mathbf{E}(\mathbf{r}, \omega) = -i\omega\mathbf{B}(\mathbf{r}, \omega) = -i\omega\mu_0\mu(\mathbf{r}, \omega)\mathbf{H}(\mathbf{r}, \omega), \quad (\text{A.1.9})$$

$$\nabla \times \mathbf{H}(\mathbf{r}, \omega) = i\omega\mathbf{D}(\mathbf{r}, \omega) + \mathbf{J}_s(\mathbf{r}) = i\omega\epsilon_0\epsilon(\mathbf{r}, \omega)\mathbf{E}(\mathbf{r}, \omega) + \mathbf{J}_s(\mathbf{r}). \quad (\text{A.1.10})$$

Thereby Maxwell's equations in the frequency domain has been derived. Note that  $\epsilon$  is the effective dielectric constant.

## A.2 Derivation of wave equations

The starting point for deriving the wave equations (2.2.6) and (2.2.7) are equations (2.1.10) and (2.1.11) which are restated here for convenience:

$$\nabla \times \mathbf{E}(\mathbf{r}, \omega) = -i\omega\mathbf{B}(\mathbf{r}, \omega) = -i\omega\mu_0\mu(\mathbf{r}, \omega)\mathbf{H}(\mathbf{r}, \omega), \quad (\text{A.2.1})$$

$$\nabla \times \mathbf{H}(\mathbf{r}, \omega) = i\omega\mathbf{D}(\mathbf{r}, \omega) + \mathbf{J}_s(\mathbf{r}) = i\omega\epsilon_0\epsilon(\mathbf{r}, \omega)\mathbf{E}(\mathbf{r}, \omega) + \mathbf{J}_s(\mathbf{r}). \quad (\text{A.2.2})$$

For now  $\mathbf{J}_s = 0$  and  $\mu = 1$ . Taking the curl on both sides of equations (A.2.1) and (A.2.2) gives:

$$\nabla \times \nabla \times \mathbf{E}(\mathbf{r}, \omega) = -i\omega\mu_0 \nabla \times \mathbf{H}(\mathbf{r}, \omega), \quad (\text{A.2.3})$$

$$\nabla \times \nabla \times \mathbf{H}(\mathbf{r}, \omega) = i\omega\epsilon_0 \nabla \times (\epsilon(\mathbf{r}, \omega)\mathbf{E}(\mathbf{r}, \omega)). \quad (\text{A.2.4})$$

Then using equation (A.2.2) in equation (A.2.3) and the vector relation  $\nabla \times (\varepsilon \mathbf{E}) = \varepsilon \nabla \times \mathbf{E} + \nabla \varepsilon \times \mathbf{E}$  will lead to:

$$\nabla \times \nabla \times \mathbf{E}(\mathbf{r}, \omega) = \left( \frac{\omega}{c_0} \right)^2 \varepsilon(\mathbf{r}, \omega) \mathbf{E}(\mathbf{r}, \omega) = k_0^2 \varepsilon(\mathbf{r}, \omega) \mathbf{E}(\mathbf{r}, \omega), \quad (\text{A.2.5})$$

$$\nabla \times \nabla \times \mathbf{H}(\mathbf{r}, \omega) = i\omega \varepsilon_0 (\varepsilon \nabla \times \mathbf{E}(\mathbf{r}, \omega) + \nabla \varepsilon \times \mathbf{E}(\mathbf{r}, \omega)), \quad (\text{A.2.6})$$

where  $c_0 = (\varepsilon_0 \mu_0)^{-1/2}$  is the speed of light in vacuum. The vector identity  $\nabla \times \nabla \times \mathbf{F} = -\nabla^2 \mathbf{F} + \nabla (\nabla \cdot \mathbf{F})$  is now used giving:

$$-\nabla^2 \mathbf{E}(\mathbf{r}, \omega) + \nabla (\nabla \cdot \mathbf{E}(\mathbf{r}, \omega)) = k_0^2 \varepsilon(\mathbf{r}, \omega) \mathbf{E}(\mathbf{r}, \omega), \quad (\text{A.2.7})$$

$$-\nabla^2 \mathbf{H}(\mathbf{r}, \omega) + \nabla (\nabla \cdot \mathbf{H}(\mathbf{r}, \omega)) = i\omega \varepsilon_0 (\varepsilon(\mathbf{r}, \omega) \nabla \times \mathbf{E}(\mathbf{r}, \omega) + \nabla \varepsilon(\mathbf{r}, \omega) \times \mathbf{E}(\mathbf{r}, \omega)). \quad (\text{A.2.8})$$

Maxwells equation (2.1.3) states that  $\nabla \cdot (\varepsilon(\mathbf{r}, \omega) \mathbf{E}(\mathbf{r}, \omega)) = 0$  and this statement leads to:

$$\begin{aligned} \nabla \cdot (\varepsilon(\mathbf{r}, \omega) \mathbf{E}(\mathbf{r}, \omega)) &= 0 \quad \Rightarrow \\ \mathbf{E}(\mathbf{r}, \omega) \nabla \varepsilon(\mathbf{r}, \omega) + \varepsilon(\mathbf{r}, \omega) \nabla \cdot \mathbf{E}(\mathbf{r}, \omega) &= 0 \quad \Rightarrow \\ \nabla \cdot \mathbf{E}(\mathbf{r}, \omega) &= -\mathbf{E}(\mathbf{r}, \omega) \frac{1}{\varepsilon(\mathbf{r}, \omega)} \nabla \varepsilon(\mathbf{r}, \omega) = -\mathbf{E}(\mathbf{r}, \omega) \nabla \ln(\varepsilon(\mathbf{r}, \omega)). \end{aligned} \quad (\text{A.2.9})$$

Using this in equation (A.2.7) the wave equation (2.2.6) comes out:

$$\nabla^2 \mathbf{E}(\mathbf{r}, \omega) + \nabla (\mathbf{E}(\mathbf{r}, \omega) \cdot \nabla \ln \varepsilon(\mathbf{r}, \omega)) + \varepsilon(\mathbf{r}, \omega) k_0^2 \mathbf{E}(\mathbf{r}, \omega) = 0 \quad (\text{A.2.10})$$

Now turning back to equation (A.2.8). Using that  $\mu(\mathbf{r}, \omega) = 1$  for non-magnetic materials and using equations (A.2.1) and (A.2.2) to get rid of the electric fields, the equation now looks like:

$$\begin{aligned} -\nabla^2 \mathbf{H}(\mathbf{r}, \omega) &= i\omega \varepsilon_0 \left[ \varepsilon(\mathbf{r}, \omega) (-i\omega \mu_0 \mathbf{H}(\mathbf{r}, \omega)) + \nabla \varepsilon(\mathbf{r}, \omega) \times \frac{1}{i\omega \varepsilon_0 \varepsilon(\mathbf{r}, \omega)} \nabla \times \mathbf{H}(\mathbf{r}, \omega) \right] \Rightarrow \\ -\nabla^2 \mathbf{H}(\mathbf{r}, \omega) &= \omega^2 \varepsilon_0 \varepsilon(\mathbf{r}, \omega) \mu_0 \mathbf{H}(\mathbf{r}, \omega) + \nabla \varepsilon(\mathbf{r}, \omega) \times \frac{1}{\varepsilon(\mathbf{r}, \omega)} \nabla \times \mathbf{H}(\mathbf{r}, \omega) \quad \Rightarrow \\ -\nabla^2 \mathbf{H}(\mathbf{r}, \omega) &= \omega^2 \varepsilon_0 \varepsilon(\mathbf{r}, \omega) \mu_0 \mathbf{H}(\mathbf{r}, \omega) + \frac{1}{\varepsilon(\mathbf{r}, \omega)} \nabla \varepsilon(\mathbf{r}, \omega) \times \nabla \times \mathbf{H}(\mathbf{r}, \omega) \quad \Rightarrow \\ \nabla^2 \mathbf{H}(\mathbf{r}, \omega) &+ k_0^2 \varepsilon(\mathbf{r}, \omega) \mathbf{H}(\mathbf{r}, \omega) + \nabla \ln(\varepsilon(\mathbf{r}, \omega)) \times \nabla \times \mathbf{H}(\mathbf{r}, \omega) = 0. \end{aligned} \quad (\text{A.2.11})$$

In that way the wave equation (2.2.7) for the magnetic field has been derived.

### A.3 Derivation of field components

The transverse part of the electric field can be found solving equation (2.3.6). Then using Maxwell's equation (2.1.3), the constitutive relation (2.1.7) and that there is no free charges,  $\rho = 0$ , the  $e_z$  component is found:

$$\begin{aligned} \nabla \cdot \mathbf{D}(\mathbf{r}, t) &= \nabla \cdot (\varepsilon_0 \varepsilon(\mathbf{r}_\perp) \mathbf{E}(\mathbf{r}, t)) = 0 & \Rightarrow \\ \nabla \cdot (\varepsilon(\mathbf{r}_\perp) \mathbf{e}(\mathbf{r}_\perp) \exp(i\beta z)) &= 0 & \Rightarrow \\ \varepsilon(\mathbf{r}_\perp) \partial_z (e_z \exp(i\beta z)) + \nabla_\perp \cdot (\varepsilon(\mathbf{r}_\perp) \mathbf{e}_\perp(\mathbf{r}_\perp) \exp(i\beta z)) &= 0 & \Rightarrow \\ e_z &= \frac{\nabla_\perp \cdot (\varepsilon(\mathbf{r}_\perp) \mathbf{e}_\perp(\mathbf{r}_\perp))}{-i\beta \varepsilon(\mathbf{r}_\perp)} = \frac{\nabla_\perp \cdot (\varepsilon \mathbf{e}_\perp)}{-i\beta \varepsilon}. \end{aligned} \quad (\text{A.3.1})$$

Thereby all three electric field components are known. The magnetic field components are found using equation (2.1.10), with  $\mu = 1$ :

$$\nabla \times \mathbf{E}(\mathbf{r}, \omega) = -i\omega \mathbf{B}(\mathbf{r}, \omega) = -i\omega \mu_0 \mathbf{H}(\mathbf{r}, \omega). \quad (\text{A.3.2})$$

This equation relates the transverse part of  $\mathbf{E}$  with the  $z$ -part of  $\mathbf{H}$  and vice versa. The  $z$ -part is straightforward to determine:

$$\hat{\mathbf{z}} \cdot \nabla \times \mathbf{E}_\perp = -i\omega \mu_0 H_z \quad \Rightarrow \quad (\text{A.3.3})$$

$$h_z = \frac{\hat{\mathbf{z}} \cdot \nabla \times \mathbf{e}_\perp}{i\mu_0 \omega}. \quad (\text{A.3.4})$$

As for the transverse part it demands a bit more vector calculus. Again starting from equation A.3.2 and do the cross product leads to:

$$\begin{bmatrix} \partial_y E_z - \partial_z E_y \\ \partial_z E_x - \partial_x E_z \\ 0 \end{bmatrix} = -i\omega \mu_0 \begin{bmatrix} H_x \\ H_y \\ 0 \end{bmatrix}, \quad (\text{A.3.5})$$

where the  $z$ -part has been left out for convenience. The vector to the left can be written in a shorter form:

$$\begin{bmatrix} \partial_y E_z - \partial_z E_y \\ \partial_z E_x - \partial_x E_z \\ 0 \end{bmatrix} = \hat{\mathbf{z}} \times \begin{bmatrix} \partial_z E_x - \partial_x E_z \\ \partial_z E_y - \partial_y E_z \\ 0 \end{bmatrix} = \hat{\mathbf{z}} \times (\partial_z \mathbf{E}_\perp - \nabla_\perp E_z). \quad (\text{A.3.6})$$

Using the two above equations and equation (A.3.1) this will lead to:

$$\hat{\mathbf{z}} \times (\partial_z (\mathbf{e}_\perp \exp(i\beta z)) - \nabla_\perp e_z \exp(i\beta z)) = -i\omega \mu_0 \mathbf{h}_\perp \exp(i\beta z) \quad \Rightarrow \quad (\text{A.3.7})$$

$$\mathbf{h}_\perp = \frac{1}{\mu_0 \omega} \hat{\mathbf{z}} \times \left( \beta \mathbf{e}_\perp - \nabla_\perp \left[ \frac{\nabla_\perp \cdot (\varepsilon \mathbf{e}_\perp)}{-i\beta \varepsilon} \right] \right). \quad (\text{A.3.8})$$

Thereby all the field components have been determined only from knowing the transverse part of the electric field.

If only the transverse part of the magnetic field is known, then using a similar approach as above the other four field components can be determined. The  $h_z$  component is found using Maxwell's equation (2.1.4) with the constitutive equation (2.1.8) and setting  $\mu = 1$ :

$$\begin{aligned}\nabla \cdot \mathbf{B}(\mathbf{r}, t) &= \nabla \cdot (\mu_0 \mathbf{H}(\mathbf{r}, t)) = 0 && \Rightarrow \\ \nabla \cdot (\mathbf{h}(\mathbf{r}_\perp) \exp(i\beta z)) &= 0 && \Rightarrow \\ \partial_z (h_z \exp(i\beta z)) + \nabla_\perp \cdot (\mathbf{h}_\perp(\mathbf{r}_\perp) \exp(i\beta z)) &= 0 && \Rightarrow \\ h_z &= \frac{i}{\beta} \nabla_\perp \cdot \mathbf{h}_\perp(\mathbf{r}_\perp) = \frac{i}{\beta} \nabla_\perp \cdot \mathbf{h}_\perp.\end{aligned}\tag{A.3.9}$$

Now all the magnetic field components are known, all the electric field components can be determined using Maxwell's equation (2.1.11). The approach is very similar for finding the magnetic field components when the electric field is known, so the derivation will not be given. The electric field components can be derived to be:

$$e_z = \frac{i}{\omega \varepsilon_0 \varepsilon \beta} \hat{\mathbf{z}} \cdot \nabla \times \mathbf{h}_\perp,\tag{A.3.10}$$

$$\mathbf{e}_\perp = \frac{-1}{\omega \varepsilon_0 \varepsilon} \hat{\mathbf{z}} \times \left( \beta \mathbf{h}_\perp - \nabla_\perp \left[ \frac{\nabla_\perp \cdot (\varepsilon \mathbf{h}_\perp)}{\beta} \right] \right)\tag{A.3.11}$$

## A.4 Decoupling of eigenvalue problems

For the electric field the eigenvalue problem is given in equation (2.3.6). Considering a slab waveguide the dielectric function only has an  $x$ -dependence. This means that both the electric and magnetic field only varies in  $x$ , meaning  $\partial_y \mathbf{e} = 0$  and  $\partial_y \mathbf{h} = 0$ . This will now be used in order to decouple equation (2.3.6):

$$\nabla_\perp^2 \mathbf{e}_\perp + \nabla_\perp (\mathbf{e}_\perp \cdot \nabla \ln \varepsilon(\mathbf{r}_\perp)) + \varepsilon(\mathbf{r}_\perp) k_0^2 \mathbf{e}_\perp = \beta^2 \mathbf{e}_\perp \quad \Rightarrow \tag{A.4.1}$$

$$\begin{cases} \left[ \begin{array}{l} \partial_x^2 e_x + \partial_y^2 e_x + \partial_x (e_x \partial_x \ln \varepsilon(x)) + \varepsilon(x) k_0^2 e_x \\ \partial_x^2 e_y + \partial_y^2 e_y + \partial_y (e_y \partial_y \ln \varepsilon(x)) + \varepsilon(x) k_0^2 e_y \end{array} \right] = \beta^2 \begin{bmatrix} e_x \\ e_y \end{bmatrix} \\ \left\{ \begin{array}{l} \partial_x^2 e_x + \partial_x (e_x \partial_x \ln \varepsilon(x)) + \varepsilon(x) k_0^2 e_x = \beta^2 e_x \\ \partial_x^2 e_y + \varepsilon(x) k_0^2 e_y = \beta^2 e_y \end{array} \right. \end{cases} \quad \Rightarrow \tag{A.4.2}$$

And in the same way the eigenvalue problem in equation (2.3.14) is decoupled into two equations. The decoupling is not as trivial as before due to the two cross products in the eigenvalue problem:

$$\nabla^2 \mathbf{h}_\perp + k_0^2 \varepsilon(\mathbf{r}_\perp) \mathbf{h}_\perp + \nabla \ln(\varepsilon(\mathbf{r}_\perp)) \times \nabla \times \mathbf{h}_\perp = \beta^2 \mathbf{h}_\perp.\tag{A.4.3}$$

Therefore the cross products are firstly evaluated:

$$\begin{aligned}
\nabla \ln(\varepsilon(\mathbf{r}_\perp)) \times \nabla \times \mathbf{h}_\perp &= \begin{bmatrix} \partial_x \ln \varepsilon(x) \\ \partial_y \ln \varepsilon(x) \\ \partial_z \ln \varepsilon(x) \end{bmatrix} \times \begin{bmatrix} \partial_x \\ \partial_y \\ \partial_z \end{bmatrix} \times \begin{bmatrix} h_x \\ h_y \\ 0 \end{bmatrix} \\
&= \begin{bmatrix} \partial_x \ln \varepsilon(x) \\ \partial_y \ln \varepsilon(x) \\ \partial_z \ln \varepsilon(x) \end{bmatrix} \times \begin{bmatrix} -\partial_z h_y \\ \partial_z h_x \\ \partial_x h_y - \partial_y h_x \end{bmatrix} \\
&= \begin{bmatrix} \partial_x \ln \varepsilon(x) \\ 0 \\ 0 \end{bmatrix} \times \begin{bmatrix} 0 \\ 0 \\ \partial_x h_y \end{bmatrix} = \begin{bmatrix} 0 \\ -\partial_x \ln \varepsilon(x) \partial_x h_y \\ 0 \end{bmatrix}. \quad (\text{A.4.4})
\end{aligned}$$

Now it is straightforward decoupling the eigenvalue problem:

$$\begin{aligned}
\nabla^2 \mathbf{h}_\perp + k_0^2 \varepsilon(\mathbf{r}_\perp) \mathbf{h}_\perp + \nabla \ln(\varepsilon(\mathbf{r}_\perp)) \times \nabla \times \mathbf{h}_\perp &= \beta^2 \mathbf{h}_\perp \quad \Rightarrow \\
\begin{cases} \partial_x^2 h_x + k_0^2 \varepsilon(x) h_x = \beta^2 h_x \\ \partial_x^2 h_y + k_0^2 h_y \varepsilon(x) - \partial_x \ln \varepsilon(x) \partial_x h_y = \beta^2 h_y \end{cases} & \quad (\text{A.4.5})
\end{aligned}$$

In that way the eigenvalue problems have been decoupled into two equations each.

## Appendix for computational method

### B.1 Li's Factorization Rules

A plane wave expansion is used when solving the eigenvalue problems as shown in section 3.1. Such two periodic functions and their product will be considered here:

$$f(x) = \sum_{m=-\infty}^{m=\infty} f_m \exp(imKx), \quad (\text{B.1.1})$$

$$g(x) = \sum_{n=-\infty}^{n=\infty} g_n \exp(inKx), \quad (\text{B.1.2})$$

$$h(x) = f(x)g(x) = \sum_{m=-\infty}^{m=\infty} h_m \exp(imKx) \Rightarrow \quad (\text{B.1.3})$$

$$\begin{aligned} h(x) &= \sum_{m=-\infty}^{m=\infty} f_m \exp(imKx) \sum_{n=-\infty}^{n=\infty} g_n \exp(inKx) \\ &= \sum_{m=-\infty}^{m=\infty} \sum_{n=-\infty}^{n=\infty} f_{m-n} g_n \exp(imKx), \end{aligned} \quad (\text{B.1.4})$$

where  $K = 2\pi/L_x$ . From this it is seen that:

$$h_m = \sum_{n=-\infty}^{n=\infty} f_{m-n} g_n. \quad (\text{B.1.5})$$

In order to vectorize equation (B.1.5) a truncation of the sum is needed. This is chosen to be from  $-M$  to  $M$ , such that the function  $f$  is given by a vector  $\bar{f} = [f_{-M}, \dots, f_M]$  of length  $N = 2M + 1$ . Now the expansion vector,  $\bar{h}$ , for  $h$  can be computed as: [16]

$$\bar{h} = \overline{\overline{F}}\bar{g}, \quad (\text{B.1.6})$$

where  $\overline{\overline{F}}$  is the  $N \times N$  Toeplitz matrix with the coefficients of the Fourier series of  $f$  as the elements:

$$\overline{\overline{F}} = \begin{bmatrix} f_0 & f_{-1} & f_{-2} & \dots & f_{-N+1} \\ f_1 & f_0 & f_{-1} & \dots & f_{-N+2} \\ f_2 & f_1 & f_0 & \dots & f_{-N+3} \\ \dots & \dots & \dots & \dots & \dots \end{bmatrix}. \quad (\text{B.1.7})$$

The matrix product in equation (B.1.6) is referred to as the *direct rule* for the product  $h(x) = f(x)g(x)$ . But there exist another way to calculate this product. First consider the function  $f^\dagger(x) = 1/f(x)$  given by the series expansion: [16]

$$f^\dagger(x) = \sum_{m=-\infty}^{m=\infty} f_m^\dagger \exp(imKx) \quad (\text{B.1.8})$$

and the corresponding Toeplitz  $\overline{\overline{F^\dagger}}$ . Since  $h = (f^\dagger)^{-1}g$ , the Fourier expansion coefficients of  $h$  can likewise be computed by:

$$\bar{h} = \left(\overline{\overline{F^\dagger}}\right)\bar{g}. \quad (\text{B.1.9})$$

The matrix product in equation (B.1.9) is referred to as the *inverse rule*.

Equations (B.1.6) and (B.1.9) give two ways of computing the same product. Which one to choose depends on which product converges fastest for  $N \rightarrow \infty$ . The rules for choosing the right product are known as *Li's factorization rules* [16]. The rules are based on the discontinuities of the function  $f(x)$  and  $g(x)$ .

In Figure B.1 there are shown two types of discontinuities in  $f(x)$  and  $g(x)$  - one where they are not and one where they are removable. *Li's factorization rules* are then given as the following:

1. If the discontinuities are of type 1, then the fastest convergence is obtained by choosing the product in equation (B.1.6) - the direct rule.
2. If the discontinuities are of type 2, then the fastest convergence is obtained by choosing the product in equation (B.1.9) - the inverse rule.

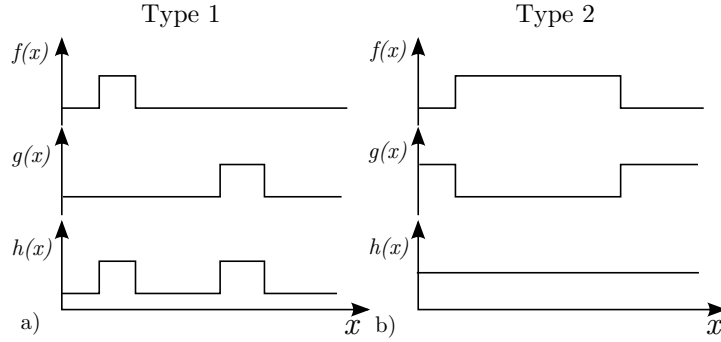


**Figure B.1:** a) The discontinuities in  $f(x)$  and  $g(x)$  are not complementary and therefore  $h(x) = f(x)g(x)$  is also discontinuous. b) The discontinuities in  $f(x)$  and  $g(x)$  are complementary and thereby the discontinuities in  $h(x) = f(x)g(x)$  are removable.

## B.2 Evaluation of $\varepsilon_j$ and $a_j$ elements

The integrals in equations (3.1.9) and (3.1.10) is evaluated analytically for the PhC structures investigated in this project, since  $\varepsilon(x)$  is a piecewise constant function as illustrated in Figure B.2. For the dielectric function illustrated in Figure B.2 the integrals are evaluated as:

$$\varepsilon_j = \frac{1}{L_x} \int_0^{L_x} \varepsilon(x) \exp(-ijKx) dx \quad \Rightarrow \quad (\text{B.2.1})$$

$$\begin{aligned} \varepsilon_j = \frac{1}{L_x} & [\varepsilon_1 (\exp(-ijKx_1) - 1) + \varepsilon_2 (\exp(-ijKx_2) - \exp(-ijKx_1)) \\ & + \varepsilon_1 (\exp(-ijKx_3) - \exp(-ijKx_2)) + \varepsilon_2 (\exp(-ijKx_4) - \exp(-ijKx_3)) \\ & + \varepsilon_1 (\exp(-ijKL_x) - \exp(-ijKx_4))] \end{aligned} \quad (\text{B.2.2})$$

$$a_j = \frac{1}{L_x} \int_0^{L_x} \frac{1}{\varepsilon(x)} \exp(-ijKx) dx \quad \Rightarrow \quad (\text{B.2.3})$$

$$\begin{aligned} a_j = \frac{1}{L_x} & \left[ \frac{1}{\varepsilon_1} (\exp(-ijKx_1) - 1) + \frac{1}{\varepsilon_2} (\exp(-ijKx_2) - \exp(-ijKx_1)) \right. \\ & + \frac{1}{\varepsilon_1} (\exp(-ijKx_3) - \exp(-ijKx_2)) + \frac{1}{\varepsilon_2} (\exp(-ijKx_4) - \exp(-ijKx_3)) \\ & \left. + \frac{1}{\varepsilon_1} (\exp(-ijKL_x) - \exp(-ijKx_4)) \right] \end{aligned} \quad (\text{B.2.4})$$

## B.3 Evaluation of scalar product integral

Equation (3.1.34) gives the formal definition of a scalar product used to normalise the mode profiles. This appendix will evaluate this integral analytically. There are two cases of interest: TM and TE polarization. Starting with TM polarization, the first step is to insert the plane wave expansions for  $e_x$  and  $h_y$  given in equations (3.1.4) and (3.1.3) into equation (3.1.34):

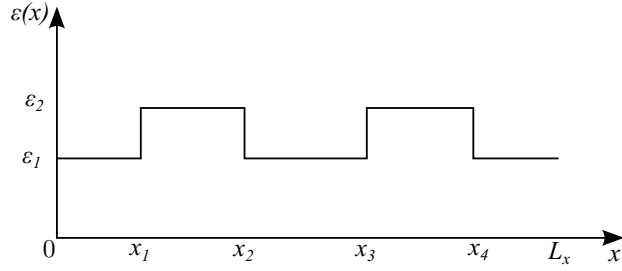


**Figure B.2:** Illustration of the dielectric function in a single layer of a PhC.

$$\begin{aligned}
\langle \mathbf{e}_m | \mathbf{h}_n \rangle &= \int (\mathbf{e}_{xm} \times \mathbf{h}_{yn}) \cdot \hat{\mathbf{z}} dx = \int (\mathbf{e}_{xm} \times \mathbf{h}_{yn}) \cdot \hat{\mathbf{z}} dx \\
&= \int_0^{L_x} \left[ \left( \sum_{j=-M}^{j=M} u_{m,j} \exp(i(jK + \alpha/Lx)x) \right) \hat{\mathbf{x}} \right. \\
&\quad \left. \times \left( \sum_{j'=-M}^{j'=M} v_{n,j'} \exp(i(j'K + \alpha/Lx)x) \right) \hat{\mathbf{y}} \right] \cdot \hat{\mathbf{z}} dx. \quad (\text{B.3.1})
\end{aligned}$$

From now on  $\alpha = 0$ , since this is the case for all simulations performed in this project. Now evaluating the crossproduct and remembering that  $(\hat{\mathbf{x}} \times \hat{\mathbf{y}}) \cdot \hat{\mathbf{z}} = 1$  the expression becomes:

$$\begin{aligned}
\langle \mathbf{e}_m | \mathbf{h}_n \rangle &= \int_0^{L_x} \left[ \left( \sum_{j=-M}^{j=M} u_{m,j} \exp(i(jK + \alpha/Lx)x) \right) \hat{\mathbf{x}} \right. \\
&\quad \left. \times \left( \sum_{j'=-M}^{j'=M} v_{n,j'} \exp(i(j'K + \alpha/Lx)x) \right) \hat{\mathbf{y}} \right] \cdot \hat{\mathbf{z}} dx \\
&= \sum_j \sum_{j'} u_{m,j} v_{n,j'} \int_0^{L_x} \exp(iK(j + j')x) dx, \quad (\text{B.3.2})
\end{aligned}$$

where it is noted that the integral is in fact a Kronecker delta,  $\delta_{j,-j'}$ . Using this the scalar product reduces to:

$$\langle \mathbf{e}_m | \mathbf{h}_n \rangle = \sum_j \sum_{j'} u_{m,j} v_{n,j'} L_x \delta_{j,-j'} = L_x \sum_j u_{m,j} v_{n,-j}, \quad \text{TM} \quad (\text{B.3.3})$$

For the case of TE polarization the derivation is very similar. The only difference is that the cross product is now  $(\hat{\mathbf{y}} \times \hat{\mathbf{x}}) \cdot \hat{\mathbf{z}} = -1$ , thereby changing the sign of equation (B.3.3):

$$\langle \mathbf{e}_m | \mathbf{h}_n \rangle = - \sum_j \sum_{j'} u_{m,j} v_{n,j'} L_x \delta_{j,-j'} = -L_x \sum_j u_{m,j} v_{n,-j}, \quad \text{TE} \quad (\text{B.3.4})$$

## B.4 Transmission and reflection matrices

First the equation (3.1.44) will be written in matrix form. For convenience the equation is restated here:

$$2\delta_{mn} = \sum_{j=1}^N (\langle \mathbf{e}_{2j} | \mathbf{h}_{1n} \rangle + \langle \mathbf{e}_{1n} | \mathbf{h}_{2j} \rangle) t_{12;jm}. \quad (\text{B.4.1})$$

The subscripts  $jm$  in  $t_{12;jm}$  means the element in the  $j$ 'th row and the  $m$ 'th column and likewise  $\langle \mathbf{e}_{2j} | \mathbf{h}_{1n} \rangle$  is the  $(j, n)$ -element of the scalar product matrix  $\overline{\langle \mathbf{e}_2 | \mathbf{h}_1 \rangle}$ . Now the sum can be replaced by a dot product as:

$$2\delta_{mn} = \overline{\langle \mathbf{e}_2 | \mathbf{h}_{1n} \rangle}^T \cdot \overline{t_{12;;m}} + \overline{\langle \mathbf{e}_{1n} | \mathbf{h}_{2:} \rangle} \cdot \overline{t_{12;;m}}, \quad (\text{B.4.2})$$

where  $T$  denotes transposition and  $:$ , means all elements in the column or row depending on whether  $:$  is the first or last subscript respectively. The transposition is needed for the next step when going from vectors to matrices. Now  $\overline{\langle \mathbf{e}_2 | \mathbf{h}_{1n} \rangle}^T \cdot \overline{t_{12;;m}}$  means the  $n$ 'th row of  $\overline{\langle \mathbf{e}_2 | \mathbf{h}_1 \rangle}^T$  dotted with the  $m$ 'th column of  $\overline{t_{12}}$  and this gives exactly the  $(n, m)$  element of a matrix. So doing this for all rows and columns the result is matrix multiplication:

$$2\overline{\overline{I}} = \left( \overline{\langle \mathbf{e}_2 | \mathbf{h}_1 \rangle}^T + \overline{\langle \mathbf{e}_1 | \mathbf{h}_2 \rangle} \right) \overline{t_{12}}, \quad (\text{B.4.3})$$

where the  $\overline{\overline{I}}$  is the identity matrix appearing from the Kronecker delta,  $\delta_{mn}$ . Isolating  $\overline{t_{12}}$  gives the transmission matrix:

$$\overline{t_{12}} = 2 \left( \overline{\langle \mathbf{e}_2 | \mathbf{h}_1 \rangle}^T + \overline{\langle \mathbf{e}_1 | \mathbf{h}_2 \rangle} \right)^{-1}. \quad (\text{B.4.4})$$

With similar considerations equation (3.1.45) can be written in matrix form as:

$$\overline{r_{12}} = \frac{1}{2} \left( \overline{\langle \mathbf{e}_2 | \mathbf{h}_1 \rangle}^T + \overline{\langle \mathbf{e}_1 | \mathbf{h}_2 \rangle} \right) \overline{t_{12}}. \quad (\text{B.4.5})$$

## B.5 Implementation of scattering matrix formalism

Implementing the scattering matrix formalism (equations (3.1.58)-(3.1.65)) demands a good and systematic bookkeeping system. The *cell*-type in Matlab have been really useful for this, since this allows to store a lot of matrices in a single cell - and these matrices do not even have to be the same size! Actually anything can be stored in a Matlab cell - no matter what type it is.

In the equations (3.1.58)-(3.1.65) there is an matrix inversion. In Matlab performing such an inversion by typing:  $M^{-1}$  is numerically unstable according to Matlab documentation. Instead the  $\backslash$  operator should be used. This operator is defined as:  $\overline{\overline{A}}^{-1} \overline{\overline{B}} = \overline{\overline{A}} \backslash \overline{\overline{B}}$ .

The first step in implementing the scattering matrix formalism is therefore to calculate the matrices that need to be inverted:

$$\overline{\overline{\text{InvM}_1}} = \overline{\overline{I}} - \overline{\overline{r_{q1}p_q^-} \overline{\overline{r_{q,q+1}p_q^+}}} \quad (\text{B.5.1})$$

$$\overline{\overline{\text{InvM}_2}} = \overline{\overline{I}} - \overline{\overline{r_{q,q-1}p_q^-} \overline{\overline{r_{q,N}p_q^+}}} \quad (\text{B.5.2})$$

Then these matrices can be used in the equations (3.1.58)-(3.1.65) by using the \ operator in Matlab. Below the implementation in equation (3.1.58) and (3.1.65) are shown:

$$\overline{\overline{r_{1,q+1}}} = \overline{\overline{r_{1q}}} + \overline{\overline{t_{q1}p_q^-} \overline{\overline{r_{q,q+1}p_q^+} \overline{\overline{\text{InvM}_1}} \backslash \overline{\overline{t_{1q}}}} \quad (\text{B.5.3})$$

$$\overline{\overline{t_{N,q-1}}} = \overline{\overline{t_{q,q-1}p_q^-} \overline{\overline{t_{N,q}}} + \overline{\overline{t_{q,q-1}p_q^-} \overline{\overline{r_{q,N}p_q^+} \overline{\overline{\text{InvM}_2}} \backslash \left( \overline{\overline{r_{q,q-1}p_q^-} \overline{\overline{t_{N,q}}} \right)} \quad (\text{B.5.4})$$

where the parenthesis in the second line are shown to clarify the factorial order of the matrices. The matrices are then stored in a Matlab cell of size  $(1 \times N - 1)$  as shown below:

$$\text{Cell}(\overline{\overline{r_{1,q}}}) = \{ \overline{\overline{r_{12}}, \overline{\overline{r_{13}}, \dots, \overline{\overline{r_{1N}}} \} \quad (\text{B.5.5})$$

$$\text{Cell}(\overline{\overline{t_{N,q}}}) = \{ \overline{\overline{r_{N1}}, \overline{\overline{r_{N2}}, \dots, \overline{\overline{r_{N,N-1}}} \} \quad (\text{B.5.6})$$

## B.6 Derivation of generalized eigenvalue problem for Bloch modes

The starting point for deriving equation (3.1.81) are equations (3.1.79) and (3.1.80), which are restated here for simplicity:

$$\begin{bmatrix} \overline{\overline{c_4}} \\ \overline{\overline{d'_1}} \end{bmatrix} = \begin{bmatrix} \overline{\overline{S_{11}}} & \overline{\overline{S_{12}}} \\ \overline{\overline{S_{12}}} & \overline{\overline{S_{22}}} \end{bmatrix} \begin{bmatrix} \overline{\overline{c_1}} \\ \overline{\overline{d'_4}} \end{bmatrix}, \quad (\text{B.6.1})$$

$$\begin{bmatrix} \overline{\overline{c_4}} \\ \overline{\overline{d'_4}} \end{bmatrix} = \Lambda \begin{bmatrix} \overline{\overline{c_1}} \\ \overline{\overline{d'_1}} \end{bmatrix}. \quad (\text{B.6.2})$$

Now equation (B.6.1) will be written into two equations and Bloch's theorem is then applied:

$$\begin{bmatrix} \overline{c_4} \\ \overline{d'_1} \end{bmatrix} = \begin{bmatrix} \overline{S_{11}} & \overline{S_{12}} \\ \overline{S_{12}} & \overline{S_{22}} \end{bmatrix} \begin{bmatrix} \overline{c_1} \\ \overline{d'_4} \end{bmatrix} \Rightarrow \quad (\text{B.6.3})$$

$$\left\{ \begin{array}{l} \overline{c_4} = \overline{S_{11}}\overline{c_1} + \overline{S_{12}}\overline{d'_4} \\ \overline{d'_1} = \overline{S_{12}}\overline{c_1} + \overline{S_{22}}\overline{d'_4} \end{array} \right\} \Rightarrow \quad (\text{B.6.4})$$

$$\left\{ \begin{array}{l} \Lambda\overline{c_1} = \overline{S_{11}}\overline{c_1} + \Lambda\overline{S_{12}}\overline{d'_1} \\ \overline{d'_1} = \overline{S_{12}}\overline{c_1} + \Lambda\overline{S_{22}}\overline{d'_1} \end{array} \right\}. \quad (\text{B.6.5})$$

Then the last equation above is rearranged such that the eigenvalue,  $\Lambda$ , is on the rhs and such that the sign in front of  $\overline{c_1}$  and  $\overline{d'_4}$  are the same in both equations:

$$\left\{ \begin{array}{l} \overline{S_{11}}\overline{c_1} = \Lambda\overline{c_1} - \Lambda\overline{S_{12}}\overline{d'_1} \\ \overline{S_{12}}\overline{c_1} - \overline{d'_1} = -\Lambda\overline{S_{22}}\overline{d'_1} \end{array} \right\}. \quad (\text{B.6.6})$$

This equation can then be written in matrix form leading to the generalized eigenvalue problem:

$$\left\{ \begin{array}{l} \overline{S_{11}}\overline{c_1} + \overline{0}d'_1 = \Lambda \left( \overline{I}c_1 - \overline{S_{12}}d'_1 \right) \\ \overline{S_{12}}\overline{c_1} - \overline{d'_1} = \Lambda \left( \overline{0}c_1 - \overline{S_{22}}d'_1 \right) \end{array} \right\} \Rightarrow \quad (\text{B.6.7})$$

$$\begin{bmatrix} \overline{S_{11}} & \overline{0} \\ \overline{S_{12}} & -\overline{I} \end{bmatrix} \begin{bmatrix} \overline{c_1} \\ \overline{d'_1} \end{bmatrix} = \Lambda \begin{bmatrix} \overline{I} & -\overline{S_{12}} \\ \overline{0} & -\overline{S_{22}} \end{bmatrix} \begin{bmatrix} \overline{c_1} \\ \overline{d'_1} \end{bmatrix} \quad (\text{B.6.8})$$

Thereby the Bloch expansion vectors are found by solving the above generalized eigenvalue problem.

## B.7 Evaluation of power flow integral

The power flow integral given in equation (3.1.84) is here evaluated. For convenience the integral is restated here:

$$P_m = \frac{1}{2} \int \text{Re} (\mathbf{\Psi}_m^E \times \mathbf{\Psi}_m^{H*}) \cdot \hat{\mathbf{z}} d\mathbf{r}_\perp. \quad (\text{B.7.1})$$

For evaluating this integral the definition of the Bloch modes,  $\mathbf{\Psi}_m^E$  and  $\mathbf{\Psi}_m^H$ , given in equations (3.1.75) and (3.1.76) is used and they are also restated here without the periodic section and layer subindices,  $w$  and  $q$ , for simplicity:

$$\Psi_m^{E\pm}(\mathbf{r}_\perp, z) = \sum_{j=1}^N [c_{mj}^\pm \mathbf{e}_j^\pm(\mathbf{r}_\perp) \exp(i\beta_j(z-z')) + d_{mj}^\pm \mathbf{e}_j^\mp(\mathbf{r}_\perp) \exp(-i\beta_j(z-z'))], \quad (\text{B.7.2})$$

$$\Psi_m^{H\pm}(\mathbf{r}_\perp, z) = \sum_{j=1}^N [c_{mj}^\pm \mathbf{h}_j^\pm(\mathbf{r}_\perp) \exp(i\beta_j(z-z')) + d_{mj}^\pm \mathbf{h}_j^\mp(\mathbf{r}_\perp) \exp(-i\beta_j(z-z'))], \quad (\text{B.7.3})$$

The derivation will be done for TM polarized light. Inserting the expansion for the eigenmodes given in equations (3.1.3) and (3.1.4) into equations (B.7.2) and (B.7.3) the Bloch modes for TM polarized light becomes:

$$\Psi_m^E(x, z) = \sum_{j=1}^N \left[ c_{mj} \sum_l u_{lj} \exp(ilKx) + d_{mj} \sum_{l'} u_{l'j} \exp(il'Kx) \right] \hat{x}, \quad (\text{B.7.4})$$

$$\Psi_m^H(x, z) = \sum_{j'=1}^N \left[ c_{mj'} \sum_n v_{nj'} \exp(inKx) - d_{mj'} \sum_{n'} v_{n'j'} \exp(in'Kx) \right] \hat{y}, \quad (\text{B.7.5})$$

where  $n$  is an index and NOT the *refractive index*. Equations (B.7.4) and (B.7.5) are now inserted in equation (B.7.1) giving:

$$P_m = \frac{1}{2} \int \text{Re}(\Psi_m^E \times \Psi_m^{H*}) \cdot \hat{\mathbf{z}} d\mathbf{r}_\perp \quad (\text{B.7.6})$$

$$\begin{aligned} &= \frac{1}{2} \int \text{Re} \left( \sum_{j=1}^N \left[ c_{mj} \sum_l u_{lj} \exp(ilKx) + d_{mj} \sum_{l'} u_{l'j} \exp(il'Kx) \right] \hat{x} \right. \\ &\quad \left. \times \sum_{j'=1}^N \left[ c_{mj'}^* \sum_n v_{nj'}^* \exp(-inKx) - d_{mj'}^* \sum_{n'} v_{n'j'}^* \exp(-in'Kx) \right] \hat{y} \right) \cdot \hat{\mathbf{z}} dx \end{aligned} \quad (\text{B.7.7})$$

$$\begin{aligned} &= \frac{1}{2} \text{Re} \left( \int \sum_{j,j'} \sum_{l,l',n,n'} (c_{mj} u_{lj} \exp(ilKx) + d_{mj} u_{l'j} \exp(il'Kx)) \right. \\ &\quad \left. \cdot (c_{mj'}^* u_{nj'}^* \exp(-inKx) - d_{mj'}^* u_{n'j'}^* \exp(-in'Kx)) dx \right) \end{aligned} \quad (\text{B.7.8})$$

$$\begin{aligned} &= \frac{1}{2} \text{Re} \left( \int \sum_{j,j'} \sum_{l,l',n,n'} [c_{mj} c_{mj'}^* u_{lj} v_{nj'}^* \exp(i(l-n)Kx) \right. \\ &\quad - c_{mj} d_{mj'}^* u_{lj} v_{n'j'}^* \exp(i(l-n')Kx) \\ &\quad + d_{mj} c_{mj'}^* u_{l'j} v_{nj'}^* \exp(i(l'-n)Kx) \\ &\quad \left. - d_{mj} d_{mj'}^* u_{l'j} v_{n'j'}^* \exp(i(l'-n')Kx)] dx \right). \end{aligned} \quad (\text{B.7.9})$$

Evaluating the integral in the last equation above will lead to four Kronecker delta functions, due to the complex exponentials:

$$P_m = \frac{1}{2} \text{Re} \left( \sum_{j,j'} \sum_{l,l',n,n'} [c_{mj} c_{mj'}^* u_{lj} v_{nj}^* \delta_{l,n} - c_{mj} d_{mj'}^* u_{lj} v_{n'j'}^* \delta_{l,n'} + d_{mj} c_{mj'}^* u_{l'j} v_{n'j'}^* \delta_{l',n} - d_{mj} d_{mj'}^* u_{l'j} v_{n'j'}^* \delta_{l',n'}] \right). \quad (\text{B.7.10})$$

The Kronecker delta functions then demand that  $l = n = n' = l'$  and this reduces the above equation to:

$$P_m = \frac{1}{2} \text{Re} \left( \sum_{j,j'} \sum_l [c_{mj} c_{mj'}^* u_{lj} v_{lj'}^* - c_{mj} d_{mj'}^* u_{lj} v_{lj'}^* + d_{mj} c_{mj'}^* u_{lj} v_{lj'}^* - d_{mj} d_{mj'}^* u_{lj} v_{lj'}^*] \right). \quad (\text{B.7.11})$$

Rearranging the terms leads to:

$$P_m = \frac{1}{2} \text{Re} \left( \sum_{j,j'} [c_{mj} \sum_l u_{lj} v_{lj'}^* (c_{mj'}^* - d_{mj'}^*) + d_{mj} \sum_l u_{lj} v_{lj'}^* (c_{mj'}^* - d_{mj'}^*)] \right). \quad (\text{B.7.12})$$

The sum over  $l$  is now defined as the  $(j, j')$  matrix element of a matrix,  $\overline{W}$ :

$$W_{j,j'} = \sum_l u_{lj} v_{lj'}^* = \overline{u}_j^T \cdot \overline{v}_{j'}^*. \quad (\text{B.7.13})$$

This means that the matrix  $\overline{W}$  is given by the matrix product:

$$\overline{W} = \overline{u}^T \overline{v}^*. \quad (\text{B.7.14})$$

Turning back to equation (B.7.12) and replacing the  $l$  sums with  $W_{j,j'}$  gives:

$$P_m = \frac{1}{2} \text{Re} \left( \sum_{j,j'} [c_{mj} W_{j,j'} (c_{mj'}^* - d_{mj'}^*) + d_{mj} W_{j,j'} (c_{mj'}^* - d_{mj'}^*)] \right). \quad (\text{B.7.15})$$

This equation can now be written in matrix form. For simplicity lets take a look at  $\sum_{j,j'} c_{mj} W_{j,j'} c_{mj'}^*$ . The sum can be replaced by dot products as:

$$\sum_{j,j'} c_{mj} W_{j,j'} c_{mj'}^* = \overline{c}_m^T \overline{W} \overline{c}_m^*, \quad (\text{B.7.16})$$

where the transposition is needed in order for getting a scalar instead of a vector. Doing the same vectorization on all the terms in equation (B.7.15) the power flow for the  $m$ 'th Bloch mode can be computed as:

$$P_m = \frac{1}{2} \text{Re} \left( \bar{c}_m^T \bar{W} (\bar{c}_m^* - \bar{d}_m^*) + \bar{d}_m^T \bar{W} (\bar{c}_m^* - \bar{d}_m^*) \right). \quad (\text{B.7.17})$$

When computing the eigenvalues,  $\Lambda_m$ , for the Bloch modes and then finding all Bloch modes with  $|\Lambda_m| = 1$  the power flow for all these Bloch modes can be found at once. This is done by letting the Bloch expansion vectors with  $|\Lambda_m| = 1$ ,  $\bar{c}_m$  and  $\bar{d}_m$ , be the columns in the matrices  $\bar{c}$  and  $\bar{d}$  respectively. In this way the power flow for all the Bloch modes can be found at once:

$$\bar{P} = \frac{1}{2} \text{Re} \left( \bar{c}^T \bar{W} (\bar{c}^* - \bar{d}^*) + \bar{d}^T \bar{W} (\bar{c}^* - \bar{d}^*) \right), \quad (\text{B.7.18})$$

where the power flows are given in the diagonal of  $\bar{P}$ , such that the power flow for the  $m$ 'th Bloch mode is given by:

$$P_m = \bar{P}(m, m) = P_{m,m}. \quad (\text{B.7.19})$$

## B.8 Derivation of transmission and reflection matrices between periodic sections

The derivation of the transmission and reflection matrices for adjacent periodic sections starts with equations (3.1.88) and (3.1.89). They are repeated here for convenience:

$$\Psi_{\perp 1m}^{E+}(\mathbf{r}_{\perp}) + \sum_j^N \Psi_{\perp 1j}^{E-}(\mathbf{r}_{\perp}) r_{b,12;jm} = \sum_j^N \Psi_{\perp 2j}^{E+}(\mathbf{r}_{\perp}) t_{b,12;jm}, \quad (\text{B.8.1})$$

$$\Psi_{\perp 1m}^{H+}(\mathbf{r}_{\perp}) + \sum_j^N \Psi_{\perp 1j}^{H-}(\mathbf{r}_{\perp}) r_{b,12;jm} = \sum_j^N \Psi_{\perp 2j}^{H+}(\mathbf{r}_{\perp}) t_{b,12;jm}. \quad (\text{B.8.2})$$

Inserting the expansions of the Bloch modes given in equations (3.1.75) and (3.1.76), setting  $z = z'$  and change every  $d$  to  $d'$  (since the expressions above are valid only at an interface) gives:

$$\begin{aligned}
 \sum_l^N [c_{1ml}^+ \mathbf{e}_{\perp 1l}^+(\mathbf{r}_{\perp}) + d_{1ml}^{\prime+} \mathbf{e}_{\perp 1l}^-(\mathbf{r}_{\perp})] + \sum_j^N \sum_l^N [c_{1jl}^- \mathbf{e}_{\perp 1l}^+(\mathbf{r}_{\perp}) + d_{jl}^{\prime-} \mathbf{e}_{\perp 1l}^-(\mathbf{r}_{\perp})] r_{b,12;jm} \\
 = \sum_j^N \sum_l^N [c_{2jl}^+ \mathbf{e}_{\perp 2l}^+(\mathbf{r}_{\perp}) + d_{2jl}^{\prime+} \mathbf{e}_{\perp 2l}^-(\mathbf{r}_{\perp})] t_{b,12;jm},
 \end{aligned} \tag{B.8.3}$$

$$\begin{aligned}
 \sum_l^N [c_{1ml}^+ \mathbf{h}_{\perp 1l}^+(\mathbf{r}_{\perp}) + d_{1ml}^{\prime+} \mathbf{h}_{\perp 1l}^-(\mathbf{r}_{\perp})] + \sum_j^N \sum_l^N [c_{1jl}^- \mathbf{h}_{\perp 1l}^+(\mathbf{r}_{\perp}) + d_{jl}^{\prime-} \mathbf{h}_{\perp 1l}^-(\mathbf{r}_{\perp})] r_{b,12;jm} \\
 = \sum_j^N \sum_l^N [c_{2jl}^+ \mathbf{h}_{\perp 2l}^+(\mathbf{r}_{\perp}) + d_{2jl}^{\prime+} \mathbf{h}_{\perp 2l}^-(\mathbf{r}_{\perp})] t_{b,12;jm}.
 \end{aligned} \tag{B.8.4}$$

Using that  $\mathbf{e}_{\perp}^- = \mathbf{e}_{\perp}^+ = \mathbf{e}_{\perp}$  and  $\mathbf{h}_{\perp}^- = -\mathbf{h}_{\perp}^+ = -\mathbf{h}_{\perp}$  the above expressions becomes:

$$\begin{aligned}
 \sum_l^N [c_{1ml}^+ \mathbf{e}_{\perp 1l}(\mathbf{r}_{\perp}) + d_{1ml}^{\prime+} \mathbf{e}_{\perp 1l}(\mathbf{r}_{\perp})] + \sum_j^N \sum_l^N [c_{1jl}^- \mathbf{e}_{\perp 1l}(\mathbf{r}_{\perp}) + d_{jl}^{\prime-} \mathbf{e}_{\perp 1l}(\mathbf{r}_{\perp})] r_{b,12;jm} \\
 = \sum_j^N \sum_l^N [c_{2jl}^+ \mathbf{e}_{\perp 2l}(\mathbf{r}_{\perp}) + d_{2jl}^{\prime+} \mathbf{e}_{\perp 2l}(\mathbf{r}_{\perp})] t_{b,12;jm},
 \end{aligned} \tag{B.8.5}$$

$$\begin{aligned}
 \sum_l^N [c_{1ml}^+ \mathbf{h}_{\perp 1l}(\mathbf{r}_{\perp}) - d_{1ml}^{\prime+} \mathbf{h}_{\perp 1l}(\mathbf{r}_{\perp})] + \sum_j^N \sum_l^N [c_{1jl}^- \mathbf{h}_{\perp 1l}(\mathbf{r}_{\perp}) - d_{jl}^{\prime-} \mathbf{h}_{\perp 1l}(\mathbf{r}_{\perp})] r_{b,12;jm} \\
 = \sum_j^N \sum_l^N [c_{2jl}^+ \mathbf{h}_{\perp 2l}(\mathbf{r}_{\perp}) - d_{2jl}^{\prime+} \mathbf{h}_{\perp 2l}(\mathbf{r}_{\perp})] t_{b,12;jm},
 \end{aligned} \tag{B.8.6}$$

and these expressions are now ready to be rearranged into equations (3.1.90) and (3.1.91). This is done by collecting the sums and setting all  $\mathbf{e}_{\perp}$ s and  $\mathbf{h}_{\perp}$ s outside parenthesis:

$$\begin{aligned}
& \sum_l^N \mathbf{e}_{\perp 1l}(\mathbf{r}_{\perp}) \left( (c_{1ml}^+ + d_{1ml}^+) + \sum_j^N (c_{1jl}^- + d_{jl}^{\prime-}) r_{b,12;jm} \right) \\
&= \sum_{j,l}^N \mathbf{e}_{\perp 2l}(\mathbf{r}_{\perp}) (c_{2jl}^+ + d_{2jl}^{\prime+}) t_{b,12;jm}, \tag{B.8.7}
\end{aligned}$$

$$\begin{aligned}
& \sum_l^N \mathbf{h}_{\perp 1l}(\mathbf{r}_{\perp}) \left( (c_{1ml}^+ - d_{1ml}^+) + \sum_j^N (c_{1jl}^- - d_{jl}^{\prime-}) r_{b,12;jm} \right) \\
&= \sum_{j,l}^N \mathbf{h}_{\perp 2l}(\mathbf{r}_{\perp}) (c_{2jl}^+ - d_{2jl}^{\prime+}) t_{b,12;jm} \tag{B.8.8}
\end{aligned}$$

These equations should now be put into matrix form. First step is to multiply the bra version of equation (B.8.7) with  $|\mathbf{h}_{1n}\rangle$  and the ket version of equation (B.8.8) with  $\langle \mathbf{e}_{1n}|$ . Doing this leads to:

$$\begin{aligned}
& \sum_l^N \langle \mathbf{e}_{1l} | \mathbf{h}_{1n} \rangle \left( (c_{1ml}^+ + d_{1ml}^+) + \sum_j^N (c_{1jl}^- + d_{jl}^{\prime-}) r_{b,12;jm} \right) \\
&= \sum_{j,l}^N \langle \mathbf{e}_{2l} | \mathbf{h}_{1n} \rangle (c_{2jl}^+ + d_{2jl}^{\prime+}) t_{b,12;jm}, \tag{B.8.9}
\end{aligned}$$

$$\begin{aligned}
& \sum_l^N \langle \mathbf{e}_{1n} | \mathbf{h}_{1l} \rangle \left( (c_{1ml}^+ - d_{1ml}^+) + \sum_j^N (c_{1jl}^- - d_{jl}^{\prime-}) r_{b,12;jm} \right) \\
&= \sum_{j,l}^N \langle \mathbf{e}_{1n} | \mathbf{h}_{2l} \rangle (c_{2jl}^+ - d_{2jl}^{\prime+}) t_{b,12;jm}, \tag{B.8.10}
\end{aligned}$$

where  $\perp$  has been dropped for simplicity. Due to that the field modes are orthonormal to each other the above expression are reduced further, using  $\langle \mathbf{e}_{1l} | \mathbf{h}_{1n} \rangle = \delta_{ln}$ :

$$1 \cdot (c_{1mn}^+ + d_{1mn}^{\prime+}) + 1 \cdot \sum_j^N (c_{1jn}^- + d_{1jn}^{\prime-}) r_{b,12;jm} = \sum_{j,l}^N \langle \mathbf{e}_{2l} | \mathbf{h}_{1n} \rangle (c_{2jn}^+ + d_{2jn}^{\prime+}) t_{b,12;jm}, \tag{B.8.11}$$

$$1 \cdot (c_{1mn}^+ - d_{1mn}^{\prime+}) + 1 \cdot \sum_j^N (c_{1jn}^- - d_{1jn}^{\prime-}) r_{b,12;jm} = \sum_{j,l}^N \langle \mathbf{e}_{1n} | \mathbf{h}_{2l} \rangle (c_{2jn}^+ - d_{2jn}^{\prime+}) t_{b,12;jm}. \tag{B.8.12}$$

Now the equations are ready to be put into matrix form. The scalar product  $\overline{\langle \mathbf{e}_{2l} | \mathbf{h}_{1n} \rangle}$  needs to be transposed in order for the elements to be summed correctly. Otherwise it is straightforward and the equations in matrix form are:

$$\left(\overline{\overline{c_1^+}} + \overline{\overline{d_1^+}}\right) + \left(\overline{\overline{c_1^-}} + \overline{\overline{d_1^-}}\right) \overline{\overline{r_{b,12}}} = \overline{\overline{\langle \mathbf{e}_2 | \mathbf{h}_1 \rangle}}^T \left(\overline{\overline{c_2^+}} + \overline{\overline{d_2^+}}\right) \overline{\overline{t_{b,12}}}, \quad (\text{B.8.13})$$

$$\left(\overline{\overline{c_1^+}} - \overline{\overline{d_1^+}}\right) + \left(\overline{\overline{c_1^-}} - \overline{\overline{d_1^-}}\right) \overline{\overline{r_{b,12}}} = \overline{\overline{\langle \mathbf{e}_1 | \mathbf{h}_2 \rangle}} \left(\overline{\overline{c_2^+}} - \overline{\overline{d_2^+}}\right) \overline{\overline{t_{b,12}}}. \quad (\text{B.8.14})$$

Isolating  $\overline{\overline{r_{b,12}}}$  in the top equation gives:

$$\overline{\overline{r_{b,12}}} = \left(\overline{\overline{c_1^-}} + \overline{\overline{d_1^-}}\right)^{-1} \overline{\overline{\langle \mathbf{e}_2 | \mathbf{h}_1 \rangle}}^T \left(\overline{\overline{c_2^+}} + \overline{\overline{d_2^+}}\right) \overline{\overline{t_{b,12}}} - \left(\overline{\overline{c_1^-}} + \overline{\overline{d_1^-}}\right)^{-1} \left(\overline{\overline{c_1^+}} + \overline{\overline{d_1^+}}\right), \quad (\text{B.8.15})$$

and inserting this in equation (B.8.14) leads to:

$$\begin{aligned} & \left(\overline{\overline{c_1^-}} - \overline{\overline{d_1^-}}\right)^{-1} \left(\overline{\overline{c_1^+}} - \overline{\overline{d_1^+}}\right) + \left(\overline{\overline{c_1^-}} + \overline{\overline{d_1^-}}\right)^{-1} \overline{\overline{\langle \mathbf{e}_2 | \mathbf{h}_1 \rangle}}^T \left(\overline{\overline{c_2^+}} + \overline{\overline{d_2^+}}\right) \overline{\overline{t_{b,12}}} \\ & - \left(\overline{\overline{c_1^-}} + \overline{\overline{d_1^-}}\right)^{-1} \left(\overline{\overline{c_1^+}} + \overline{\overline{d_1^+}}\right) = \left(\overline{\overline{c_1^-}} - \overline{\overline{d_1^-}}\right)^{-1} \overline{\overline{\langle \mathbf{e}_1 | \mathbf{h}_2 \rangle}} \left(\overline{\overline{c_2^+}} - \overline{\overline{d_2^+}}\right) \overline{\overline{t_{b,12}}} \quad \Rightarrow \end{aligned} \quad (\text{B.8.16})$$

$$\begin{aligned} \overline{\overline{t_{b,12}}} &= \left[ \left(\overline{\overline{c_1^+}} + \overline{\overline{d_1^+}}\right)^{-1} \overline{\overline{\langle \mathbf{e}_2 | \mathbf{h}_1 \rangle}}^T \left(\overline{\overline{c_2^+}} + \overline{\overline{d_2^+}}\right) - \left(\overline{\overline{c_1^-}} - \overline{\overline{d_1^-}}\right)^{-1} \overline{\overline{\langle \mathbf{e}_1 | \mathbf{h}_2 \rangle}} \left(\overline{\overline{c_2^+}} - \overline{\overline{d_2^+}}\right) \right]^{-1} \\ & \times \left[ \left(\overline{\overline{c_1^-}} + \overline{\overline{d_1^-}}\right)^{-1} \left(\overline{\overline{c_1^+}} + \overline{\overline{d_1^+}}\right) - \left(\overline{\overline{c_1^-}} - \overline{\overline{d_1^-}}\right)^{-1} \left(\overline{\overline{c_1^+}} - \overline{\overline{d_1^+}}\right) \right]. \end{aligned} \quad (\text{B.8.17})$$

Thereby equations (3.1.92) and (3.1.93) have been derived.

## B.9 Visualization of field profile in all supercells

The first step in visualizing the full field profile is to use Bloch's theorem (equation (3.1.70)) in all periodic sections in order to find the Bloch modes in every supercell in all periodic sections. The electric and magnetic fields are expanded on these Bloch modes as in equations (3.1.73) and (3.1.74) and the next step is thus to find the amplitude of these Bloch modes in each periodic section. Consider the three section geometry in the middle of Figure B.3. The structure is illuminated with the Bloch field amplitudes  $\overline{\overline{a_{s1}}}$  and  $\overline{\overline{b_{s3}}}$ . Then the structure is reduced to a three section geometry as illustrated in the left part of Figure B.3 where the Bloch mode amplitudes are illustrated. These Bloch mode amplitudes are found using the scattering reflection and transmission matrices for the periodic sections in equations (3.1.66) and (3.1.67). Doing this the Bloch mode amplitudes in the  $w$ 'th periodic section is given as:

$$\overline{\overline{a_w}} = \left(\overline{\overline{I}} - \overline{\overline{r_{b,w1} p_w^+ r_{b,wn} p_w^+}}\right)^{-1} \left(\overline{\overline{t_{b,1w} a_1^+}} + \overline{\overline{r_{b,w1} p_w^- t_{b,nw} b_n^+}}\right), \quad (\text{B.9.1})$$

$$\overline{\overline{b_w}} = \left(\overline{\overline{I}} - \overline{\overline{r_{b,wn} p_w^+ r_{b,w1} p_w^-}}\right)^{-1} \left(\overline{\overline{r_{b,wn} p_w^+ t_{b,1w} a_1^+}} + \overline{\overline{t_{b,nw} b_n^+}}\right), \quad (\text{B.9.2})$$

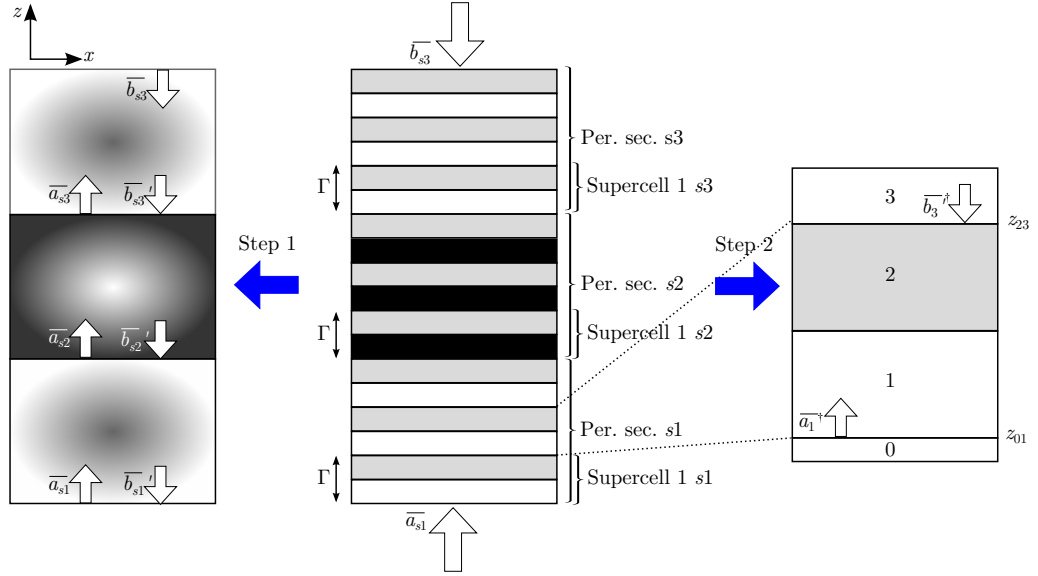


**Figure B.3:** Illustration of how the fields are computed in a multi section geometry. The central figure is the full structure, with three sections, supercells and layers. The figure to the left is three section geometry of the full structure with the Bloch mode amplitudes defined. The right figure is a zoom of a super cell used to compute the fields inside the supercells.

where  $n$  is the total number of sections.

Having determined the Bloch modes in all supercells and the Bloch mode amplitudes in all periodic sections the electric and magnetic field at any supercell interface are given by inserting equations (3.1.75) and (3.1.76) into equations (3.1.73) and (3.1.74) respectively with  $z = z'$ . For the supercell in the right part of Figure B.3 the electric and magnetic fields at the two supercell interfaces are given as:

$$\mathbf{E}(z_{01}) = \sum_j^N \left( a_{1j}^{\dagger} \mathbf{e}_j^+ + b_{1j}^{\dagger} \mathbf{e}_j^- \right), \quad (\text{B.9.3})$$

$$\mathbf{E}(z_{23}) = \sum_j^N \left( a_{3j}^{\dagger} \mathbf{e}_j^+ + b_{3j}^{\dagger} \mathbf{e}_j^- \right), \quad (\text{B.9.4})$$

$$\mathbf{H}(z_{01}) = \sum_j^N \left( a_{1j}^{\dagger} \mathbf{h}_j^+ + b_{1j}^{\dagger} \mathbf{h}_j^- \right), \quad (\text{B.9.5})$$

$$\mathbf{H}(z_{23}) = \sum_j^N \left( a_{3j}^{\dagger} \mathbf{h}_j^+ + b_{3j}^{\dagger} \mathbf{h}_j^- \right), \quad (\text{B.9.6})$$

where  $a_{1j}^{\dagger}$ ,  $a_{3j}^{\dagger}$ ,  $b_{1j}^{\dagger}$  and  $b_{3j}^{\dagger}$  are given as:

$$a_{1j}^\dagger = \sum_m^N (a_{1m} c_{1,2;mj}^+ + b_{1m} c_{1,2;mj}^-), \quad (\text{B.9.7})$$

$$b_{1j}^{\prime\dagger} = \sum_m^N (a_{1m} d_{1,2;mj}^+ + b_{1m} d_{1,2;mj}^-), \quad (\text{B.9.8})$$

$$a_{3j}^\dagger = \sum_m^N (a_{1m} c_{1,3;mj}^+ + b_{1m} c_{1,3;mj}^-), \quad (\text{B.9.9})$$

$$b_{3j}^{\prime\dagger} = \sum_m^N (a_{1m} d_{1,3;mj}^+ + b_{1m} d_{1,3;mj}^-), \quad (\text{B.9.10})$$

and here you need to pay attention to the indexing since it can be quite confusing. The first index of  $a_{1j}^\dagger$ ,  $a_{3j}^\dagger$ ,  $b_{1j}^{\prime\dagger}$  and  $b_{3j}^{\prime\dagger}$  is referring to the *layer* number in the supercell in Figure B.3 right. The amplitudes of the Bloch modes are kept constant within each periodic section so the first index of  $a_{1m}$  and  $b_{1m}$  means that we are within the first periodic section. The first index on the  $c$ 's and  $d$ 's specify the periodic section and the second index specify the supercell within the periodic section. Equations (B.9.7) - (B.9.10) can be written in matrix form as:

$$\overline{a_1^\dagger} = \overline{c_{1,2}^+} \overline{a_1} + \overline{c_{1,2}^-} \overline{b_1} \quad (\text{B.9.11})$$

$$\overline{b_1^\dagger} = \overline{d_{1,2}^+} \overline{a_1} + \overline{d_{1,2}^-} \overline{b_1} \quad (\text{B.9.12})$$

$$\overline{a_3^\dagger} = \overline{c_{1,3}^+} \overline{a_3} + \overline{c_{1,3}^-} \overline{b_3} \quad (\text{B.9.13})$$

$$\overline{b_3^\dagger} = \overline{d_{1,3}^+} \overline{a_3} + \overline{d_{1,3}^-} \overline{b_3} \quad (\text{B.9.14})$$

Thereby the electric and magnetic field can be found at all supercell interfaces. The final step for computing the fields within the whole geometry is thus to find the fields within all layers in all supercells. This is done by considering the right figure in Figure B.3.  $\overline{a_1^\dagger}$  and  $\overline{b_3^\dagger}$  are now used as sources for the supercell geometry. Then using the standard scattering matrix formalism  $\overline{a_q^\dagger}$  and  $\overline{b_q^{\prime\dagger}}$  can be found for all layers in the supercell (equations (3.1.66) and (3.1.67)). Note that the scattering between layer 0 and 1 should not be included in the field profile calculation. However, since the fields are expanded on the eigenmodes of layer 1 and 3, the transmission and reflection at the interface between layer 2 and 3 must be taken into account. This is illustrated in the right part of Figure B.3, by making layer 0 identical to layer 1 even though it is identical to layer 2 in the full structure. [16]

The electric and magnetic field in layer  $q$  within supercell  $o$  in periodic section  $w$  is then given as:

$$\mathbf{E}_{qow} = \sum_j^N \left[ a_{qow,j}^\dagger \mathbf{e}_{qow} \exp(i\beta_j(z-z')) + b_{qow,j}^\dagger \mathbf{e}_{qow} \exp(-i\beta_j(z-z')) \right], \quad (\text{B.9.15})$$

$$\mathbf{H}_{qow} = \sum_j^N \left[ a_{qow,j}^\dagger \mathbf{h}_{qow} \exp(i\beta_j(z-z')) - b_{qow,j}^\dagger \mathbf{h}_{qow} \exp(-i\beta_j(z-z')) \right]. \quad (\text{B.9.16})$$

These equations are then used for all layers in the PhC, giving the field in the whole geometry.

---

## Appendix for validation of method implementation

### C.1 Gap map computations

Various gap map computations have been carried out and compared with the gap maps in Appendix C in [17]. This Appendix will show the computed gap maps and compare them with the ones found in [17].

In Figure C.1 the gap map from [17] of a PhC consisting of dielectric rods in a triangular lattice is seen and next to it in Figure C.2 the corresponding gap map computed using the developed scripts is seen for TE polarized light. As in Figure 3.13 the computations are not reliable for  $r/a \geq 0.44$  and furthermore the lowest gap band in Figure C.2 has a line of points underneath which either should not be there or should be a part of the gap band, so the points in between are missing. The simulation parameters used are seen in Table C.1 and the unit cell is identical to one shown in Figure 3.14 except that the holes are now rods and the PhC medium is air.

**Table C.1:** Simulation parameters used for computing the gap map in Figure C.2.

Number of plane waves, $N$	Number of grid points in unit cell, $N_{g,unit}$	Number of unit cells, $N_{unit}$
27	51	1

Gap map computations on square lattices have also been carried out and such a computation are seen in Figure C.4 for TE polarization. The corresponding gap map from [17] is seen next to it in Figure C.3.

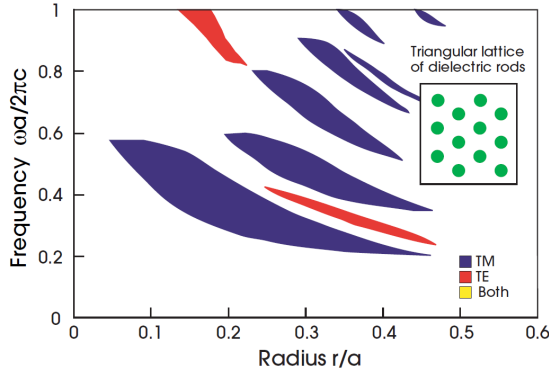


**Figure C.1:** Figure 6 in Appendix C from [17]. The dielectric constant of the rods is  $\varepsilon = 11.4$ . Note that the convention in [17] regarding polarization is opposite than the one used in this thesis - such that TE is TM and vice versa.

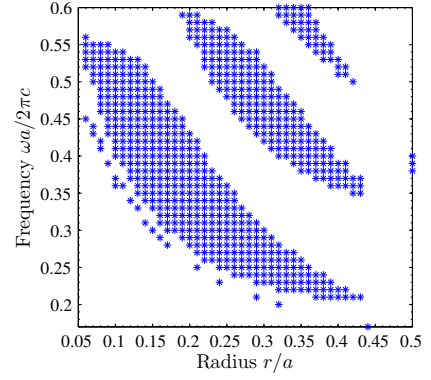


**Figure C.2:** TE gap map of a triangular lattice of dielectric rods with  $\varepsilon = 11.4$ . For  $r/a \geq 0.44$  the gap map does not behave as in Figure 3.12. The outlying point at  $r/a = 0.2$  is due to numerical instability.

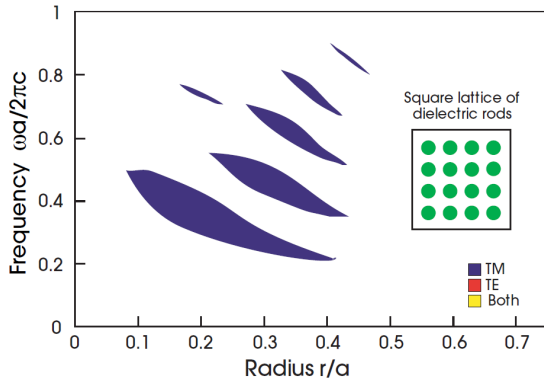


**Figure C.3:** Figure 4 in Appendix C from [17]. The dielectric constant of the rods is  $\varepsilon = 11.4$ . Note that the convention in [17] regarding polarization is opposite than the one used in this thesis - such that TE is TM and vice versa.

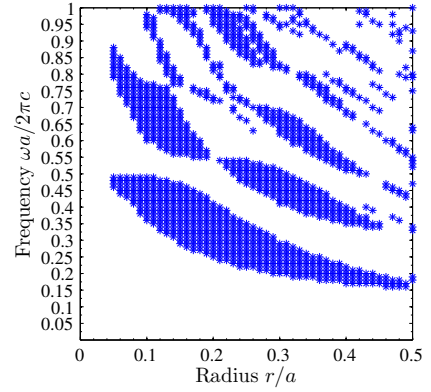


**Figure C.4:** TE gap map of a square lattice of dielectric rods with  $\varepsilon = 11.4$ . As seen the bands in Figure C.3 are reproduced but other bands have been found as well. Why this is the case have not been investigated further.

---

## Appendix for computations on PhC waveguides and microcavities

### D.1 Derivation of phase factors in coupled-mode theory

In order to derive equation (4.1.5) the phase term  $\exp(i(\theta_2 - \theta_1))$  in equation (4.1.3) needs to be determined. This is done by considering the requirements of energy conservation and time-reversal symmetry [6]. These requirements are derived in [12] and they are simply stated here:

$$d_1 = \sqrt{2\gamma_1} \exp(i\theta_1), \quad d_2 = \sqrt{2\gamma_2} \exp(i\theta_2), \quad (\text{D.1.1})$$

$$C \begin{pmatrix} d_1 \\ d_2 \end{pmatrix}^* = -C \begin{pmatrix} d_1 \\ d_2 \end{pmatrix}, \quad C = \begin{pmatrix} r_B & -it_B \\ -it_B & r_B \end{pmatrix}. \quad (\text{D.1.2})$$

Combining these equations leads to two equations:

$$r_B \sqrt{2\gamma_1} \exp(-i\theta_1) - it_B \sqrt{2\gamma_2} \exp(-i\theta_2) = -\sqrt{2\gamma_1} \exp(i\theta_1), \quad (\text{D.1.3})$$

$$-it_B \sqrt{2\gamma_1} \exp(-i\theta_1) + ir_B \sqrt{2\gamma_2} \exp(-i\theta_2) = -\sqrt{2\gamma_2} \exp(i\theta_2). \quad (\text{D.1.4})$$

Multiplying through with  $\exp(i\theta_2)$  in the top equation and with  $\exp(i\theta_1)$  in the bottom gives:

$$r_B \sqrt{\gamma_1} \exp(i(\theta_2 - \theta_1)) - it_B \sqrt{\gamma_2} = -\sqrt{\gamma_1} \exp(i(\theta_2 + \theta_1)), \quad (\text{D.1.5})$$

$$-it_B \sqrt{\gamma_1} + ir_B \sqrt{\gamma_2} \exp(-i(\theta_2 - \theta_1)) = -\sqrt{\gamma_2} \exp(i(\theta_2 + \theta_1)). \quad (\text{D.1.6})$$

Isolating  $\exp(i(\theta_2 + \theta_1))$  in one of these equations and inserting it into the other will yield a quadratic equation for  $\exp(i(\theta_2 - \theta_1))$ :

$$r_B \sqrt{\gamma_1 \gamma_2} x^2 + it_B (\gamma_1 - \gamma_2) x - r_B \sqrt{\gamma_1 \gamma_2} = 0, \quad (\text{D.1.7})$$

where  $x = \exp(i(\theta_2 - \theta_1))$ . Solving this equation gives the following expression for the phase difference:

$$\exp(i(\theta_2 - \theta_1)) = \frac{it_B (\gamma_2 - \gamma_1) \pm \sqrt{4\gamma_1 \gamma_2 - t_B^2 (\gamma_1 + \gamma_2)^2}}{2\sqrt{(1 - t_B^2) \gamma_1 \gamma_2}}, \quad (\text{D.1.8})$$

where the relation  $r_B^2 + t_B^2 = 1$  have been used.

---

## Miscellaneous plots

This appendix contains plots supporting the results presented in Chapter 4.

### E.1 Full field distributions

In Figure E.1 the real part of the magnetic field plotted in Figure 4.10 is seen.

Full field distributions are presented in this appendix supporting the choice of only looking at the field distribution in the mid of the waveguide region as done in section 4.3. All the structures in Figures E.2-E.7 are illuminated at the bottom with their respective resonance frequency found from fitting their transmission spectra to coupled-mode theory and the resulting field distribution of  $E_x$  is plotted. There are small differences between the fields, but it is difficult to see a pattern in these plots between parity and field distribution.

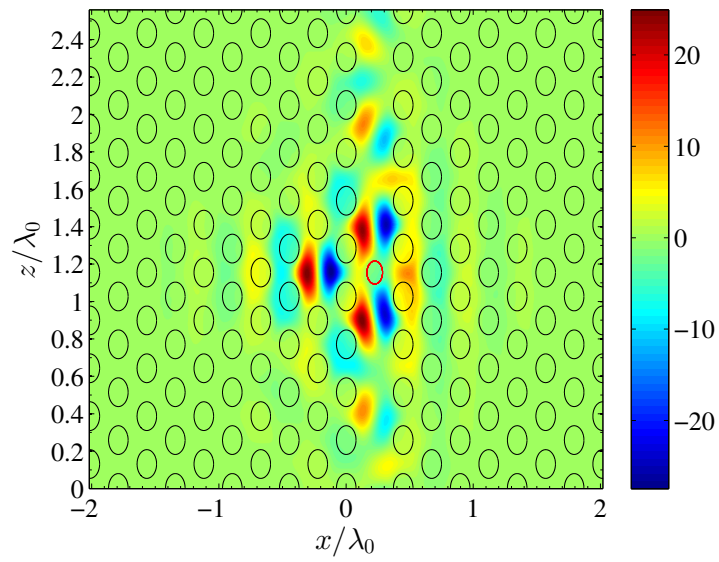


**Figure E.1:** The real part of the magnetic field plotted in Figure 4.10.

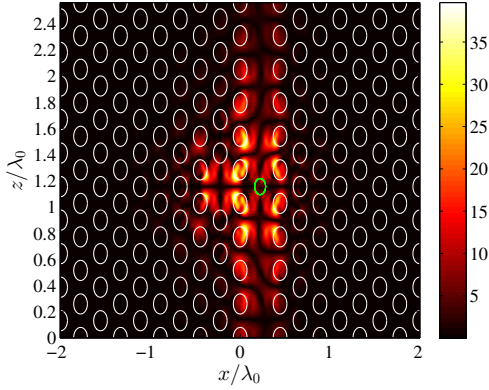


**Figure E.2:** Full field distribution of  $E_x$ . The distance between blocking element is  $d_{block,cav} = 0.0a$  and the radius of the blocking element is  $r_{block} = 0.8r/a$ . This structure has red parity.

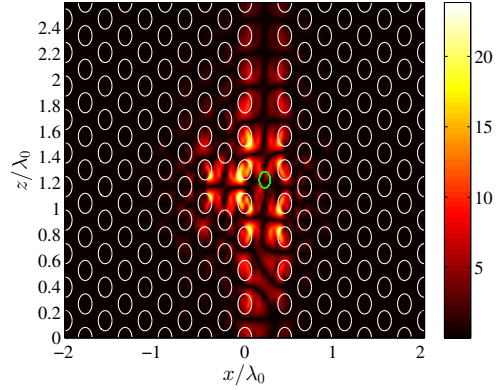


**Figure E.5:** Full field distribution of  $E_x$ . The distance between blocking element is  $d_{block,cav} = 0.20a$  and the radius of the blocking element is  $r_{block} = 0.8r/a$ . This structure has blue parity.

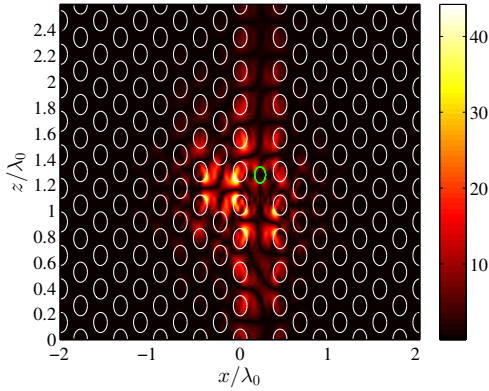


**Figure E.3:** Full field distribution of  $E_x$ . The distance between blocking element is  $d_{block,cav} = 0.40a$  and the radius of the blocking element is  $r_{block} = 0.8r/a$ . This structure has blue parity.

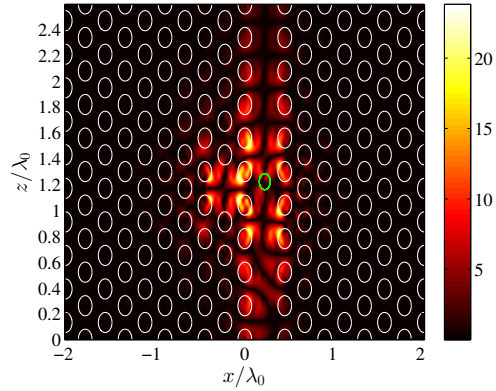


**Figure E.6:** Full field distribution of  $E_x$ . The distance between blocking element is  $d_{block,cav} = 0.60a$  and the radius of the blocking element is  $r_{block} = 0.8r/a$ . This structure has red parity.

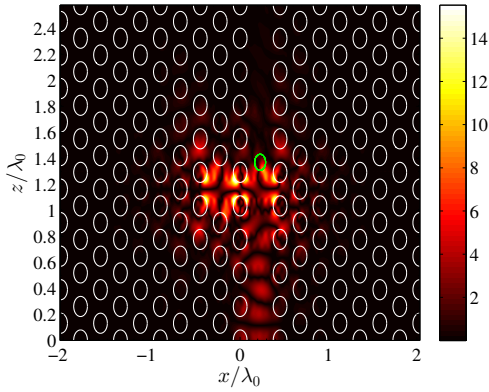


**Figure E.4:** Full field distribution of  $E_x$ . The distance between blocking element is  $d_{block,cav} = 0.80a$  and the radius of the blocking element is  $r_{block} = 0.8r/a$ . This structure has blue parity.

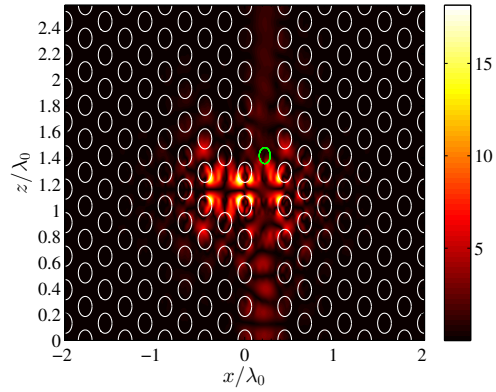


**Figure E.7:** Full field distribution of  $E_x$ . The distance between blocking element is  $d_{block,cav} = 1.00a$  and the radius of the blocking element is  $r_{block} = 0.8r/a$ . This structure has blue parity.

## E.2 Transmission spectra, $r_{block} = 0.80r/a$

Transmission spectra for PhC fano structures with  $r_{block} = 0.80r/a$  are shown in Figures E.8-E.15.

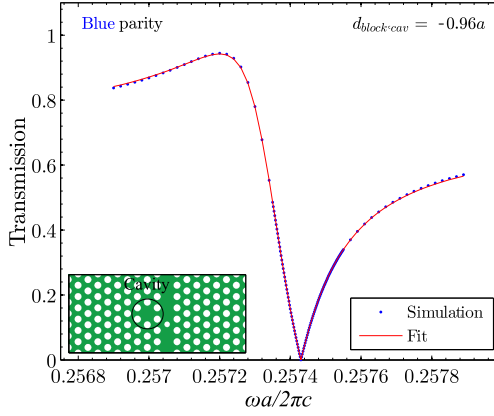


**Figure E.8:** Transmission spectrum fitted to coupled-mode theory for a PhC Fano structure with  $r_{block} = 0.80r/a$  and  $d_{block,cav} = -0.96a$ .

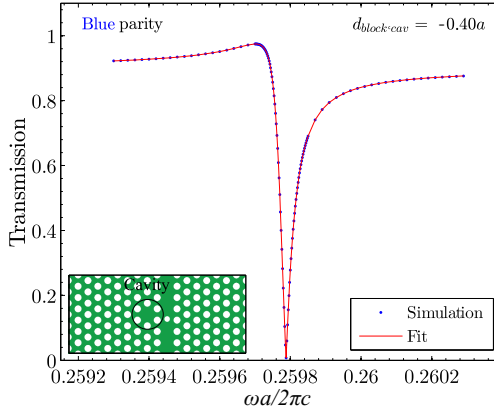


**Figure E.9:** Transmission spectrum fitted to coupled-mode theory for a PhC Fano structure with  $r_{block} = 0.80r/a$  and  $d_{block,cav} = -0.40a$ .

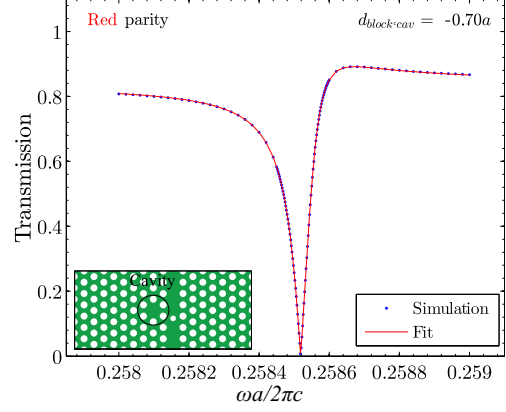


**Figure E.10:** Transmission spectrum fitted to coupled-mode theory for a PhC Fano structure with  $r_{block} = 0.80r/a$  and  $d_{block,cav} = -0.70a$ .

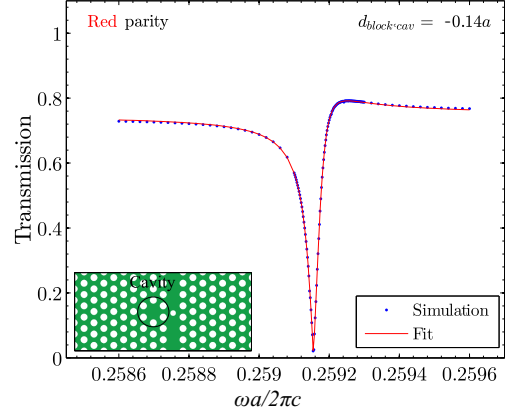


**Figure E.11:** Transmission spectrum fitted to coupled-mode theory for a PhC Fano structure with  $r_{block} = 0.80r/a$  and  $d_{block,cav} = -0.14a$ .

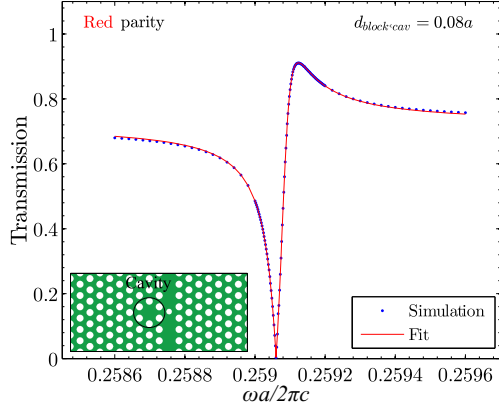


**Figure E.12:** Transmission spectrum fitted to coupled-mode theory for a PhC Fano structure with  $r_{block} = 0.80r/a$  and  $d_{block,cav} = 0.08a$ .

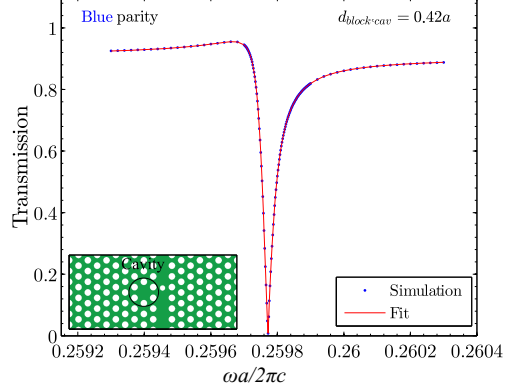


**Figure E.14:** Transmission spectrum fitted to coupled-mode theory for a PhC Fano structure with  $r_{block} = 0.80r/a$  and  $d_{block,cav} = 0.42a$ .

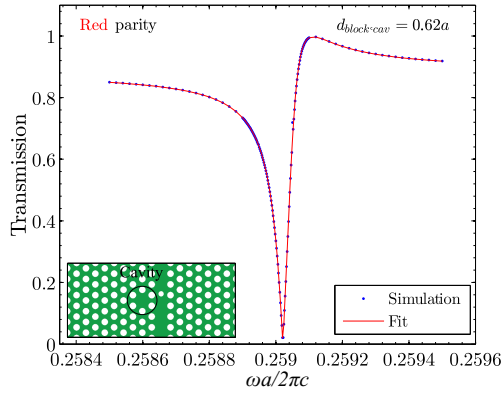


**Figure E.13:** Transmission spectrum fitted to coupled-mode theory for a PhC Fano structure with  $r_{block} = 0.80r/a$  and  $d_{block,cav} = 0.62a$ .

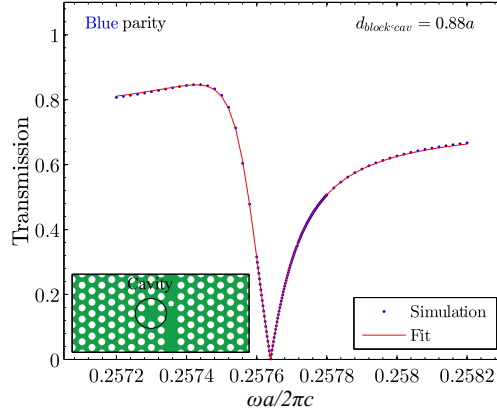


**Figure E.15:** Transmission spectrum fitted to coupled-mode theory for a PhC Fano structure with  $r_{block} = 0.80r/a$  and  $d_{block,cav} = 0.88a$ .

### E.3 Transmission spectra $r_{block} = 0.30 r/a$

Transmission spectra for the Fano structures are found in this appendix. In Figures E.16 - E.19 the transmission spectra are seen for the Fano structure with the slightly changed cavity illustrated in Figure 4.22. In Figure E.16 a single point deviates from the Fano line function and this is due to a numerical error as discussed in section 3.5.

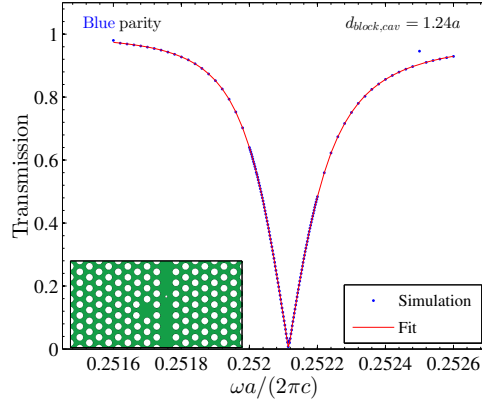


**Figure E.16:** Transmission spectrum fitted to coupled-mode theory for a PhC Fano structure with  $r_{block} = 0.30r/a$  and  $d_{block,cav} = 1.24a$ . This spectrum has blue parity and as seen a single point deviates from the fitted Fano line function.

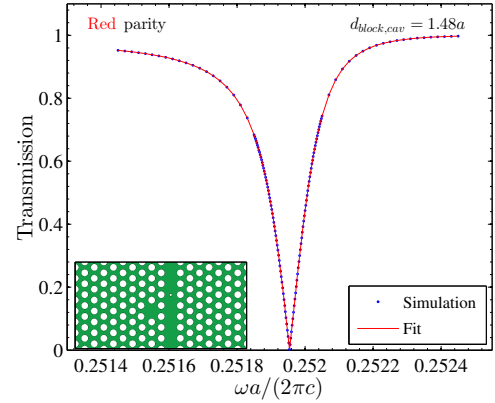


**Figure E.18:** Transmission spectrum fitted to coupled-mode theory for a PhC Fano structure with  $r_{block} = 0.30r/a$  and  $d_{block,cav} = 1.48a$ . This spectrum has red parity.

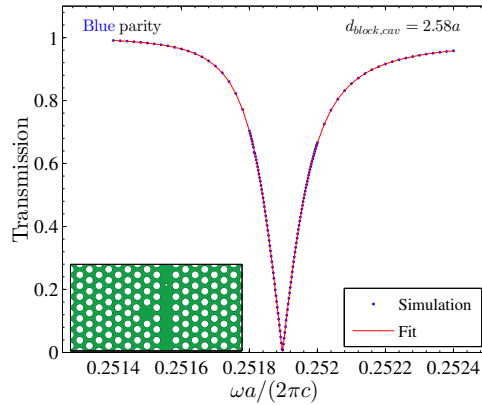


**Figure E.17:** Transmission spectrum fitted to coupled-mode theory for a PhC Fano structure with  $r_{block} = 0.30r/a$  and  $d_{block,cav} = 2.58a$ . This spectrum has blue parity.

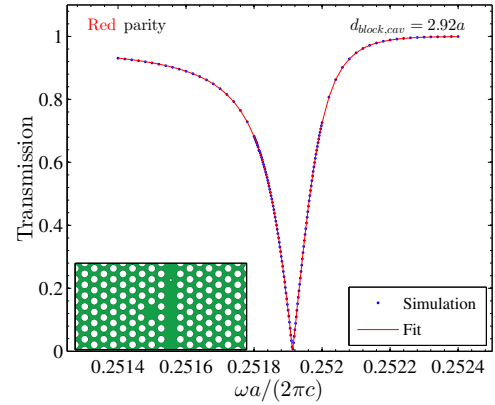


**Figure E.19:** Transmission spectrum fitted to coupled-mode theory for a PhC Fano structure with  $r_{block} = 0.30r/a$  and  $d_{block,cav} = 2.92a$ . This spectrum has red parity.

## E.4 Resonance frequency and direct transmission coefficient

In Figure E.20 the direct transmission coefficient and the resonance frequency plotted as function of the distance between blocking element and cavity for  $r_{block} = 0.30r/a$ . As seen the points do not lie on a smooth line as in Figure 4.15 and this is probably due to the stair case approximation of the small blocking element not having enough steps - thereby making the blocking element not as circular as it should be. This is further discussed in the end of section 4.2.

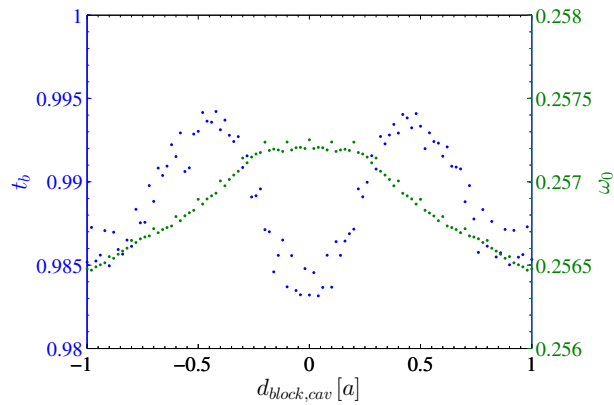


**Figure E.20:** The direct transmission coefficient and the resonance frequency as function of distance between blocking element and cavity. The size of the blocking element is  $r_{block} = 0.30r/a$ .

## **E.5 Field distribution in mid of waveguide**

In Figures E.21-E.24 the field distribution in the mid of the waveguide for different Fano and blocked waveguide structures are plotted. The vertical black lines indicate the position of the blocking element and the vertical dashed line indicate the start of the final periodic section. All of the structures are illuminated with the resonance frequency of the corresponding Fano structure. Similar plots are seen in Figures E.25 - E.28, where the size of the blocking element has been reduced to  $r_{block} = 0.30r/a$ .

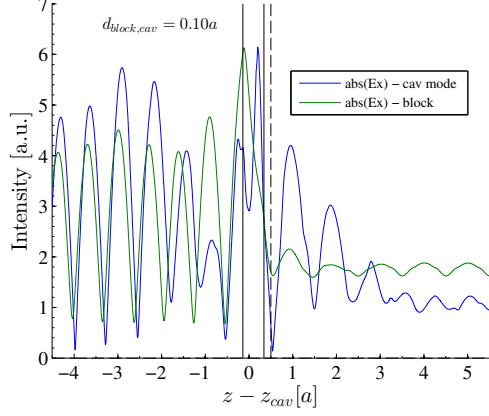


**Figure E.21:** Field distribution of  $E_x$  in the mid of the waveguide region for the Fano structure (cav mode) and the blocked waveguide structure (block). The distance between blocking element and cavity is  $d_{block,cav} = 0.10a$  and the radius of the blocking element is  $r_{block} = 0.80r/a$ . The Fano structure has red parity.

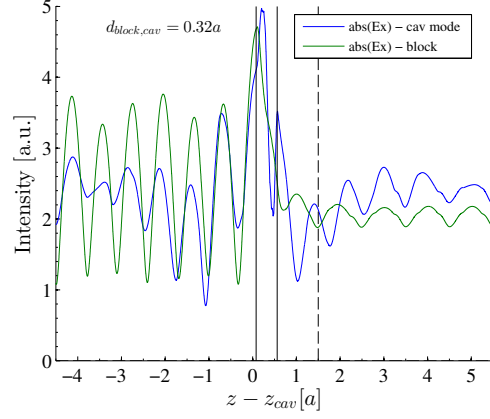


**Figure E.23:** Field distribution of  $E_x$  in the mid of the waveguide region for the Fano structure (cav mode) and the blocked waveguide structure (block). The distance between blocking element and cavity is  $d_{block,cav} = 0.32a$  and the radius of the blocking element is  $r_{block} = 0.80r/a$ . The Fano structure has blue parity.

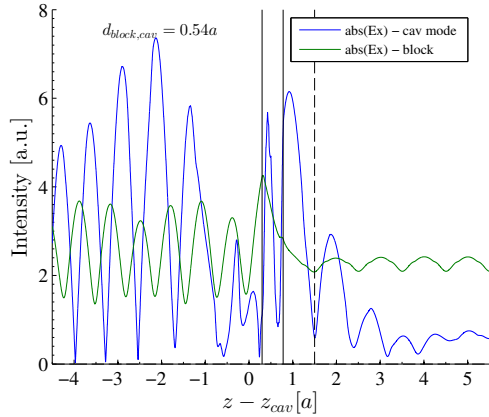


**Figure E.22:** Field distribution of  $E_x$  in the mid of the waveguide region for the Fano structure (cav mode) and the blocked waveguide structure (block). The distance between blocking element and cavity is  $d_{block,cav} = 0.54a$  and the radius of the blocking element is  $r_{block} = 0.80r/a$ . The Fano structure has red parity.

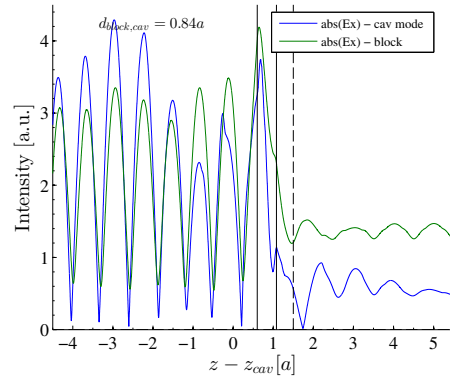


**Figure E.24:** Field distribution of  $E_x$  in the mid of the waveguide region for the Fano structure (cav mode) and the blocked waveguide structure (block). The distance between blocking element and cavity is  $d_{block,cav} = 0.84a$  and the radius of the blocking element is  $r_{block} = 0.80r/a$ . The Fano structure has blue parity.

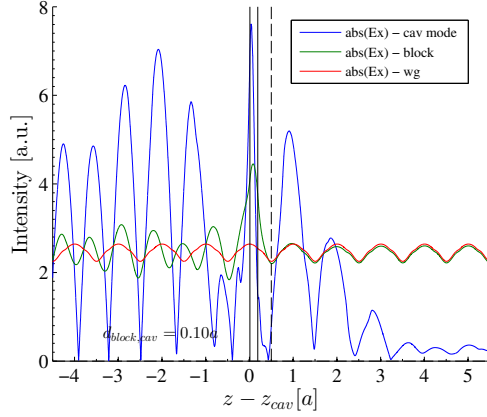


**Figure E.25:** Field distribution of  $E_x$  in the mid of the waveguide region for the Fano structure (cav mode), the blocked waveguide structure (block) and the pure waveguide (wg). The distance between blocking element and cavity is  $d_{block,cav} = 0.10a$  and the radius of the blocking element is  $r_{block} = 0.30r/a$ . The Fano structure has red parity.

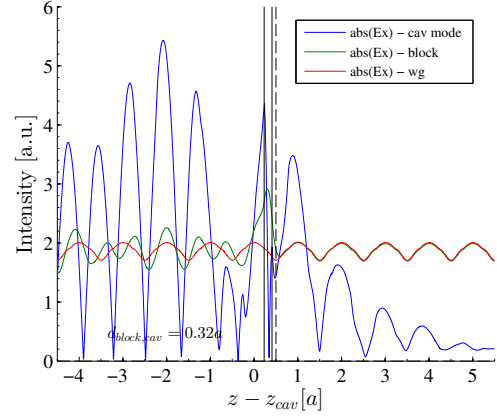


**Figure E.27:** Field distribution of  $E_x$  in the mid of the waveguide region for the Fano structure (cav mode), the blocked waveguide structure (block) and the pure waveguide (wg). The distance between blocking element and cavity is  $d_{block,cav} = 0.32a$  and the radius of the blocking element is  $r_{block} = 0.30r/a$ . The Fano structure has blue parity.

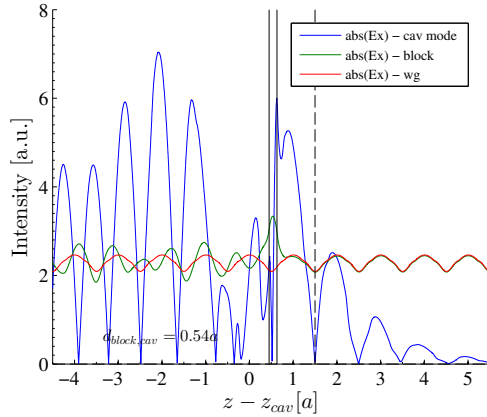


**Figure E.26:** Field distribution of  $E_x$  in the mid of the waveguide region for the Fano structure (cav mode), the blocked waveguide structure (block) and the pure waveguide (wg). The distance between blocking element and cavity is  $d_{block,cav} = 0.54a$  and the radius of the blocking element is  $r_{block} = 0.30r/a$ . The Fano structure has red parity.

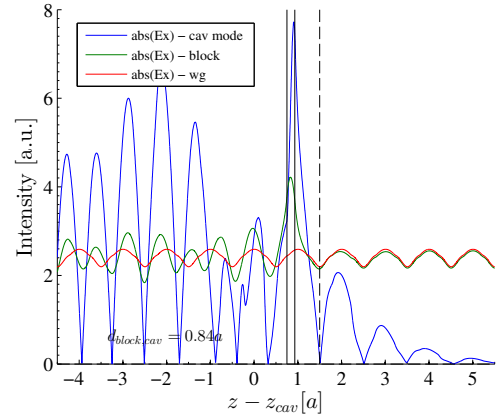


**Figure E.28:** Field distribution of  $E_x$  in the mid of the waveguide region for the Fano structure (cav mode), the blocked waveguide structure (block) and the pure waveguide (wg). The distance between blocking element and cavity is  $d_{block,cav} = 0.84a$  and the radius of the blocking element is  $r_{block} = 0.30r/a$ . The Fano structure has blue parity.

## **CLEO-Europe 2015 submission**

In this appendix our submission abstract for CLEO-Europe 2015 is found. The submission deadline was 19th January 2015 and the abstract was written with the at that time obtained results.

# Determining the Parity of Fano Resonance from Field Distribution in a Photonic Crystal Waveguide-Cavity Structure

Andreas D. Østerkryger\*, Jakob R. de Lasson, Yi Yu, Jesper Mørk and Niels Gregersen

DTU Fotonik, Department of Photonics Engineering, Technical University of Denmark, Ørsted's Plads, Building 343, DK-2800 Kongens Lyngby

\*corresponding author, E-mail: adyhlosterkryger@gmail.com

Fano resonances, as a universal phenomenon, may in photonic structures result from the interference between a discrete resonance and a continuum of modes. They can be realized by placing a partially transmitting element (PTE) in a waveguide that is positioned next to a cavity as in [1] where a Fano structure has been realized in a photonic crystal. The appearance of Fano resonances is well predicted by coupled-mode theory [2]. It has been shown experimentally that the parity of the transmission spectrum changes when the PTE is moved along the waveguide and that Fano structures are suitable for photonic switching due to its unique nonlinear transfer function [1]. In Figure 1a, computed transmission spectra of two PhC Fano structures (see the inset) are plotted with the only difference being the position of the PTE relative to the cavity.

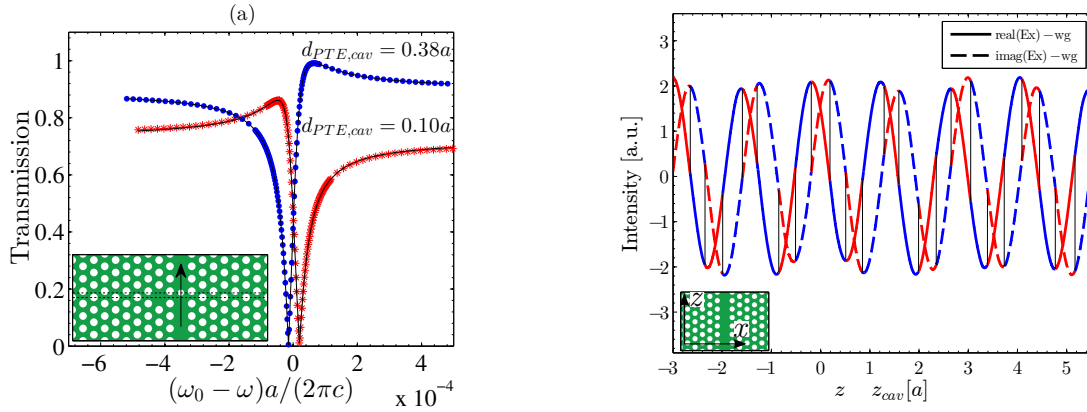


**Figure 1:** (a) A PhC Fano structure is seen in the inset, where the arrow indicates the direction of transmission and the two dotted lines indicate the positions of the cavity and the PTE.  $d_{PTE,cav}$  is equal to the distance between these two lines. Two different simulations with different PTE-cavity distances are shown - one with red parity (asterisk symbol) and one with blue (dot symbol). Red (blue) parity means that the minimum is red (blue) shifted relative to the maximum. (b) The real and imaginary part of the  $E_x$ -field in the middle of the waveguide plotted for a bare waveguide PhC structure. The parity is found from simulations of PhC Fano structures. As seen the parity changes when the PTE is moved across an extremum of either the real or imaginary part of  $E_x$  illustrated by the vertical dashed lines.

Coupled-mode theory predicts that the phase difference between a field taking the direct path in the waveguide through the PTE and a field taking a longer way through the cavity directly determines the parity of the Fano resonance. The phase difference can be determined by fitting the full transmission spectrum to coupled-mode theory, but we propose here a simpler and faster method for determining the parity of a Fano resonance.

In Figure 1b, the  $E_x$  field distribution of the Bloch mode of a bare PhC waveguide is plotted. The colors indicate the Fano parity, and it is observed that the parity changes whenever the PTE is moved across an extremum of either the real or imaginary part of the field. The waveguide is illuminated with the fundamental mode at the resonance frequency of the mirror symmetric PhC Fano structure, i.e. the structure where  $d_{PTE,cav} = 0$ . The resonance frequency depends slightly on the position of the PTE relative to the cavity and therefore there is a small deviation between the extrema of  $E_x$  and where the parity changes. Understanding how to control the Fano parity allows the realization of various switching configurations, as will be discussed at the conference.

## References

- [1] Y. Yu and M. Heuck and H. Hu and W. Xue and C. Peucheret and Y. Chen and L. K. Oxenløwe and K. Y. and J. Mørk, "Fano resonance control in a photonic crystal structure and its application to ultrafast switching," *App. Phys. Lett.* **105**, 061117 (2014).
- [2] W. Suh and Z. Wang and S. Fan, "Temporal Coupled-Mode Theory and the Presence of Non-Orthogonal Modes in Lossless Multimode Cavities," *IEEE J. Quant. Electron.* **40**, 1511-1518 (2004).

## Bibliography

- [1] J. Mørk, Y. Chen, and M. Heuck, “Photonic crystal fano laser: Terahertz modulation and ultrashort pulse generation,” *Phys. Rev. Lett.* **113** (2014).
- [2] T. F. Krauss, “Photonic crystals for integrated optics,” <http://www.st-andrews.ac.uk/photocryst/Assets/Publications/erice.pdf> (2015).
- [3] M. Heuck, P. T. Kristensen, Y. Elesin, and J. Mørk, “Improved switching using fano resonances in photonic crystal structures,” *Opt. Lett.* **38** (2013).
- [4] Y. Yu, M. Heuck, H. Hu, W. Xue, C. Peucheret, Y. Chen, L. K. Oxenløwe, K. Yvind, and J. Mørk, “Fano resonance control in a photonic crystal structure and its application to ultrafast switching,” *Appl. Phys. Lett.* **105** (2014).
- [5] D. A. B. Miller, “Device requirements for optical interconnects to silicon chips,” *Proc. IEEE* **97** (2009).
- [6] Y. Yu, M. Heuck, W. Xue, C. Peucheret, Y. Chen, K. Yvind, and J. Mørk, “Fano resonance control in a photonic crystal structure and its application to ultrafast switching,” (2014).
- [7] K. Takeda, T. Sato, A. Shinya, K. Nozaki, W. Kobayashi, H. Taniyama, M. Notomi, K. Hasebe, T. Kakitsuka, and S. Matsuo, “Few-fj/bit data transmissions using directly modulated lambda-scale embedded active region photonic-crystal lasers.” *Nature Photonics* **7** (2013).
- [8] H. C. Nguyen, Y. Sakai, M. Shinkawa, N. Ishikura, and T. Baba, “10 gb/s operation of photonic crystal silicon optical modulators,” *Opt. Express* **19** (2011).
- [9] K. Nozaki, T. Tanabe, A. Shinya, S. Matsuo, T. Sato, H. Taniyama, and M. Notomi, “Sub-femtojoule all-optical switching using a photonic-crystal nanocavity,” *Nature Photonics* **4** (2010).
- [10] T. Tanabe, H. Sumikura, H. Taniyama, A. Shinya, and M. Notomi, “All-silicon sub-gb/s telecom detector with low dark current and high quantum efficiency on chip,” *Appl. Phys. Lett.* **96** (2010).
- [11] S. Fan, W. Suh, and J. D. Joannopoulos, “Temporal coupled-mode theory for the fano resonance in optical resonators,” *J. Opt. Soc. Am. A* **20** (2003).
- [12] W. Suh, Z. Wang, and S. Fan, “Temporal coupled-mode theory and the presence of non-orthogonal modes in lossless multimode cavities,” *IEEE J. Quant. Electron.* **40** (2004).

- [13] K. X. Wang, Z. Yu, S. Sandhu, and S. Fan, “Fundamental bounds on decay rates in asymmetric single-mode optical resonators,” *Opt. Lett.* **38** (2013).
- [14] D. Pisssoort, B. Denecker, P. Bienstman, F. Olyslager, and D. D. Zutter, “Comparative study of three methods for the simulation of two-dimensional photonic crystals,” *J. Opt. Soc. Am. A* **21** (2004).
- [15] D. J. Griffiths, *Introduction to electrodynamics*, 3rd ed. (Pearson, 2008).
- [16] A. V. Lavrinenko, J. Lægsgaard, N. Gregersen, F. Schmidt, and T. Søndergaard, *Numerical methods in photonics* (CRC Press, 2014).
- [17] J. D. Joannopolous, S. G. Johnson, J. N. Winn, and R. D. Meade, *Photonic Crystals - Molding the flow of light*, 2nd ed. (Princeton University Press, 2008).
- [18] M. Fox, *Optical properties of solids*, 2nd ed. (Oxford, 2010).
- [19] P. Bienstman and R. Baets, “Optical modelling of photonic crystals and vcsels using eigenmode expansion and perfectly matched layers,” *Opt. Quantum. Electron.* (2001).
- [20] L. Novotny and B. Hecht, *Principles of Nano-Optics*, 2nd ed. (Cambridge University Press, 2012).
- [21] J. R. de Lasson, P. T. Kristensen, J. Mørk, and N. Gregersen, “Roundtrip matrix method for calculating the leaky resonant modes of open nanophotonic structures,” *J. Opt. Soc. Am. A* **31** (2014).
- [22] P. T. Kristensen and S. Hughes, “Modes and mode volumes of leaky optical cavities and plasmonic nanoresonators,” *ACS Photonics* **1** (2014).
- [23] J. R. de Lasson, P. T. Kristensen, J. Mørk, and N. Gregersen, “A bloch modal approach for engineering waveguide and cavity modes in two-dimensional photonic crystals,” *SPIE Journal of Nanophotonics* (2014).
- [24] [http://en.wikipedia.org/wiki/Moore%E2%80%93Penrose\\_pseudoinverse](http://en.wikipedia.org/wiki/Moore%E2%80%93Penrose_pseudoinverse), (23.01.2015).